POLITECNICO
MILANO 1863

Ultrafast UV spectroscopy of primary photoinduced processes in biomolecules

PhD thesis in Physics

Piotr Kabaciński

Advisor: Prof. Giulio Cerullo
Tutor: Prof. Sandro de Silvestri

Academic Year 2021/2022 - Cycle XXXIV

Acknowledgements

I would like to first of all thank my PhD thesis supervisor prof. Giulio Cerullo for guiding me these three years when building the UV transient absorption setup and with various spectroscopy projects we worked on.

I would also like to thank Cristian Manzoni for the help with building the setup and many interesting and deep discussions about optics, Lucia Ganzer and Rocio Borrego-Varillas for introducing me to the lab and the UV spectroscopy, and the whole group of prof. Cerullo for the time spent together.

As the PhD program has been conducted within the LightDyNAmics consortium, I would like to thank everyone involved, but specifically Vishal Jaiswal, his supervisor prof. Marco Garavelli, and the whole group for fruitful collaboration.

Finally, I thank my dear friend Vasilis Petropoulos for support and many discussions about science and life.

Abstract

Since the discovery of double helix DNA structure in 1953, the understanding of the inner workings of the cell has seen tremendous growth. With various tools we gained insight into the molecular structures of DNA, amino acids and proteins. In parallel, the advancements in laser technology kept opening new ways of studying all kinds of matter, with both steady state and time-resolved techniques. Recently, developments in ultrafast optics opened a path towards sub-picosecond temporal resolution measurements across the spectrum.

In this work, we have built a UV transient absorption spectroscopy setup for investigation of ultrafast photoinduced dynamics in biomolecules at the fastest timescales. The setup features a tunable sub-20-fs UV pump pulse and a broadband probe pulse, for high temporal resolution probing in a wide range of energies. The obtained experimental results were compared each time with advanced computations done by our collaborators. We have applied this methodology in three main studies.

First, we compare the photophysics of uridine and 5-methyluridine, two nucleosides differing only by the presence of methyl group. After years of scientific debate, our results solve the remaining questions and correctly assign the observed time constants to the corresponding phenomena, explaining how 5-methyluridine decays an order of magnitude longer than uridine. In the second study, we turn our interest towards a group of epigenetic derivatives of deoxycytidine, which are responsible for regulating gene expression. We systematically map out the excited state decay pathways and asses how different substitutions modify the response. Finally, we look at the earliest photoinduced events in tryptophan, the brightest chromophore among the aromatic amino acids. We find that the high sensitivity to solvent environment governs the relaxation dynamics, which extends its possible applications as a local probe of protein behavior to the ultrafast timescales.

Our findings prove that the technology of ultrafast UV spectroscopy is now mature enough to study more and more complex systems, which with theoretical support can be disentangled and shed light on plethora of fascinating processes in biomolecules.

Keywords: transient absorption, UV, biomolecules, DNA, tryptophan

Contents

1 | Introduction

Every living cell functions thanks to the complex machinery of proteins assembling other proteins from amino acids, based on the genetic code written in the deoxyribonucleic acid (DNA) double helices. All of the macroscopic properties of the cell, and the whole organism, depend on the stability of DNA and the correct performance of the proteins. A common theme between all of these molecules is that their ultraviolet (UV) absorption makes them potentially vulnerable to the interaction with those highly energetic photons, but on the other hand, it lets us study their properties using various methods of UV spectroscopy. This work explores the application of ultrafast UV spectroscopy, specifically transient absorption (TA), for the investigation of the primary photoinduced processes in several chosen biomolecules.

1.1. DNA

The basic structure and processes relating to the studied molecules are shown in Figure 1.1. The genetic information is stored in the double strands of DNA as a sequence of nucleotides, where it also goes through a replication process. This process produces two identical replicas of DNA and is essential for cell division during the growth of the organism and repair of damaged tissue. A nucleotide consists of a nucleobase, and deoxyribose sugar with a phosphate group, binding the neighboring nucleotides into a strand, through the sugar-phosphate backbone. Adenine, cytosine, guanine, and thymine, are the canonical bases of DNA that match in pairs from the opposing strands and their sequence encodes the information used for building the whole organism. DNA cannot leave the nucleus of the cell, instead, it undergoes a process of transcription, forming a ribonucleic acid (RNA) molecule which is smaller and can leave the nucleus into the cytoplasm for the readout of the genetic information. RNA is made of only a single strand of nucleobases and contains uracil instead of thymine in its set of canonical bases. Outside of the nucleus, the ribosomes, macromolecular machines composed of protein and RNA, translate the code of messenger RNA strands into a polypeptide chain of amino acids, the main structural building blocks of proteins. The polypeptide then folds onto itself forming a biologically

active protein in its native three-dimensional structure and begins serving its function for the organism.

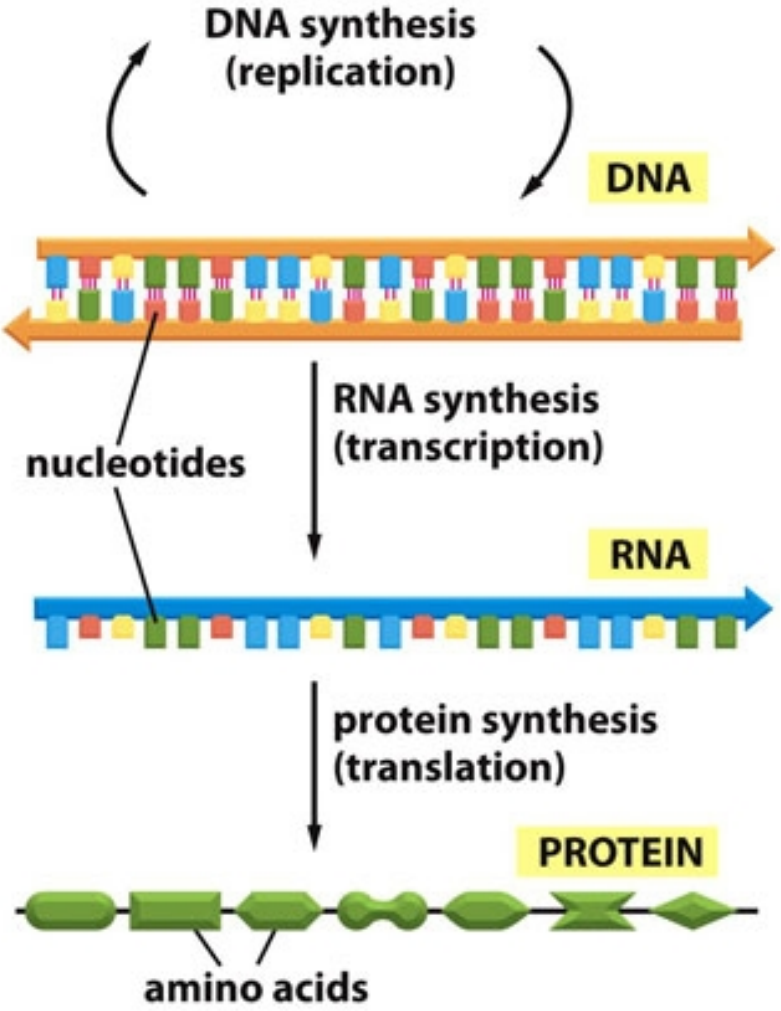

Figure 1.1: Processes of DNA replication, transcription into RNA, and translation into chain of amino acids forming a protein[1].

Looking into the DNA in more detail in Figure 1.2a, we can recognize the molecular structure of individual nitrogen-rich nucleobases and the hydrogen bonds formed between them. Adenine and guanine have a fused-ring structure derived from purine, thus they are called purine nucleobases, while the simple ring structures of cytosine and thymine are derived from pyrimidine, and called pyrimidine nucleobases. The respective absorption spectra for the DNA nucleosides (bases together with deoxyribose sugar) are shown in Figure 1.2b. We can see how the absorption bands of their lowest excited states all appear below 300 nm and extend deeper into the short wavelengths of the UV region, allowing their study with UV light, and on the other hand, making them prone to unwanted interactions caused by the high energy deposited by the UV photons.

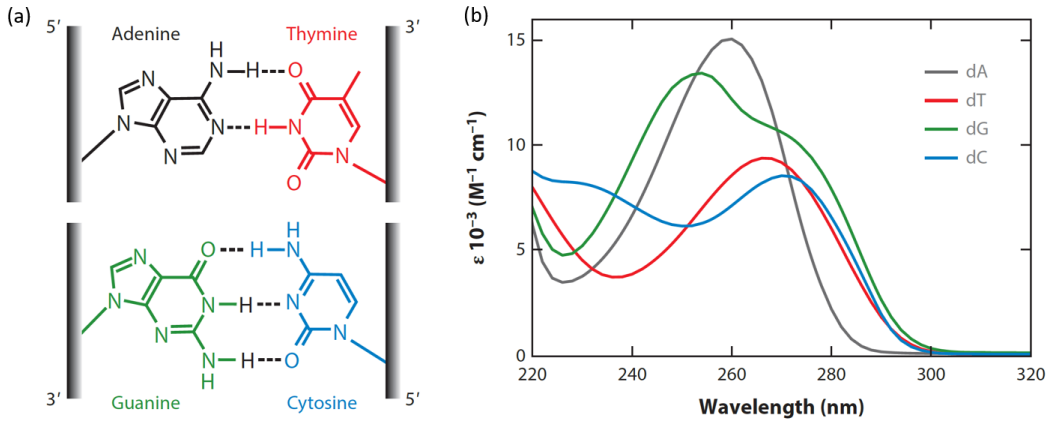

Figure 1.2: (a) Molecular structures of pairs of canonical DNA nucleosides: Adenine (dA), Thymine (dT), and Guanine (G), Cytosine (C), within a double strand and (b) their UV absorption spectra[2].

1.2. Damage and photoprotection mechanisms

The UV photons, such as those coming in the form of solar radiation, may cause several types of damage in the DNA structure, for example, a cyclobutane pyrimidine dimer (CPD), as shown schematically in Figure 1.3, where the two neighboring pyrimidine bases form a photolesion, becoming covalently bound into a stable photoproduct[3]. Such lesions, if not repaired, may lead to incorrect replication or transcription processes, carrying over the damage and producing malfunctioning proteins. In humans, the DNA contained in the skin cells is the most prone to UV damage. Repeating modifications of DNA structure caused by long exposure to the sun are often too difficult to sufficiently quickly repair, and when ignored often lead to skin cancer formation[4].

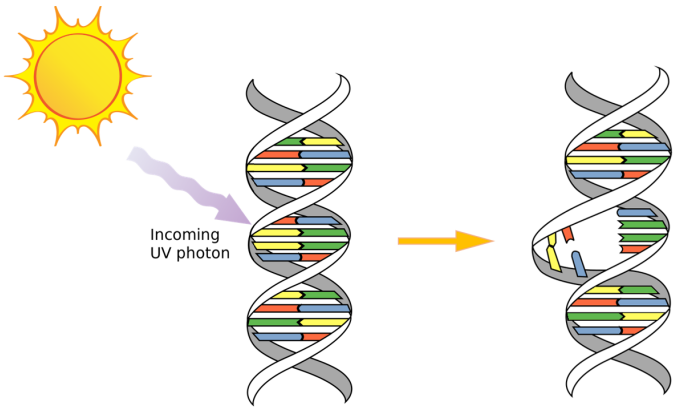

Figure 1.3: Schematic representation of cyclobutane pyridimide dimer formation through solar UV irradiation.

Fortunately, the molecules selected for storing genetic information by evolution, are quite robust against the UV photodamage[2,5]. In single nucleobases, this is done through the existence of efficient non-radiative routes of ultrafast decay to the ground state (GS) and subsequent dissipation of vibrational energy of the hot GS into the surrounding water[6–11]. This ultrafast decay is made possible due to the existence of conical intersection (CI), a degeneracy point between the potential energy surface (PES) of the excited state and the ground state (Figure 1.4) that is usually reached in a few hundred femtoseconds[12]. At a specific nuclear geometry, the energy degeneracy will favor transition between the states, freeing the system from electronic excitation that could lead to a chemical reaction, such as the one forming CPDs[13,14]. Thanks to this mechanism, the vast majority of UV interactions do not result in photodamage, as demonstrated by less than 1% quantum yields of lesion formation[15].

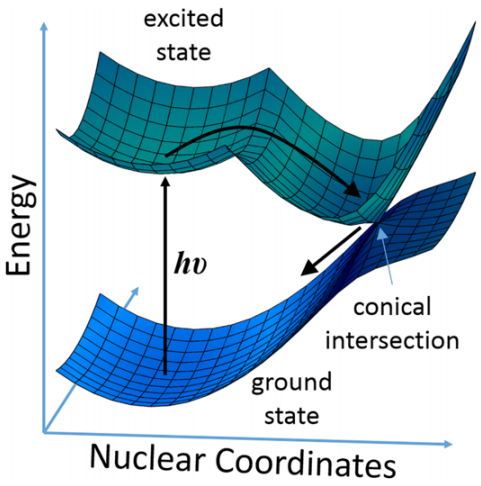

Figure 1.4: Diagram explaining conical intersection, a molecular geometry point where the energies of the two potential energy surfaces become degenerate, allowing a non-adiabatic coupling between the states. Through conical intersections, the wavepacket can non-radiatively decay from the excited to the ground state.[12].

CIs have been located in all of the canonical nucleobases and many derivatives at various levels of theory[16] and later confirmed through fluorescence up-conversion or transient absorption measurements[17]. In nucleobases, CIs are usually accessed via out-of-plane deformations that are initiated by double bond twisting; for pyrimidines, many studies have shown that torsion around the C5-C6 bond is the main deactivation step. While the energy of the excited state is not very sensitive to ring puckering, the ground state on the other hand is strongly destabilized by the loss of π-bond stabilization. This results in a sharp rise of ground state energy along the ring-deformation coordinate, bringing it high enough to cross with the excited state surface which is relatively flat. Lifetimes of excited

states are sensitive to C5 substitutions[18], which can be explained through the restricted ability of torsion around this bond due to the substituent, as found through fluorescence measurements[19,20]. Following the crossing of the CI, high energy is deposited into the vibrational modes of the ground state. This can be observed by a strongly red-shifted ground state absorption spectrum, which returns to equilibrium by transferring the energy to the surrounding solvent in a process known as vibrational cooling on a timescale of a few picoseconds.

In addition to the bright $^1\pi\pi^*$ excited states, also dark $^1n\pi^*$ states as well as triplet states $^3n\pi^*$ and $^3\pi\pi^*$ have been characterized, although it is not straightforward with conventional spectroscopic techniques. Dark states can be also reached by internal conversion (IC), and the triplet states by inter-system crossing (ISC) processes through CIs. It has been observed that the $^1n\pi^*$ lifetimes are significantly longer for pyrimidine nucleosides than for nucleobases[21].

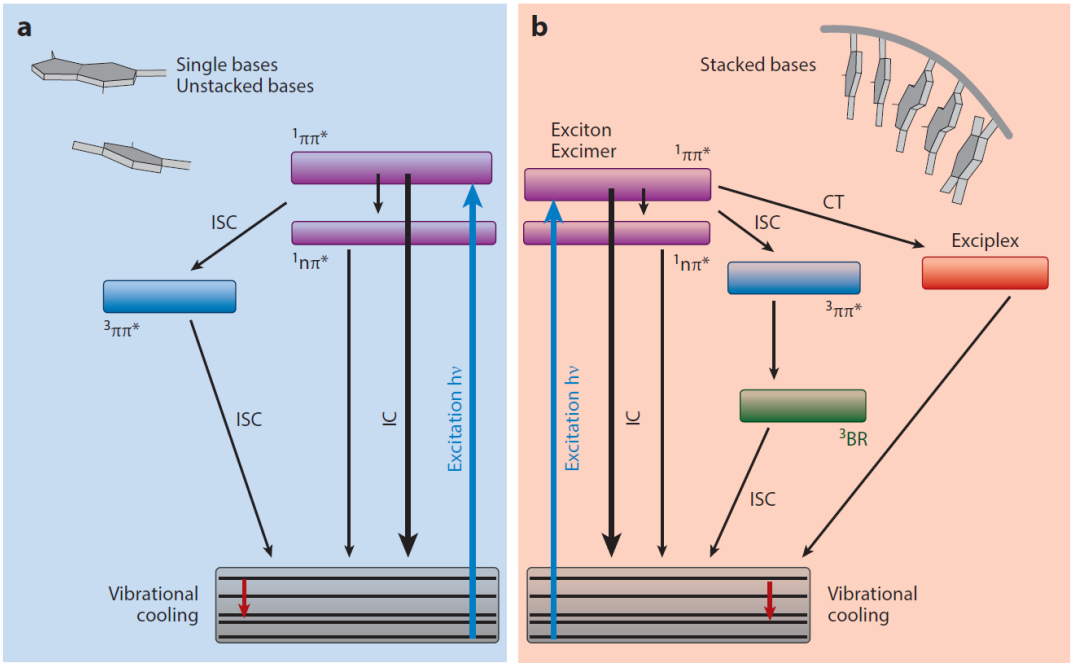

Figure 1.5: Photophysical processes after UV excitation of (a) isolated nucleobases, and (b) single- and double- stranded DNA[2].

The generalized decay paths in both isolated nucleobases, as well as stacked on a strand are presented in Figure 1.5. While in this work we will discuss only measurements done on nucleosides, it is worth noting that the spatial arrangement within DNA strand determines couplings that give rise to new deactivation pathways, not found in the bases. The relatively flat free energy landscape that governs the structure of the double helix is

responsible for the structural disorder, which has to be considered to correctly interpret experimental results. Both base stacking and base pairing have to be taken into account, and they result in the creation of charge-transfer states and proton transfer dynamics respectively[5,22–24].

1.3. Amino acids

As introduced previously, the information contained in the DNA strands is the basis for the synthesis of proteins by chaining together amino acids. Out of the 21 amino acids building eukaryotic proteins, only three contain aromatic rings: phenylalanine, tyrosine, and tryptophan, whose molecular structures are shown in Figure 1.6. Aromatic rings present in these molecules make them absorb UV light in the 250-300 nm region, similarly to the nucleosides, and are known to be fluorescent. Moreover, these amino acids serve as precursors for the synthesis of other biomolecules. Phenylalanine is used for creating neurotransmitter dopamine, and hormones adrenalin and noradrenalin. Tyrosine is a precursor for melanins, a group of polymerized tyrosine pigments, shielding the skin cells from UV radiation. Tryptophan is also used in the production of the neurotransmitter serotonin, the hormone melatonin, and vitamin B3.

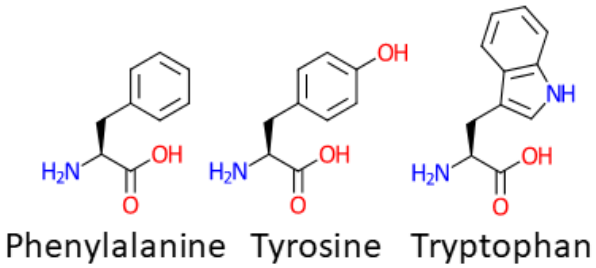

Figure 1.6: Aromatic amino acids: phenylalanine, tyrosine and tryptophan.

Tryptophan has the highest absorbance relative to the other amino acids and the strongest fluorescence signal and this makes it the most appropriate out of the three to be used as a local probe for tracking protein structure and dynamics[25–27]. Computations have shown that the aromatic rings of amino acids in small peptides can be tracked via 2D UV spectroscopy as highly specific markers of structural rearrangements (Figure 1.7)[28]. Similarly, hydrophobic interaction of aromatic side chains with other parts of amino acids in a protein could be tracked dynamically, even on ultrafast timescales[26].

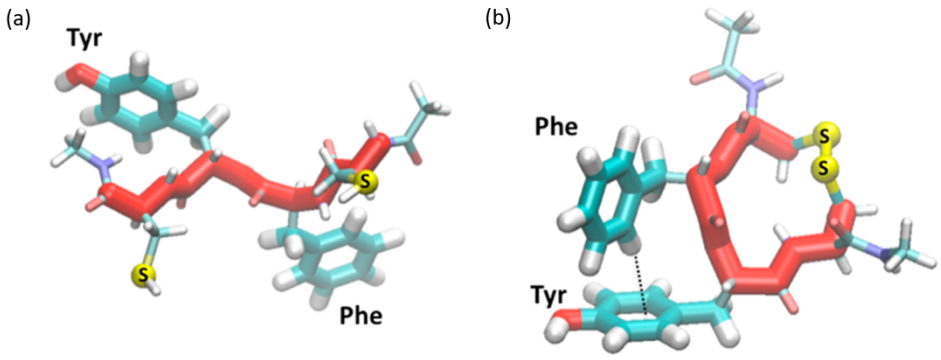

Figure 1.7: Open (a) and closed (b) CFYC peptide configuration with the aromatic rings stacked[28].

In proteins, due to its aromatic structure, tryptophan finds large pockets and can support interactions requiring large surface area. As it is the most bioenergetically expensive amino acid to produce, it only appears in protein sites where it is absolutely needed for its functions, which allows for high selectivity of the application as a local probe. Tryptophan radicals often mediate the biological electron transfer process, as in the case of azurin, the protein that shuttles electrons between enzymes in the cytochrome chain of bacteria, where it has been proposed to play a crucial role as a central redox element promoting a rapid electron transfer to the copper center[29–32].

1.4. Ultrafast spectroscopy techniques

The proper characterization of the excited state deactivation processes in DNA and detailed tracking of protein processes involving aromatic amino acids was elusive due to both theoretical and experimental technical limitations. Experiments suffered from limited temporal resolution and narrow spectral coverage, while issues such as high dispersion in the UV region or the generation of solvated electrons through ionization of the solvent, hindered high resolution and clear readout of the spectroscopic signals. In computations, modelling the nucleoside behavior in the gas phase or using simplified solvent descriptions and not fully considering the electronic correlations, was missing important interactions that influence the dynamics of photoinitiated processes.

With the ongoing improvements in both experimental and theoretical techniques, we are getting closer to the full characterization of the primary photoinduced processes in biomolecules[33,34]. We briefly review here some of the most commonly used ultrafast spectroscopic techniques for the characterization of biomolecules[35,36]. Due to a range of developments of linear and nonlinear optical tools in the visible spectral range, ultrafast spectroscopy became possible. It quickly scaled into the mid- and near- infrared, experiencing a rapid growth. Then, diffraction and scattering methods were implemented using sources of ultrashort X-ray pulses, for studying nuclear structures. However, the UV spectral region has been rather neglected until recently. While it has been straightforward to reach it with a third harmonic of Ti:Sapphire lasers at 266 nm, the tunability of the pump pulses and the broadband probing capabilities close to that region were not achieved for quite a while. The absorption bands of amino acids or nucleotides, other small aromatic molecules or transition metal oxides, all fall in the UV region. As these materials have started attracting much interest in the past 20 years, the progress of tunable deep UV excitation with white light continuum probing became desirable. The last two decades have shown dramatic improvements of ultrafast spectroscopy techniques and brought to life femtosecond time-resolved versions of many of the steady-state techniques, as well as completely new methodologies such as multidimensional photon-echo, coherent anti-Stokes Raman, and others.

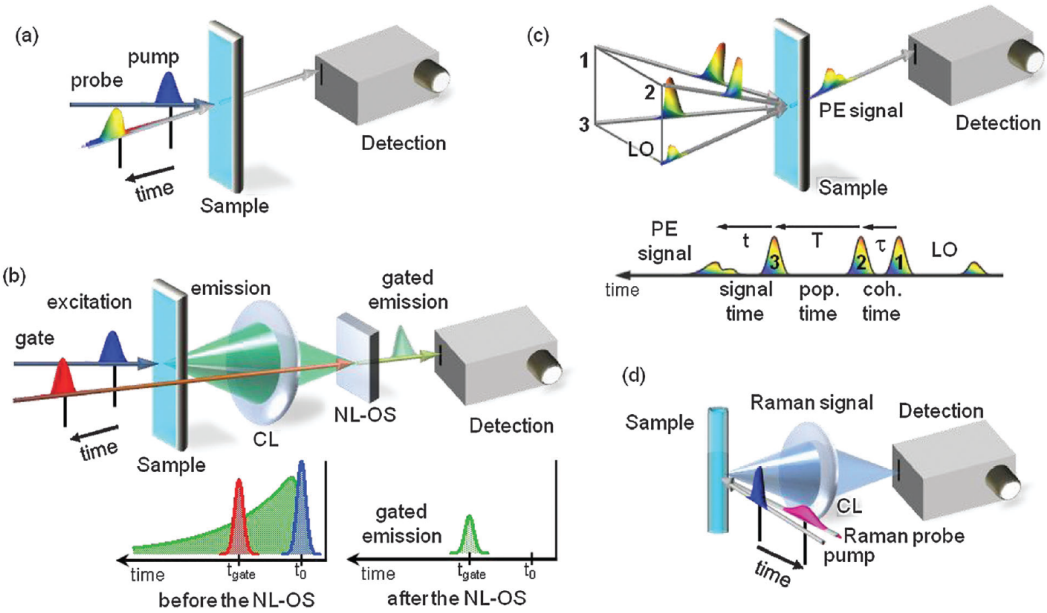

Figure 1.8: Schematic representation of the main ultrafast spectroscopic techniques[35]. (a) Pump-probe transient absorption spectroscopy. (b) Time-resolved fluorescence upconversion spectroscopy. (c) 2D spectroscopy. (d) Time-resolved Raman spectroscopy.

Transient absorption is one of the most widely used ultrafast spectroscopies (Figure 1.8a), and allows measurements of the changes in absorption of the sample while its evolving in its excited state, through pump-modulated transmission of the probe pulse. Its conceptual simplicity and robust geometry allow for stable and high temporal resolution measurements, but overlap several kinds of signals together, which may be difficult to disentangle. The Fourier Transform, heterodyne detected, version of photon echo spectroscopy, called 2D spectroscopy, is a method analogous to multidimensional nuclear magnetic resonance technique, but where electric dipoles instead of magnetic ones are detected. As seen in Figure 1.8c, generally, it uses a more complex sequence of pulses than TA spectroscopy, making it challenging experimentally, but allows for direct study of couplings and long range interactions, as well as differentiating homogenous line shape from the inhomogenous distribution. Time-resolved fluorescence up-conversion, on the other hand, time-gates the signal emitted from the sample after excitation by nonlinear interaction inside an optical shutter, either by sum-frequency or optical Kerr effect (Figure 1.8b). This method gives the dynamics of only the fluorescence emission, but may encounter difficulties with low emission intensities, and needs two interactions of the pulses with the signal, which restricts the lowest attainable temporal resolution. In time-resolved Raman spectroscopy (Figure 1.8d), after excitation the sample is hit with a narrowband Raman probe, that generates signals that are then collected and spectrally resolved. This kind of technique has the advantage that a single narrowband pulse can simultaneously generate signals from many vibrational transitions in a wide frequency range, while avoiding any severe solvent interference.

1.5. Outline

For our investigations of the primary photoinduced processes in biomolecules, we have chosen the method of transient absorption spectroscopy as the most suitable. It simultaneously can be optimized for high temporal resolution and high stability, especially needed during work with fragile samples, nowadays even in the difficult to access UV region, while avoiding the excess complexity and bringing a rich broadband signal to analyze from various angles. After this brief introduction to the field of spectroscopic studies of biological matter, in the rest of this work, we discuss in more detail the optics and parameters of the used TA setup and then proceed with main experimental studies done during the PhD. In Chapter 2, we discuss the necessary basics of ultrashort pulse generation and dispersion management, as well as the nonlinear optical techniques used in transient absorption setups, then discussing the principles of pump-probe technique and finishing the chapter with a discussion of coherent artifacts that plague the TA mea-

surements. Chapter 3 describes the experimental setup constructed for conducting UV TA of biomolecules and specifically the sample delivery method with a wire-guided jet. Chapter 4 compares the behavior of uridine and 5-methyluridine to find how the methyl group elongates the decay to the ground state. Chapter 5 presents the photoprocesses observed in epigenetic deoxycytidine nucleosides, which are DNA base derivatives utilized by the cell for regulating gene expression. Chapter 6 focuses on a detailed description of the earliest behavior of tryptophan, showing how the dynamics are strongly influenced by the solvent and could be used as a sensitive probe of protein behavior. We finish with concluding all the topics discussed here.

2 | Transient absorption spectroscopy

With transient absorption spectroscopy we can characterize materials through the application of laser pulses and extract information about their excited state behavior. Various pulse durations can be used, but in this work, we are focusing on the investigation of the ultrafast timescales, therefore we start with a discussion of the basic description of ultrashort pulses and the nonlinear optics used in the generation of such pulses for experiments. Then, the principles of pump-probe technique and the fundamental signals of transient absorption measurement are discussed. Finally, we note the possibility of observing vibrational fingerprints in the time domain on top of the TA signals, and the commonly observed coherent artifacts, that overlap the measured traces at early times and make the correct interpretation of the signals difficult.

2.1. Ultrashort pulses

As 'ultrashort' we usually consider electromagnetic pulses with time durations on the order of a picosecond (1 picosecond = 10^{-12} seconds) or shorter. The basic way to describe an optical pulse is to use the notion of intensity and phase.

We can describe such a pulse in the time domain as:

$$E(t) \propto \sqrt{I(t)}\exp\{-i\phi(t)\} \tag{2.1}$$

where $I(t)$ is the pulse intensity and $\phi(t)$ is its temporal phase,
or in the frequency domain:

$$\tilde{E}(\omega) \propto \sqrt{S(\omega)}\exp\{-i\varphi(\omega)\} \tag{2.2}$$

where $S(\omega)$ is the spectrum and $\varphi(\omega)$ is the spectral phase.

Both of these quantities can be represented either on a frequency/energy scale with terahertz/electron volts as units or on a wavelength scale with nanometers.

The two descriptions are bound together through a Fourier Transform (FT). When the spectral phase is constant for all frequencies, then the pulse duration is the shortest possible for a given spectrum. Such a pulse is called transform-limited. The broader is the spectrum of the pulse, the shorter duration can be obtained when assuming constant spectral phase.

In the time domain, we can use a more intuitive description of pulse behavior through using instantaneous frequency[37]. Non-zero temporal phase means, that the frequency of the electric field in the pulse is time-dependent and different from the central frequency. This frequency difference is a derivative of the temporal phase.

We can define the instantaneous frequency as:

$$\omega_{inst} = \omega_0 + \frac{\mathrm{d}\phi(t)}{\mathrm{d}t} \tag{2.3}$$

This description not only can tell us how the oscillation frequency of the electric field changes under its envelope, but also how the spectral content of the subsequent parts of the pulse changes. This facilitates the description of phenomena influencing the frequency distribution under the envelope, such as dispersion or self-phase modulation.

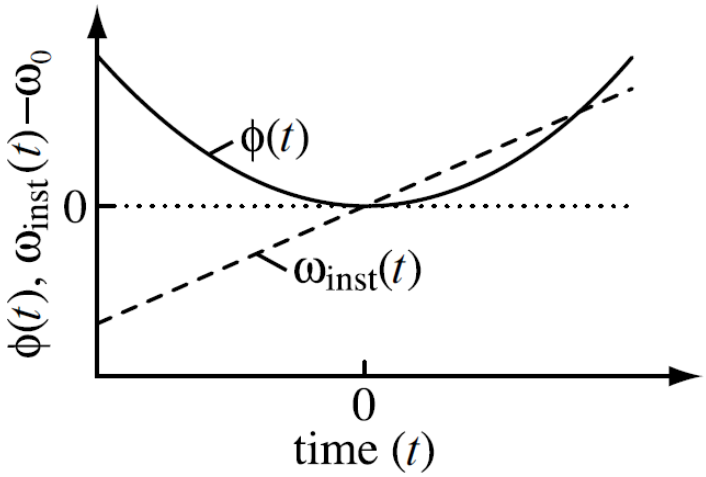

Figure 2.1: Phase (solid line) and instantaneous frequency (dashed line) for normal dispersion[37].

Light is propagating in vacuum with a constant velocity of $c = 299\ 792\ 458$ m/s, independently of the electromagnetic wave oscillation frequency. However, while propagating through a material, different wavelengths experience different phase delays, due to the frequency dependent refractive index. This phenomenon, called dispersion, is due to the non-instantaneous interaction of light with atoms and translates into an effective decrease of the light propagation velocity through the medium.

Wave vector can be expressed as:

$$\beta(\omega) = \frac{\omega}{c} n(\omega) \tag{2.4}$$

where $n(\omega)$ is the frequency-dependent refractive index.

Influence of dispersion can be described mathematically through Taylor-expansion of the wave vector around its central frequency[38]:

$$\beta(\omega) = \beta(\omega_0) + \beta_1(\omega - \omega_0) + \frac{1}{2}\beta_2(\omega - \omega_0)^2 + \frac{1}{6}\beta_3(\omega - \omega_0)^3 + ... + \frac{1}{n!}\beta_n(\omega - \omega_0)^n \tag{2.5}$$

where the coefficients $\beta_1, \beta_2, \beta_3$ are defined as follows:

$$\beta_1 = \frac{\mathrm{d}\beta(\omega)}{\mathrm{d}\omega} = \frac{1}{v_g}$$

$$\beta_2 = \frac{\mathrm{d}^2\beta(\omega)}{\mathrm{d}\omega^2} = \frac{d}{d\omega}\left(\frac{1}{v_g}\right) \tag{2.6}$$

$$\beta_3 = \frac{\mathrm{d}^3\beta(\omega)}{\mathrm{d}\omega^3}$$

The pulse envelope is traveling with the group velocity v_g connected with parameter β_1, while β_2 is responsible for pulse broadening and denotes group-velocity dispersion (GVD). The β_3 parameter is referred to as third-order dispersion. For describing most of the ultrafast phenomena it is sufficient to stop the expansion at second or third order. While GVD causes uniform broadening of the pulse temporal intensity profile, third-order dispersion also introduces modulations in the pulse structure.

Dispersion plays an important role in pulse propagation because its frequency components travel within the material with different velocities. The bigger is the frequency difference, the more different are the velocities (outside of special cases, like birefringence). Thus,

the influence of dispersion is stronger, the shorter the pulse is.

In conditions of normal dispersion the low frequencies move towards the front of the pulse and the high frequencies towards its back. When the opposite occurs, we call it anomalous dispersion. Due to the similarity to bird's singing, we call a pulse with a time-dependent frequency distribution, a chirped pulse. Pulse has a positive chirp after traveling through a medium with normal dispersion, and a negative chirp in the case of a material with anomalous dispersion.

The definition of chirp is connected with previously defined instantaneous frequency. Linear chirp occurs when the instantaneous frequency is linearly dependent on time, that is when the temporal phase is quadratically dependent on time. Such a situation is shown in the figure below, where GVD is causing pulse duration broadening through the linear shift of the constituent frequencies, in such a way that the low frequencies, shown in Figure 2.2 as red are ahead of the blue frequencies.

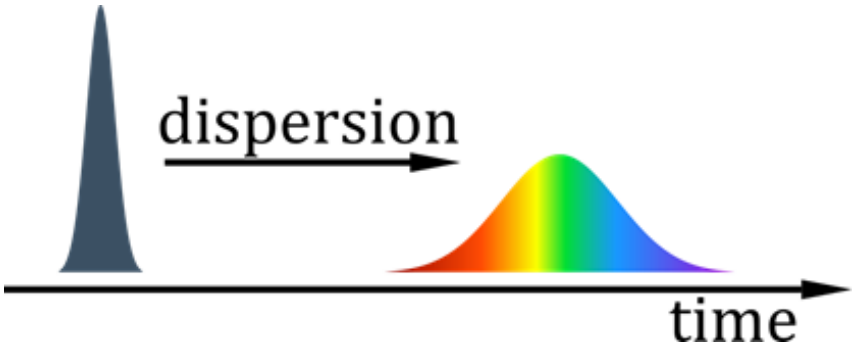

Figure 2.2: Influence of normal dispersion on the frequency distribution within an ultrashort pulse.

When we know the spectral phase of the pulse, we can compensate for the dispersion previously introduced by the propagation through some medium, using an optical compressor[37]. The compressor can be built for example from a set of diffraction gratings[39], optical prisms[40], or chirped mirrors[41].

Prism compressor operation is shown in Figure 2.3. Single prism causes different wavelengths to propagate at different angles, but the full compressor is built in such a way as to make different wavelengths leave it in the same spatial direction, but with different temporal delays.

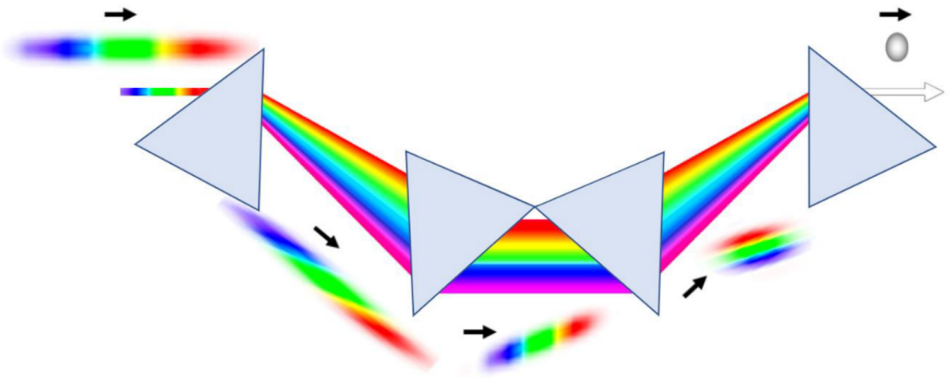

Figure 2.3: Prism compressor setup together with representation of the changes that the chirped pulses is going through during transmission through the prisms. In practice, instead of four prisms only two are used with a mirror at the end that reflects the beam back through the prisms.

Negative dispersion introduced by the compressor is caused by red light traveling a longer path in the second and third prism than the blue light. In addition to that, the third and fourth prisms remove the spatial chirp caused by prisms second and third, and angular chirp introduced by the first prism. In practice, instead of a set of four prisms, we use a flat mirror after the second prism, and the beam returns, following its previous path.

If the normally dispersed pulse travels through such a prism setup with appropriately chosen materials and distances, the output pulse will be temporally compressed. If the initial phase of the pulse didn't contain significant amounts of higher-order components, then in this way we can obtain a pulse close to being transform-limited.

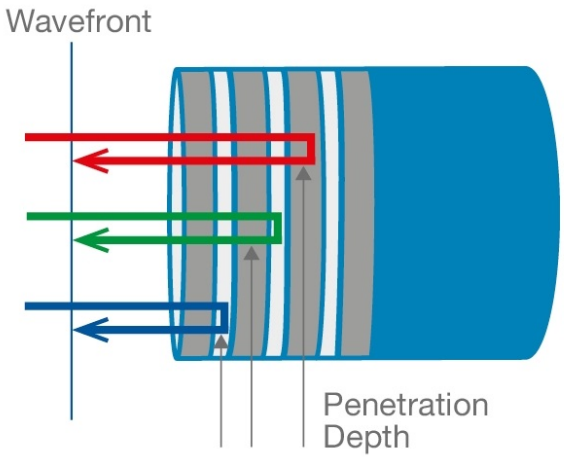

Figure 2.4: Chirped mirror working principle. Different wavelengths are reflected within different penetration depths, effectively compressing the pulse on the output.

When the pulse that we want to compress has a very broad spectrum, a set of chirped mirrors is more optimal. As shown in the Figure 2.4, a chirped mirror is a stack of alternating dielectric materials with varying thickness, that through interference effects on reflection, cause a larger delay for long wavelengths than for short wavelengths, thus compressing the pulse. Because of its mechanism, a single chirped mirror introduces residual phase oscillations. These can be suppressed by using a pair of complementary mirrors.

2.2. Nonlinear optics

In the previous sub-chapter we have introduced the description of ultrashort pulses and discussed the main phenomenon governing their linear propagation: dispersion. As the short durations of those pulses allow for very high peak powers, in this sub-chapter we describe the main phenomena of nonlinear optics that are useful to manipulate the properties of femtosecond pulses for use in transient absorption measurements. We will discuss first the nonlinear polarization expansion in general, and then specifically the sum-frequency and second harmonic generation, as well as difference-frequency and parametric amplification and application in a non-collinear optical parametric amplifier (NOPA).

We start with a simple description for a linearly polarized plane wave which during propagation in a medium induces a polarization, which we expand into a power series which allows for the dependence of the polarization on the strength of the electric field [42].

$$P = \epsilon_0[\chi^{(1)}E + \chi^{(2)}E^2 + \chi^{(3)}E^3 + ...] \tag{2.7}$$

where the terms proportional to higher powers of E represent the nonlinear polarization, with the coefficients χ called nonlinear susceptibilities. Nonlinearities in light-matter interaction may arise due to the motion of bound electrons, vibrational or rotational motion, optically induced acoustic waves, thermal effects, and others. Here we are interested in those related to bound electron motion in a transparent medium, since the nonlinear response of those is very fast, on the order of 1 fs (1 femtosecond = 10^{-15} seconds).

If we assume as input to a nonlinear medium two fields at frequencies ω_1 and ω_2, we can write the electric field as:

$$E = \frac{1}{2}[\tilde{E}(\omega_1)e^{i\omega_1 t} + \tilde{E}(\omega_2)e^{i\omega_2 t} + c.c.] \tag{2.8}$$

Then, the second-order nonlinear polarization becomes:

$$\begin{aligned} P_{NL}^{(2)} =& \frac{\epsilon_0}{4}\{\chi^{(2)}(2\omega_1 : \omega_1, \omega_1)\tilde{E}^2(\omega_1)e^{i2\omega_1 t} + \chi^{(2)}(2\omega_2 : \omega_2, \omega_2)\tilde{E}^2(\omega_2)e^{i2\omega_2 t} \\ &+ 2\chi^{(2)}(\omega_1 + \omega_2 : \omega_1, \omega_2)\tilde{E}(\omega_1)\tilde{E}(\omega_2)e^{i(\omega_1+\omega_2)t} \\ &+ 2\chi^{(2)}(\omega_1 - \omega_2 : \omega_1, -\omega_2)\tilde{E}(\omega_1)\tilde{E}^*(\omega_2)e^{i(\omega_1-\omega_2)t} \\ &+ \chi^{(2)}(0 : \omega_1, -\omega_1)\tilde{E}(\omega_1)\tilde{E}^*(\omega_1) + \chi^{(2)}(0 : \omega_2, -\omega_2)\tilde{E}(\omega_2)\tilde{E}^*(\omega_2)\} \\ &+ c.c. \end{aligned} \tag{2.9}$$

From this expression, we can notice various second-order processes that can happen due to this nonlinearity, such as second harmonic generation (SHG) ($2\omega_1$ and $2\omega_2$), sum- and difference- frequency generation ($\omega_1 + \omega_2$ and $\omega_1 - \omega_2$, SFG and DFG, respectively), and optical rectification ($\omega = 0$). While the above expression considers monochromatic plane waves, this formalism can be extended to gaussian beams with ultrashort pulses as well, with some additional considerations. The processes of SFG and DFG, also called optical parametric amplification (OPA), are shown in Figure 2.5.

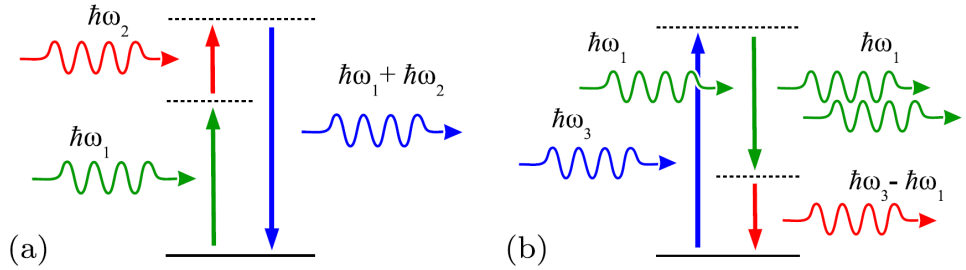

Figure 2.5: Second order nonlinear interactions, (a) sum-frequency generation and (b) optical parametric amplification[43].

The special case of sum-frequency generation - second harmonic generation is a process where an incoming pulse creates a pulse at double the central frequency so at half the wavelength of the fundamental beam. For the SHG to be efficient, the 2ω field contributions generated at different locations of the nonlinear medium, need to coherently add when exiting the crystal. The technique ensuring a proper phase relationship between the interacting waves is called phase matching.

We can define phase mismatch for SHG as:

$$\Delta k = k_3 - k_2 - k_1 = k_{2\omega} - 2k_\omega = \frac{2\omega_0}{c}(n_{2\omega} - n_\omega) \tag{2.10}$$

where k_ω is the wavevector of the fundamental, and $k_{2\omega}$ of the second harmonic beam.

Phase mismatch in a dispersive environment of the nonlinear crystal will not generally be close to zero ($n_{2\omega} \neq n_{\omega}$), thus we will not observe an efficient SHG effect if additional measures are not taken, and the energy will just oscillate back and forth between fundamental and second harmonic wave, rather than consistently being transferred to the higher frequency beam.

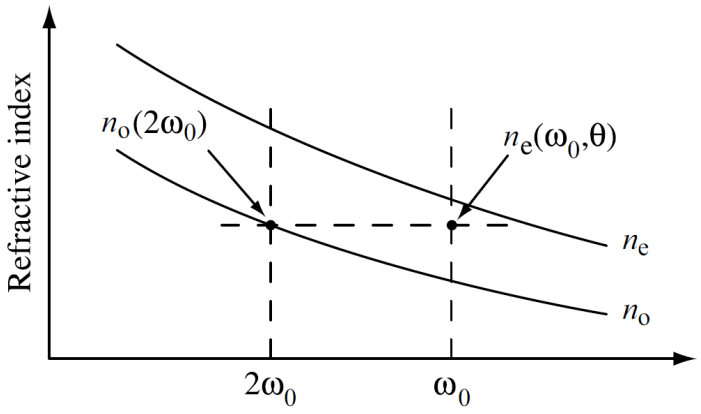

Figure 2.6: Phase matching diagram for second harmonic generation in a positive uniaxial crystal for type I phase matching[37].

The most commonly used type of phase matching is birefringent phase matching, where the refractive index seen by the wave at frequency ω and 2ω can be made equal by choosing the appropriate angle of propagation of the beams inside the birefringent crystal (as shown in Figure 2.6). We distinguish type I phase matching, where the two fundamental beams have the same polarization (as in the case of SHG) and produce a beam at perpendicular polarization, and type II phase matching, where the fundamental beams have different polarizations. By choosing appropriate phase matching conditions we can select a nonlinear process that we want to make efficient, while the others will have negligible efficiency.

2.3. Optical parametric amplification

The process of DFG can also be considered as optical parametric amplification (OPA) if both signals ω_1 and ω_3 are present at the input[43]. When ω_3 is the higher frequency beam, we call it the pump and call the ω_1 beam, the seed. In the OPA process, the seed gets amplified, by splitting the pump photons into photons of the seed wavelength and the photons of the ω_2 idler beam that is created to preserve the energy conservation:

$$\hbar\omega_3 = \hbar\omega_2 + \hbar\omega_1 \tag{2.11}$$

The energy conservation here is not enough, to have an efficient amplification, we need to also satisfy the phase-matching condition for the interacting beams:

$$\Delta k = k_3 - k_2 - k_1 \tag{2.12}$$

By appropriate choice of the ω_1 frequency and the phase-matching condition (angle of the crystal in birefringent phase matching), we can thus obtain energy transfer from an intense fixed frequency pump beam into a tunable frequency low intensity signal beam, amplifying it and making it useful for applications requiring higher intensities at wavelengths that are difficult to reach for laser amplifiers. Moreover, if the phase-matching condition is properly chosen in the OPA process we can fulfill it for a broad range of frequencies. Therefore, not only we can transfer energy into a tunable frequency beam, but also for pulsed beams, we can obtain a transfer from a narrowband beam to a broadband one, and this way generate pulses significantly shorter than the pump pulse.

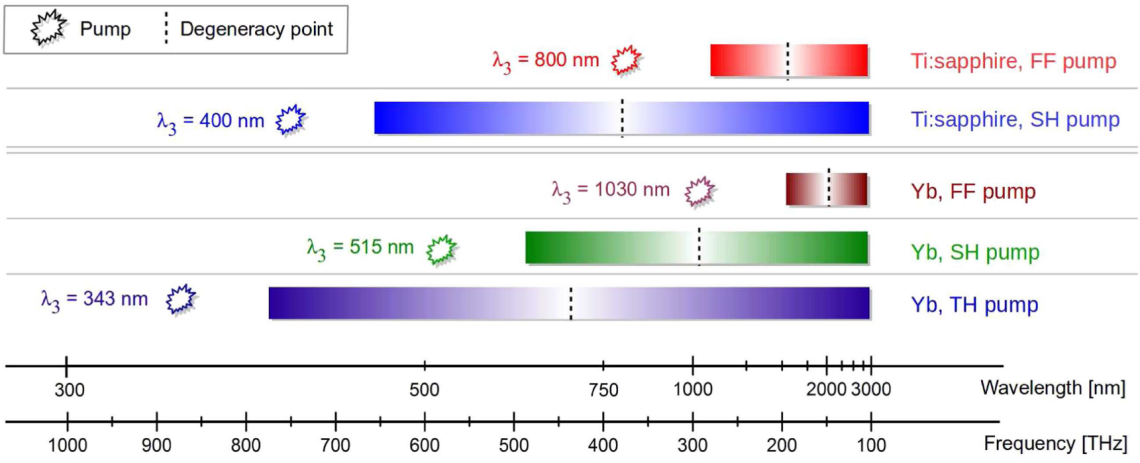

Figure 2.7: Tuning ranges of a beta barium borate (BBO) based OPA with Ti:Sapphire and Ytterbium lasers and their harmonics[43].

OPA setup usually consists of three stages:

- seed pulse generation stage, where starting from the fraction of the fundamental pulse or its harmonic, we obtain a weak pulse that initiates the amplification process, most often generated by white light continuum generation process, described in the next section
- parametric amplification stage, where frequencies selected from the seed pulse are amplified using energy from the fundamental pulse or its harmonic

- compression stage, where the amplified signal pulse has its dispersion originating mainly from the white light generation process and the propagation in the nonlinear crystal compensated, to obtain the pulse duration close to the transform limit; as discussed previously this can be done using chirped mirrors pair or prism pair

As already mentioned, in the general case phase matching is required for efficient energy transfer from the pump into the signal beam. For pulsed beams, to have broadband amplification, we need to keep the phase-matching condition fulfilled over a large bandwidth. One approach is first-order Taylor expansion of the Δk equation, for the fixed pump frequency (so assuming narrowband pump pulse) and considering the signal frequency as $\omega_1 + \Delta\omega$, and due to energy conservation the idler frequency as $\omega_2 - \Delta\omega$, we can find that the wavevector mismatch becomes:

$$\Delta k \approxeq \left(\frac{1}{v_{g_1}} - \frac{1}{v_{g_2}}\right)\Delta\omega = \delta_{12}\Delta\omega \tag{2.13}$$

where δ_{12} is the group velocity mismatch (GVM) between the signal and the idler pulses. This shows, that the broadest phase-matching condition, for any $\Delta\omega$, is obtained when $\delta_{12} = 0$, so when the signal and the idler have matched group velocities. For collinear phase matching this is best fulfilled for Type I phase matching at degeneracy, so when signal and idler have the same frequency and polarization and so the same group velocity. This happens at half the frequency of the pump.

If we want to achieve broadband phase matching without being constrained by staying close to degeneracy, we should consider non-collinear phase matching. If we again expand the Δk equation for $\Delta\omega$ detuning, but now in its vectorial form, after transformation we obtain a simple expression:

$$v_{g_1} = v_{g_2}\cos\Omega \tag{2.14}$$

where Ω is the angle between directions of the signal and idler, which tells us that to obtain broadband phase-matching in non-collinear case, the signal group velocity has to be the projection of the idler group velocity and by properly choosing the angle Ω, the group velocity matching can be realized. The comparison of the overlap of the signal and idler pulses in the case of collinear and non-collinear propagation is shown in Figure 2.8.

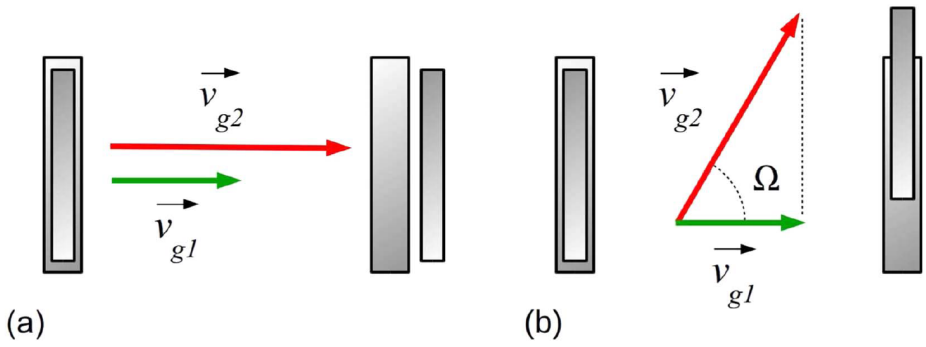

Figure 2.8: Schematic representation of signal and idler pulses during propagation in the gain medium of an OPA. (a) Colinear configuration results in a temporal walk-off of the pulses. (b) The angle Ω satisfying the equation 2.14 keeps the signal and idler temporally overlapped and allows broadband amplification [43].

Non-collinear optical parametric amplifier having superior bandwidth for phase-matching allows us to generate ultrashort pulses tunable in a broad spectral region. This makes it a perfect source for pump pulses for time-resolved spectroscopies. In UV spectral region, where it is more challenging to realize a NOPA, we can instead use the second harmonic of the pulses generated from a broadband visible NOPA. If we would consider in more detail a situation for broadband pulses SHG, we would similarly find that a big role is played by group velocity matching condition. GVM is depending both on the crystal and the wavelengths used, typically increasing with decreasing wavelength, especially at wavelengths close to the absorption edge. For these reasons to preserve as much of the NOPA bandwidth as possible in the SHG process, the total GVM can be reduced by using thinner crystals.

2.4. White light generation

Despite low energies (on the order of nanojoules), because of their short duration, ultrashort pulses have very high peak powers (on the order of megawatts). For this reason, third-order nonlinear effects also play an important role in their propagation through basic optical media like air or glasses. The most important third-order nonlinear optical phenomenon is the dependence of refractive index on intensity, which results in the self-phase modulation (SPM) effect [42].

Similarly as dispersion is a refractive index dependence on frequency, which broadens the intensity envelope in time, SPM is a refractive index dependence on intensity and it broadens the frequency spectrum in time.

During the interaction of high intensity light with electrons, a new, nonlinear phase delay shows up, giving a total formula for the refractive index as:

$$n = n_0 + n_2 I(t) + n_4 I(t)^2 + ... \tag{2.15}$$

where n_2 is called the nonlinear refractive index, and in most cases we can omit n_4 and higher nonlinearities. Nonlinear index of refraction is usually a positive value on the order of $10^{-20}\ m^2/W$.

If the n_2 value is known, we can find the nonlinear phase change due to the pulse propagation through a medium as:

$$\Delta\varphi = \frac{2\pi d}{\lambda} n_2 I(t) \tag{2.16}$$

where d is the distance and λ is the wavelength.

We can see that the nonlinear phase change depends on the time dependence of the intensity, and for a pulse with an initial flat temporal phase and in absence of other effects, the phase will take the shape of the pulse intensity profile. If we calculate the Fourier Transform of such a pulse, we will see that its spectrum got broadened, while its temporal intensity profile stays unchanged.

One important application of the self-phase modulation effect is generation of ultrabroadband optical spectra in the process of white light generation. As SPM is the result of intensity-dependent refractive index in the time domain, the n_2 parameter is also influencing the change of spatial phase of the beam depending on the spatial intensity distribution.

For a high intensity gaussian beam, this self-focusing effect will cause the pulse to locally modify the material making it equivalent to a transient lens. The beam getting focused then increases its intensity which drives the self-focusing even more and may lead to beam collapse. On the other hand, if the parameters of the beam are suitably chosen, the plasma generated by the high intensity pulse can exactly balance the self-focusing effect by defocusing and start a formation of a plasma filament which acts as a waveguide.

A strongly focused beam then can travel through such a waveguide while continuously broadening its spectrum due to SPM and a combination of other nonlinear effects. By choosing an appropriate crystal as the nonlinear medium and optimizing the numerical aperture and intensity, in this way we can obtain a broad stable spectrum in the region of interest, while preserving its spatial and temporal coherence.

2.5. Principles of transient absorption spectroscopy

Now that we discussed all of the most relevant nonlinear phenomena used for generation and shaping the ultrashort pulses, we can move to basic principles of transient absorption spectroscopy[44–46].

Our goal is to study the excited state evolution of various materials. For this purpose, we will need a pulse called the pump, which brings some population vertically from the ground state to the excited state and in this way starts the dynamics. The pump pulse ideally has high intensity and a tunable spectrum to selectively excite chosen states. Its duration is also an important part of defining the temporal resolution of the whole spectroscopic measurement. Such parameters are best obtainable using a NOPA.

The second pulse that we use in a TA measurement is called the probe. This pulse arrives at the sample delayed with respect to the pump pulse, and interrogates the current state of the dynamic processes happening within the material. We want the probe pulse to have weak intensity, not to perturb those processes, and a broadband spectrum so that we can see as many different processes as possible. The pulses created using the white light generation technique fit this description very well.

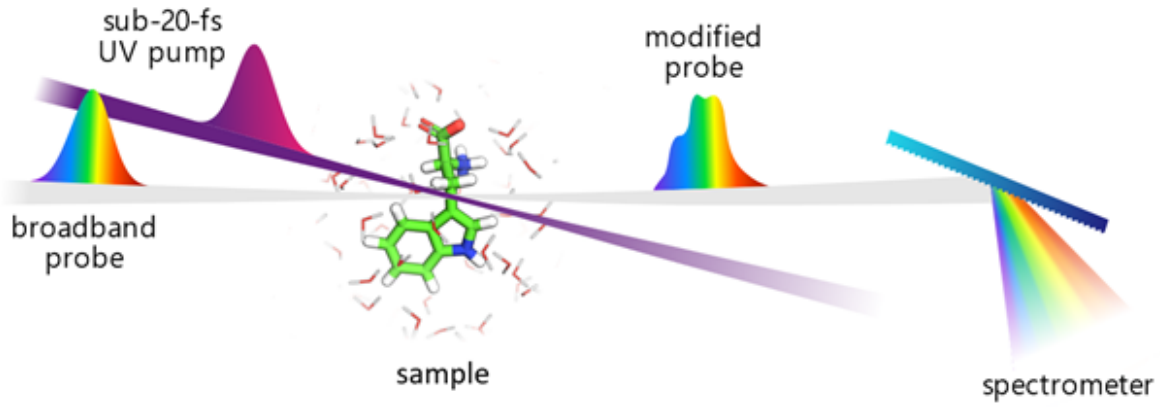

Figure 2.9: Schematic representation of a pump-probe geometry used in this work. Ultrashort UV pulse pumps the sample to the excited state and the delayed broadband probe pulse interrogates the current state of the sample modifying its spectrum in the process. The differential spectrum for each delay between the pump and the probe is recorded via spectrometer and represents a dynamic 'movie' of the excited state behavior.

In this work, we apply the pump-probe geometry for transient absorption measurements as shown in Figure 2.9, using a second harmonic of the NOPA as an ultrashort UV pump, and a chirped white light pulse as the probe. The pulses arrive at the sample in the sequence of: pump-probe-nothing-probe, in this way we can subtract a reference spectrum of the pulse that passed through a sample in the ground state from the pulse that interacted with the excited sample. We record such a differential spectrum for each pump-probe delay, modified with the mechanical delay stage, to obtain a kind of molecular movie of the spectral evolution since the time of excitation. The measured differential transmission signal is expressed as:

$$\frac{\Delta T}{T}(\lambda,\tau) = \frac{T_{ON}(\lambda,\tau) - T_{OFF}(\lambda)}{T_{OFF}(\lambda,\tau)} \tag{2.17}$$

which can also be represented as differential absorbance:

$$\Delta A(\lambda,\tau) = -log\left(\frac{\Delta T}{T}(\lambda,\tau) + 1\right) \tag{2.18}$$

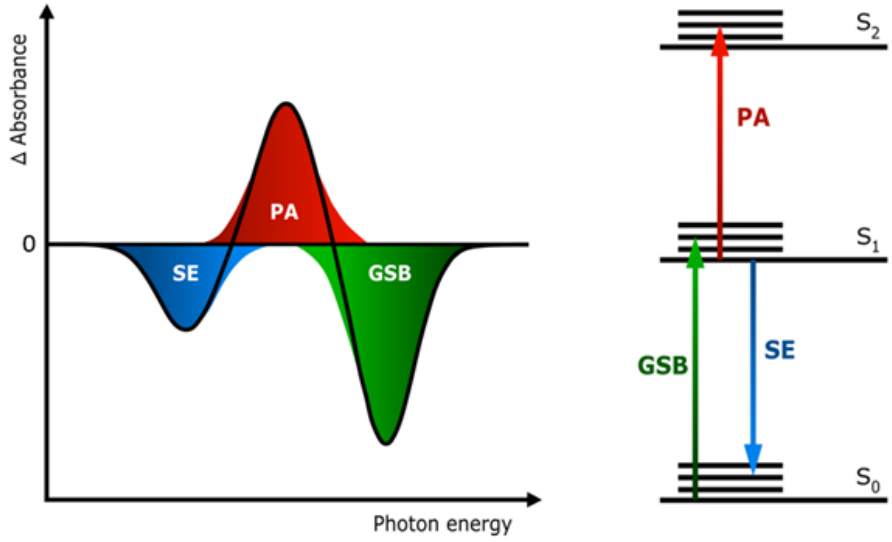

Figure 2.10: Example of a TA spectrum comprised of SE, PA and GSB signals, together with corresponding transitions.

During the measurement, we record the differential transmission spectrum, which can be later converted into differential absorbance. The Figure 2.10 presents the three main kinds of signals that can be observed in a TA measurement: stimulated emission (SE), photoinduced absorption (PA) and ground state bleach (GSB). The SE signal appears as negative absorption change due to emission of additional photons into the beam, coming

from the transition back down to the ground state. The PA signal is a positive absorption change and comes from transitions from the currently excited state to some higher lying states. Finally, the GSB signal is again a negative signal, showing the increased transmission at the pump wavelengths due to depletion of the ground state population through the pump pulse.

Those three transient signals then evolve over time as the excited state relaxes. Figure 2.11 shows an example of a TA map spanning 2 ps, and a corresponding simplified energy level scheme. At time zero, the wavepacket resting in the ground state is vertically excited to the Frank-Condon (FC) region (position 1 into 2). Following the excitation, we observe appearance of two broad spectral bands, negative SE, and positive PA1, as the wavepacket moves on the S_1 PES (position 3). The decay of the SE and PA1 signals signifies the transfer of the wavepacket via the CI to the ground state (position 3 into 4). Simultaneously we can see the rise of the PA2 signal due to the population of the ground state vibrational energy levels, called hot ground state. As the wavepacket settles down at the minimum of the ground state, giving energy away to the solvent through vibrations, the PA2 signal blue-shifts and decays.

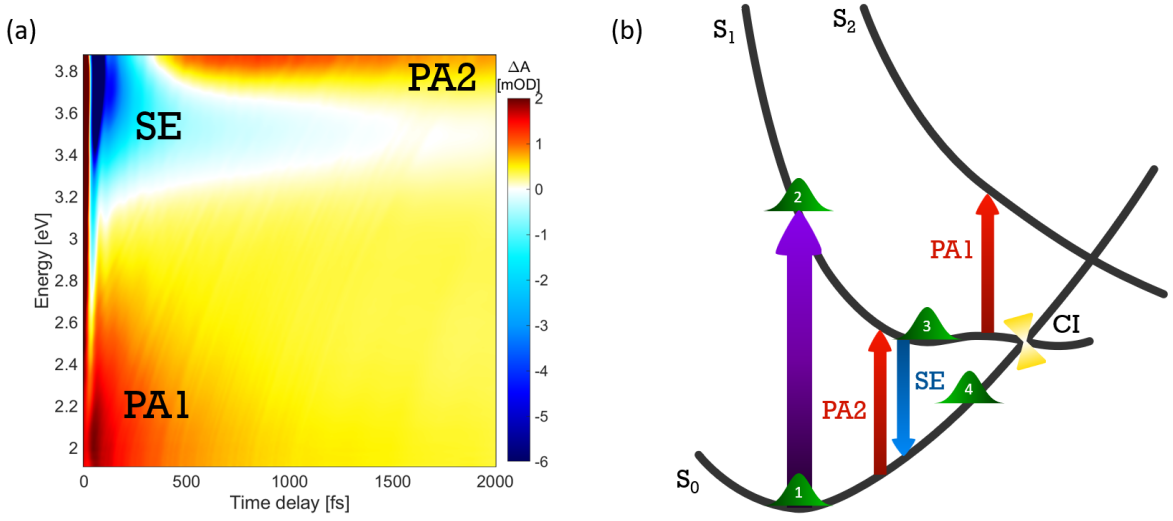

Figure 2.11: Example of a nucleoside TA map (a) and a corresponding schematic PES diagram (b). Positions of the wavepacket are numbered according to sequence after excitation.

This scheme displays simple interpretation of the decay of the transient signals to characterize the timescale of the transition through CI. In full analysis, we would have to include proper fitting of the decay timescales as well as consider other pathways, such as population of the dark $n\pi^*$ states. To disentangle the evolution of complex transient

spectra over time, we use global fitting. Instead of fitting for a single decay trace and finding a time constant and an amplitude, we fit whole spectra with their corresponding time constants. The fitted spectra can then be more easily assigned to the evolving states. Global analysis of the data presented in this thesis has been done using Glotaran software[47].

If the excitation pulse is sufficiently short, which also means it has a broadband spectrum, it may generate vibrational coherences in the sample. With high enough temporal resolution of the experimental setup, such oscillations can be recorded as a modulation of the above mentioned signals of SE, PA, or GSB. As shown in Figure 2.12, the oscillating wavepacket, either in the excited or ground state, will continuously change the energy of transition up or down and this will shift the spectral peak recorded in TA measurement periodically. If we track the intensity change for a specific wavelength and calculate its Fourier Transform, we can find the vibrational spectrum exhibited by the sample and track its evolution in real time, just as the electronic TA signals[48].

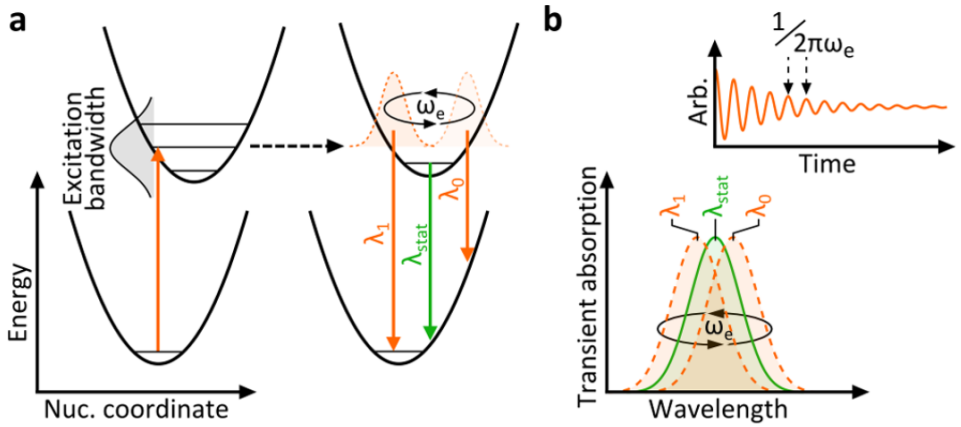

Figure 2.12: Idea of impulsive vibrational spectroscopy. (a) Ultrashart and thus spectrally broadband pulse generates vibrational coherence during photoexcitation. (b) The evolving vibrational state shows oscillatory modulation of the emission spectrum at the corresponding frequency[48].

As mentioned, the modulation related to vibrational motion can be connected to various transitions. Usually, we can observe isolated peaks appearing on top of the TA signal related to a specific transition. In addition to that, as you can see in the above figure, we expect to see a π phase jump across the wavelength that corresponds to the static emission or bleach. This phase jump is related to the oscillations being out of phase for the wavelengths on the opposite sides of the central one.

2.6. Coherent artifacts

Coherent artifacts are signals recorded in transient absorption measurements originating from nonlinear interaction between the pulses during their temporal overlap in the sample, solvent, substrate, or cuvette. Such effects arise during the application of short lasers pulses which have very high power densities that can lead to two-photon absorption (TPA) or stimulated Raman amplification (SRA), and together with the application of spectrally broad and chirped probe pulses, such as white light continuum provide suitable conditions for efficient cross-phase modulation (XPM)[49–51].

In this chapter, we focus on discussing the TPA and XPM effects, which are the ones present in experiments discussed in this work, while we didn't observe SRA, which may occur when the excitation wavelength is located close to the probe wavelength. The artifacts are very short in duration, comparable with the temporal width of cross-correlation function of the pulses, as they are produced through a simultaneous action of two photons, one coming from the pump and one from the probe. In XPM phase changes are induced on the probe pulse by the intense photons of the pump pulse through modification of the refractive index, as discussed previously for the case of SPM. For high intensities of the pump, absorption of one pump photon and one probe photon will give rise to TPA. The interchange of photons between the pulses through a vibrational energy level of the material leads to SRA.

For low intensity UV light many solvents are transparent. However, for high-power ultrashort pulses, these materials can efficiently absorb through a multiphoton absorption process. For sufficiently high intensity pump pulse, it is possible that two photons will be absorbed by the sample through a single transition. While this effect will be the strongest for pairs of photons from the pump, what we can observe in the TA measurement will be the absorption of one photon from the pump and one photon from the probe. The sum of the energy of these photons has to correspond to some absorption band of the material, and this will often be the case for deep UV absorption of solvents and glasses when using UV-VIS probe. The TPA signal appears as a Gaussian signal assuming gaussian pump and probe pulses in a thin medium. When the medium becomes thicker or its dispersion higher, GVM will contribute to the change of the shape of the TPA artifact, broadening it first and then transforming into a top-hat pulse profile. In case of high GVD, this effect becomes more significant the further away the probe wavelength is from the pump, as shown in Figure 2.13.

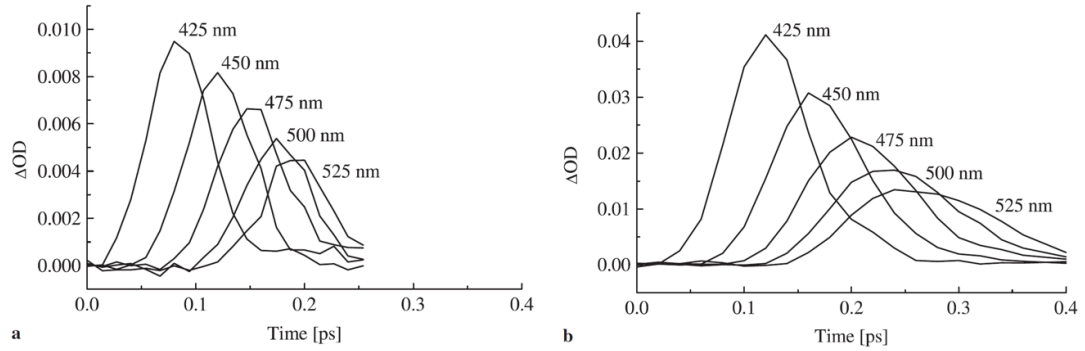

Figure 2.13: TPA signal measured in a plane-parallel (a) 0.15 mm and (b) 0.9 mm thick BK7 glass plate with 400 nm excitation. Significant stretching of the artifact for wavelengths far from the pump can be observed in the second case[49].

The XPM signal originates from the non-resonant interaction with the solvent or the cuvette windows (usually made from fused silica). It is closely related to the previously described SPM process, but in the previous case the self-action of the pulse on itself due to intensity dependent refractive index was discussed, here, it's the pump pulse affecting the probe pulse through the same mechanism. When the pulses overlap, the pump pulse modifies both its phase through SPM effect, which we cannot observe in the TA map, and the phase of the probe pulse through XPM, which we can see around time zero of the measurement. In this case, there is no net energy transfer into or out of the probe pulse, only a redistribution of spectral intensity. This leads to a change of probe transmission for a given wavelength and delay.

The greater is the chirp of the probe, the larger is the time separation between neighboring frequencies of the probe, so that fewer frequencies fall into the interval of interaction with the pump. This translates into increased XPM signal.

A common feature of XPM artifacts is their broadening and decrease in amplitude due to the group-velocity mismatch. If the spectral separation between the pulses is large enough, the maximum of the XPM signal is split in two, as shown in Figure 2.14. As the frequency is coupled to time through the chirp, the XPM looks alike in wavelength and in time domain.

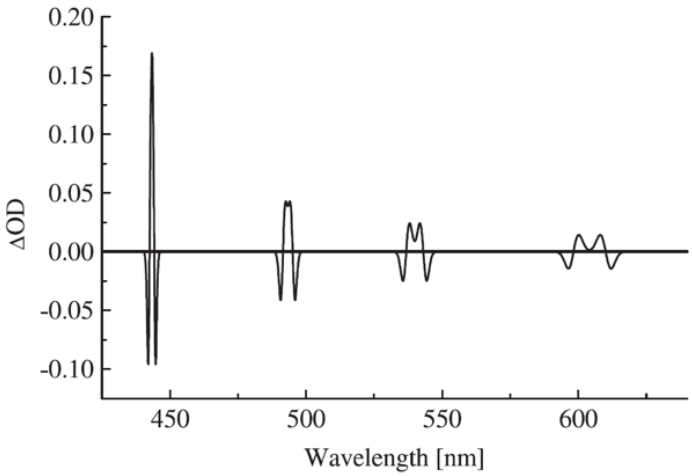

Figure 2.14: Simulation of XPM spectra at diferent time delays for a thick sample. At wavelengths further away from the 400 nm pump, we can observe artifact elongation and splitting[49].

Both TPA and XPM signals trace the temporal chirp of the white light probe pulse, which can be used to determine and then correct the time zero of the TA spectra (Figure 2.15). Moreover, their time dependence is a measure of the cross correlation function, so the compression of the pump pulse can be adjusted based on the artifact shape. The artifacts also give useful information about the group-velocity mismatch present in the medium, as their shape is known, unlike the unknown dynamics that we are trying to measure.

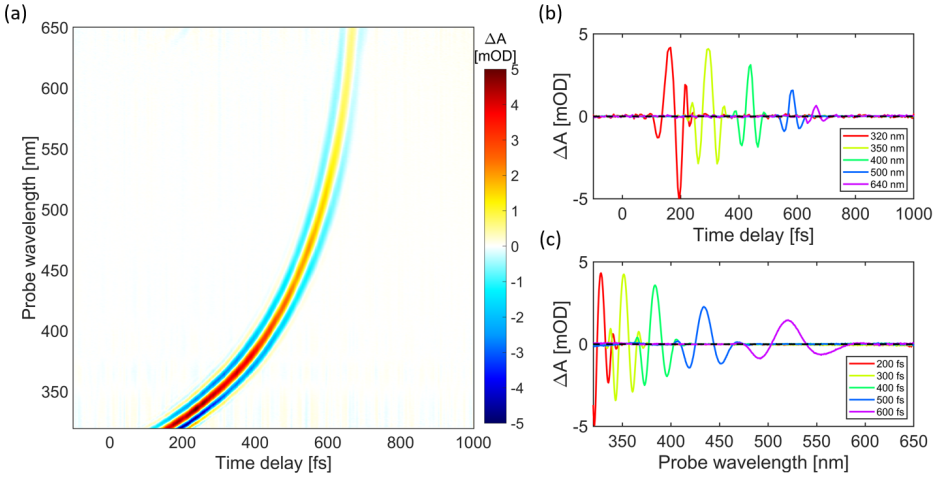

Figure 2.15: XPM artifact measured in 0.15 mm water jet without chirp correction. TA map (a), dynamics (b) and spectra (c). The duration of the artifact stays roughly the same over the probing wavelenghts thanks to the thin sample path.

3 | Experimental setup

In this chapter, the experimental setup used for all of the measurements done in this work is described. Firstly the general layout of the setup is discussed, as designed by the authors of Borrego-Varillas et al.[52] and rebuilt by the author. Then, the details of improved sample delivery methods are discussed, such as a new wire-guided jet or the considerations for high temporal resolutions in cuvettes.

3.1. Setup layout

The setup, shown in Figure 3.1, is seeded with the fundamental beam at 800 nm wavelength and 1 kHz repetition rate coming from the regeneratively amplified Ti:Sapphire laser system (Libra, Coherent), which emits vertically polarized 100 fs pulses. A fraction of the laser power is split between the UV pump generation stage and the white light generation stage. The UV generation stage, containing the NOPA, SHG, and the compressors, is driven by 500 μJ 800 nm pulses, while a 35 μJ portion of the fundamental is sent through the computer-controlled delay stage into the probe generation part. After the generation of suitable pump and probe pulses, the pump pulse is modulated by a mechanical chopper and the two pulses are focused onto the sample with spherical mirrors. While the delay between the pulses is varied through the movement of the delay stage, the spectrometer records the changes in the probe spectra due to the interaction with the sample.

The UV generation is comprised of a broadband visible NOPA with chirped mirror compressor and an SHG stage with a prism compressor. The NOPA is presented in Figure 3.2. The entering 800 nm light is split into two beams, one enters the seed generation arm, and the other goes through a manual delay stage and is converted via SHG into 400 nm pulses used for pumping the NOPA crystal. In the seed generation arm, the standard white light generation process is used in a 2 mm thick sapphire crystal, with variable power and numerical aperture of the driving beam. The beams are then recombined on the 1 mm thick BBO crystal, where they have to overlap in space and time, as well as their angle has to match the direction of the superfluorescence cone. The temporal overlap is

adjusted by moving the delay stage, which at the same time chooses the spectral window of the white light seed to be amplified. The overlap on the face of the crystal and the angle alignment is set with the flat mirrors of the white light beam.

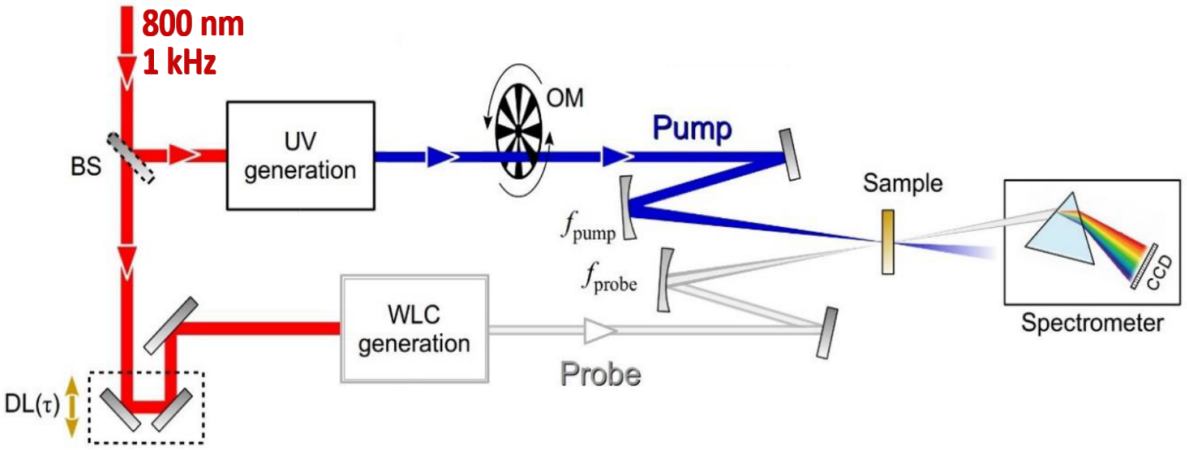

Figure 3.1: Experimental transient absorption setup[52].

The spectrum generated from the NOPA can extend from 525 to 700 nm when optimized for visible bandwidth, corresponding to a transform-limited pulse duration of 6.2 fs and energy on the order of 10 μJ. Following the generation process, the NOPA pulses are then collimated and compressed through 12 reflections between a pair of dispersion-matched double-chirped mirrors, achieving almost flat spectral phase. The output spectrum can be tuned within the 500-700 nm which allows for greater tunability of the UV pump pulse spectrum.

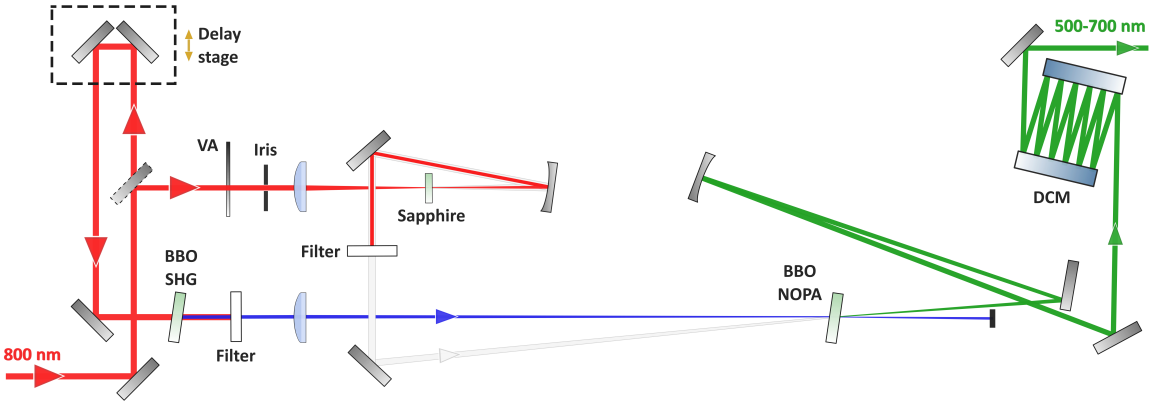

Figure 3.2: Detailed schematic of the broadband visible NOPA used for driving SHG to create the pump pulse.

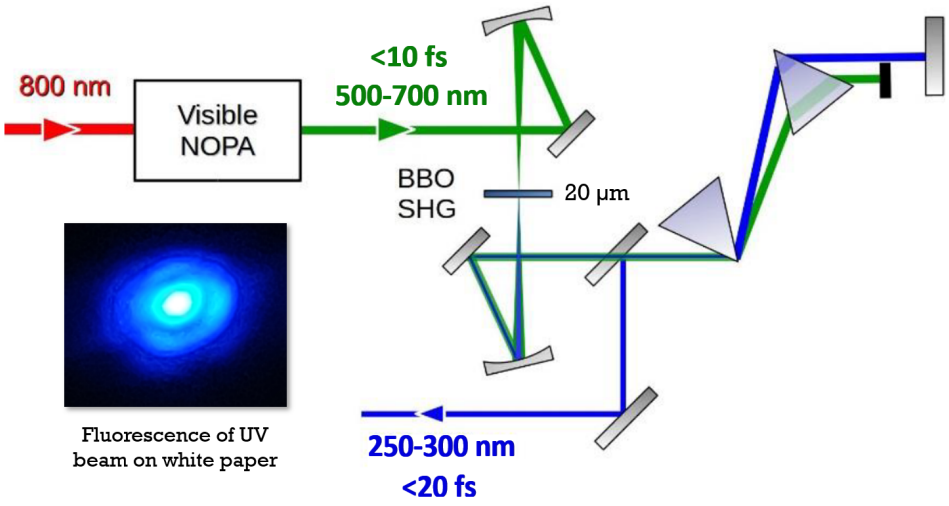

Figure 3.3: Experimental setup for generation of the UV pump pulse[52]. Fluorescence of the UV beam shown as an inset.

The broadband visible pulses are then focused onto another BBO crystal, this time cut for the SHG Type I process and with a thickness of only 20 μm. After SHG the beam is cleaned using dichroic mirrors and directed into a Brewster-cut MgF_2 prism pair, where the additional phase gathered from passing through the crystal, air, and possibly cuvette window is removed and the remaining visible light is cut off, as shown in Figure 3.3. The nonlinear interaction generates horizontally polarized UV pulses with energies ranging between 20 and 80 nJ at the sample position. Adjusting the angle of the BBO crystal for phase matching and simultaneously the spectrum amplified by the NOPA, the output can be tuned in the 250-300 nm range. Figure 3.4 below shows examples of spectra and temporal profiles retrieved from the two-dimensional spectral-shearing interferometry pulse characterization method[52,53] showing the capabilities of the pump generation setup. As we can see the pulses are sub-20-fs in duration and close to their transform limit.

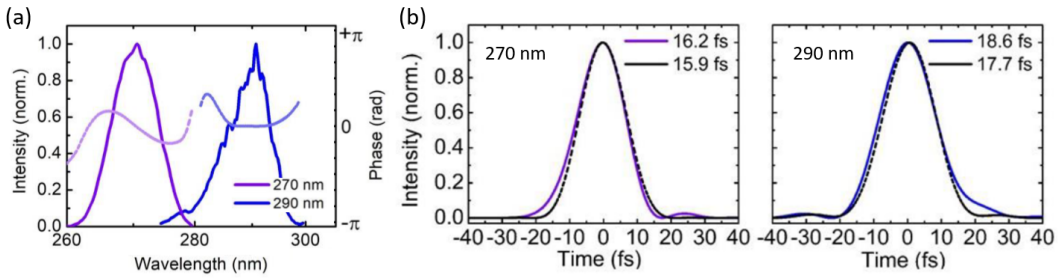

Figure 3.4: (a) Spectra of the UV pulses, and (b) corresponding temporal pulse profiles as characterized with two-dimensional spectral-shearing interferometry[52,53]. Transform-limited pulses shown as dashed lines.

The white light probe generation starts by going through a delay stage, which is used to precisely synchronize the pump and probe pulses and then change the delay between them for conducting a TA measurement. Then, the beam is sent through an iris and attenuator towards a 2 mm calcium fluoride (CaF_2) crystal (thickness optimized for the lowest dispersion) mounted on a two-axis translation stage (Zaber Technologies, T-LS28M), which continuously moves the crystal in a helical pattern in the plane perpendicular to the propagation direction so as to avoid optical damage through continuous irradiation of the same spot on the crystal. The iris, the variable attenuator, and the crystal position in the focus, are used to control the power and the numerical aperture of the beam entering the crystal, as in the case of NOPA seed generation, to adjust the parameters of the resulting white light spectrum (Figure 3.5b). The beam is then recollimated using a spherical mirror and cleaned from the leftover fundamental beam using an thin (400 μm) absorption filter (Shott BG39), and sent towards the sample. Alternatively, the white light can be generated using a second harmonic of the fundamental beam, at 400 nm, generated after the delay stage in a 1 mm thick Type I BBO crystal (Figure 3.5a). The white light pumped with 800 nm beam extends from 320 to 650 nm, and the one pumped with 400 nm, from 250 to 360 nm, giving a total 250-650 nm broad range covering the whole visible region and the UV region near the usual absorption peaks in biomolecules (Figure 3.5c).

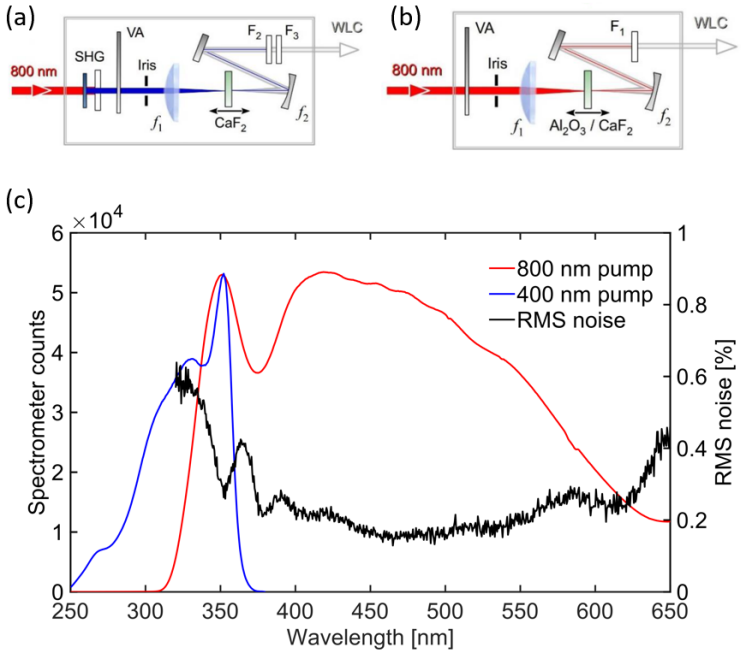

Figure 3.5: White light generation stages for (a) 400 nm pump, and (b) 800 nm pump[52]. (c) Optimized white light spectra for the two pumps together with the RMS noise profile for the 800 nm pump.

As the UV pump has horizontal polarization, because of polarization change introduced by the SHG process, the beams arrive at the sample perpendicular polarized to each other. To allow for changes of the relative polarization of the pulses, we insert a half-wave plate before the white light generation process, with which we can change the polarization of the output white light either to be polarized parallel to the pump pulses or at the magic angle (54.7 deg) at which the rotational contribution to the measured decay traces will cancel out. It is important to note that the CaF_2 crystals are always produced with some birefringence that we need to correct for when changing the input polarization, by adjusting the rotation angle of the crystal, such that it doesn't modify the polarization of the light passing through it.

The stability of the white light spectrum generated with the fundamental beam as a pump is very good. The 0.2% rms fluctuation obtained in most of the spectral region corresponds to a noise $< 10^{-4}$ for the $\frac{\Delta T}{T}$ signal when averaged over 500 consecutive pulse pairs, so in 1 second of measurement time. The high stability that we managed to achieve in this setup is crucial for UV TA measurements as in water solvent, two-photon absorption of the pump pulse produces solvated electrons which complicate the measured map with their broad and long-lived absorption spectra[54]. To minimize those spurious signals, we keep the pump fluence low and the sample thin, which decreases the maximal achievable signal intensity, thus calling for high sensitivity of the whole setup.

When they are ready, the pump and probe pulses are separately and non-collinearly focused on the sample at a small angle, using UV enhanced aluminum spherical mirrors with $f_{probe} = 200$ mm and $f_{pump} = 400$ mm as to always keep the pump spot bigger than the probe spot, such that the probe is probing an area excited by the uniform density of the pump. The pump is modulated by passing through a mechanical chopper at 500 Hz and a probe transmitted through the sample with the pump on and with pump off is recorded by the spectrometer (SP2300 Princeton Instruments, Acton) equipped with a linear CCD detector with a spectral resolution of 0.5 nm and read-out electronics (Stresing Entwicklungsburo) working in single-shot readout mode at the full 1 kHz laser repetition rate. It is important to note that even though the probe spectrum is not compressed, the high spectral resolution of the spectrometer acts as a narrowband filter on the probe pulse, and according to the resolution contributed by the probe depends on its transform-limited duration[55], which in this case is very short as we obtain very broad spectra. This allows us to skip any compression stages for the probe and simplify the setup. The existing chirp of the probe results in a dispersion of the pump-probe time delay, which is later corrected by numerical post-processing of the raw TA maps.

3.2. Sample delivery

The main technical improvement to the rebuilt setup is the design of a new wire-guided jet system. As explained before, ultrashort pulses traveling through a material media will change their shape due to dispersion effects. While in the UV spectral region even air path starts to be non-negligible, the biggest influence on unwanted stretching of the pump pulse is caused by the solvent and the cuvette window in which the sample is located. Figure 3.6 shows how the refractive index of fused silica rises sharply in the UV region.

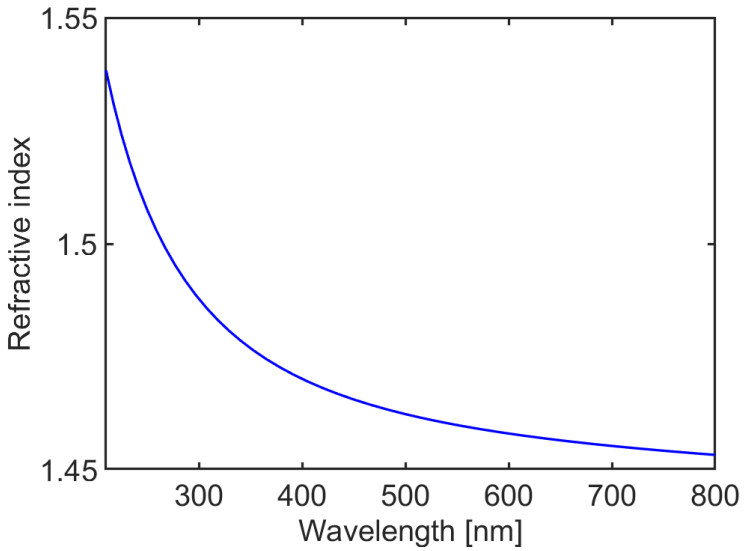

Figure 3.6: Dispersion of fused silica[56].

This dispersion not only stretches the duration of the pump pulse itself, which can be precompensated by the prism compressor to not lose resolution, but also causes GVM between the pump pulse and the probe pulse as they contain different wavelengths, which cannot be precompensated. The best solution to minimize this effect is to keep the interaction path of the pump and probe pulses inside the sample to a minimum, as then the distance over which the pulse delay will be altered is the shortest. GVM will significantly deteriorate the temporal resolution for ultrashort pulses, as the single probe pulse will interact with the sample at several different real delays with respect to the pump pulse over the interaction distance. This effect becomes stronger, as the distance between the pump and probe wavelengths increases.

This calls for keeping the thickness of the sample as short as possible. In a 1 mm thick cuvette, we will observe strong dispersive stretching of the signals, as shown for the case of TPA artifact in Figure 3.7a. While a thin cuvette with 200 μm sample path could be used, the front glass window even though it can be precompensated, will introduce an

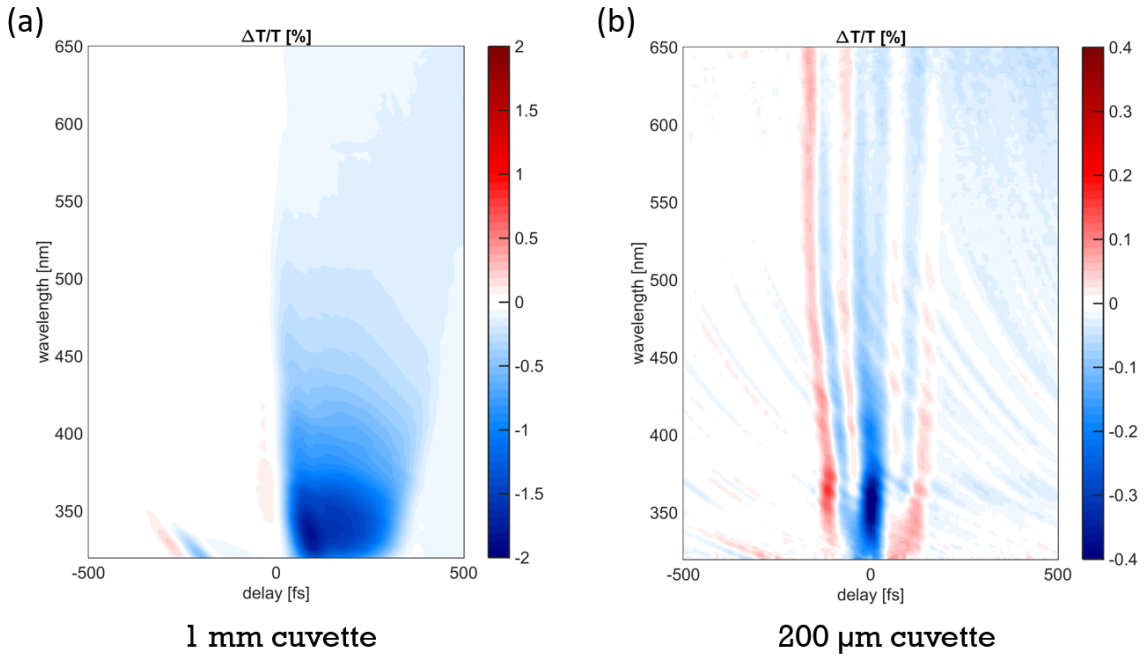

Figure 3.7: (a) TPA artifact significantly stretched due to thick (1 mm), weakly absorbing sample path. Wavelength-dependent stretching due to GVM can also be observed. (b) TPA and XPM artifact in a thin (200 μm) cuvette. The TPA signal is very sharp, but due to low absorption of the sample, XPM artifact is induced also in the back window of the cuvette, obstructing early times of the sample dynamics.

XPM artifact. In the case of sample not fully absorbing the pump pulse, also the back window will contribute to another slightly delayed XPM signal (Figure 3.7b) and overlap the earliest part of the signal, making it more difficult to interpret the dynamics.

At the same time, many samples, especially those absorbing in the UV region need to be continuously flown, as the UV can damage their structure and form photoproducts. The best solution for all of the above problems is flowing the sample in a wire-guided jet configuration[57], shown in Figure 3.8.

As shown in the figure the system comprises a custom-built holder with two steel wires guided out of it that act as rails for the laminar flow of the solvent. The dissolved sample is pumped out of the vial using a high-speed micro annular gear pump (HNP Mikrosysteme mzr-4622X1-hs-vb M2.1) that has very reduced pulsation compared to the often used peristaltic pump, through a check valve that forces a flow in one direction and into the wire holder. The liquid being pumped down the wires forms a thin layer of relatively uniform thickness that avoids any unnecessary interaction of the ultrashort UV pulses with glass. Then the sample is picked up at the bottom and pumped back to the vial.

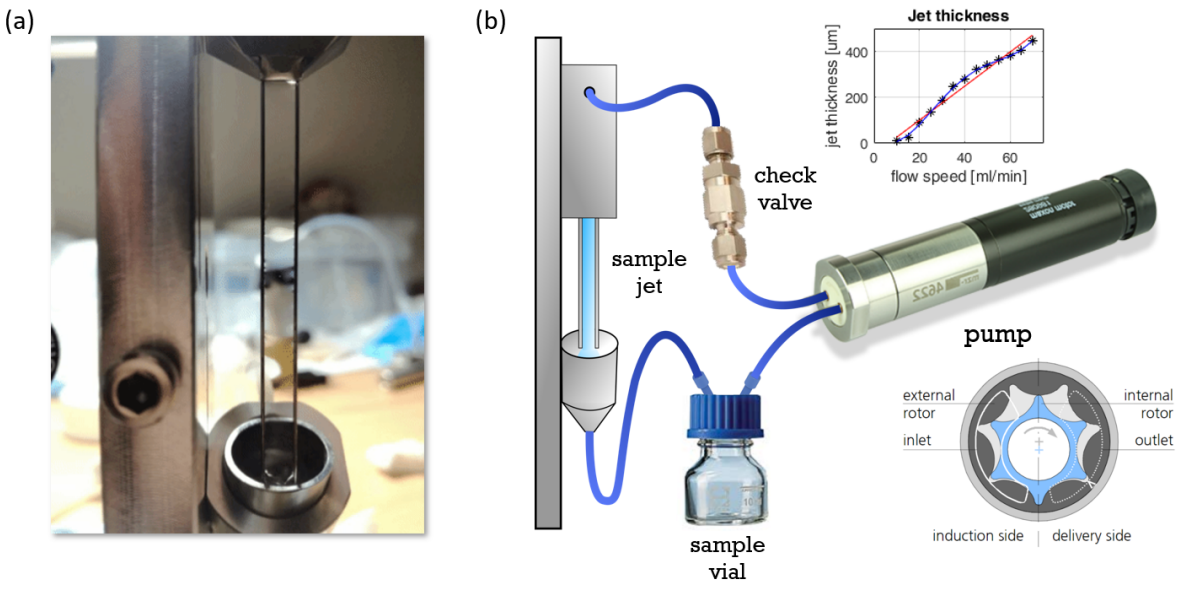

Figure 3.8: (a) Photo of the laminar jet, showing minimal distortion of objects behind it. (b) Schematic of the wire-guided jet system. Jet thickness plot and micro annular gear pump mechanism shown as insets.

In such a circulating system if the volume of the sample is enough, even if molecules get damaged, they will be continuously getting diluted in the fresh sample volume, bringing mostly undamaged samples into the interaction with the pulses. Moreover, the thickness of the jet can be varied as shown in the inset of the Figure 3.8, by changing the flow speed of the liquid, which allows for adjusting down the thickness if the sample has low absorption, to avoid the dispersive effects distorting the signal, or for adjusting it up if the signal coming from the sample is weak. The best performance has been observed around 150 μm jet thickness.

While the jet solution offers the best time resolution parameters assuming the flow is stable, in certain cases it is difficult or not possible to use it. Such cases include toxic and quickly evaporating solvents or difficult to obtain and expensive samples that cannot be easily flown in smaller volumes. In such situations often the choice is using 200 μm cuvettes with thin glass windows to minimize dispersion. The issue, as already mentioned above, is that if the sample doesn't absorb a high fraction of the pump power, this leftover pump will induce a second XPM effect in the back window of the cuvette, even if it is thin, and since its only 200 μm distance away from the first glass window, it will overlap with the early dynamics, where we often want to find some very fast time constants.

The solution for these problems is using a standard 1 mm cuvette, but with a highly concentrated sample, which we would anyway have to use if our sample thickness in the

jet is 100 μm, as to see any measurable signal. The advantage of using the 1 mm cuvette is that even if the first glass window is thicker, the dispersion inside it splits the XPM artifact into two parts, where one appears fully before time zero, so the one overlapping with the signal is reduced, and also the back window is now 1 mm away from the front window, so that the pump cannot reach it with any significant intensity to cause another XPM artifact at later times. As for the problem of the thick glass window in the front, this can be precompensated with the prism compressor.

The high concentrations are important, because the signal is only recorded when there is an overlap of the pumped region with the probe, and if the first 100 or 200 μm of the total 1 mm sample thickness in the case of the thick cuvette, absorbs almost all of the pump intensity, the total thickness of the sample doesn't matter, what matters is only the effective thickness. This way, as long as the sample can be sufficiently concentrated without affecting its structure, we can achieve very thin effective sample paths, and fully preserve the resolution of the setup, while avoiding the XPM artifact contributed from the back window of the thin cuvette and the loss of resolution of a thick sample. From practical experience the main disadvantage of this method is higher intensity artifact due to the thick front window, and having to compensate it.

4 | Excited state decay pathways of uridine and 5-methyluridine

We have discussed in Chapter 1.2 the basic photoprotection mechanism of isolated nucleosides. It is generally accepted that the excited states deactivate through CI-mediated ultrafast internal conversion to the ground state. While the general mechanism is known, the debate on the details of this relaxation is still attracting scientific interest and advancing thanks to improvements in computational and experimental techniques. It is established that the processes take place on the ultrafast timescale from both time-resolved fluorescence, photoelectron spectroscopy, and transient absorption studies as well as theoretical computations. However, the precise assignment of time constants to the relevant processes as well as the level of involvement of dark $n\pi^*$ states is not yet complete.

4.1. Open questions

In this chapter, we focus on the full description of the excited state decay dynamics of uridine (Urd) and 5-methyluridine (5mUrd), two closely related pyrimidines, as their only difference is the presence of the methyl group in the second case on the C5 position. Uridine is one of the four canonical RNA nucleosides, while 5-methyluridine, which in its deoxyribose-based form is called thymine, is the canonical base of DNA. Through this basic comparison, we can see how the addition of the methyl group to the nucleobase present in DNA modifies its response to UV radiation[11]. Even though these basic pyrimidines have been thoroughly studied over the years, the timescale of the IC and the degree of involvement of $n\pi^*$ states is still disputed. It is generally agreed that the initially excited $^1\pi\pi^*$ singlet state decays with one or two sub-ps components, and some residual longer-lived signals are also detected[7–9,21,58–67]. The observed ∼100 fs time constant has been assigned to the process involving the bright state for both pyrimidines, but there is still disagreement on whether it decays directly to the GS or through the $n\pi^*$ state[59,62,64,66]. The longer decay time has been proposed to come from several scenarios including, vibrational cooling in the GS, intersystem crossing to triplet states, or IC from previously

populated dark states to the GS.

For example, in the two recent experimental studies of Prokhonerko et al.[59] and Xue et al.[66], the thymine TA has been measured (Figure 4.1). In the first work, the ∼100 fs timescale has been missed and the longer 0.6 ps constant has been assigned to the population of an intermediate $n\pi^*$ dark state. On the other hand, in the second work, while the 100 fs constant has been resolved, it has been assigned to transition to a long lived $n\pi^*$ state, while the $^1\pi\pi^*$ state continues till the CI with the GS after 1 ps. The lack of comprehensive theoretical analysis caused in both cases an improper assignment of the measured constants, even in case of relatively high temporal resolution, the obstacle was the narrow spectral probing range.

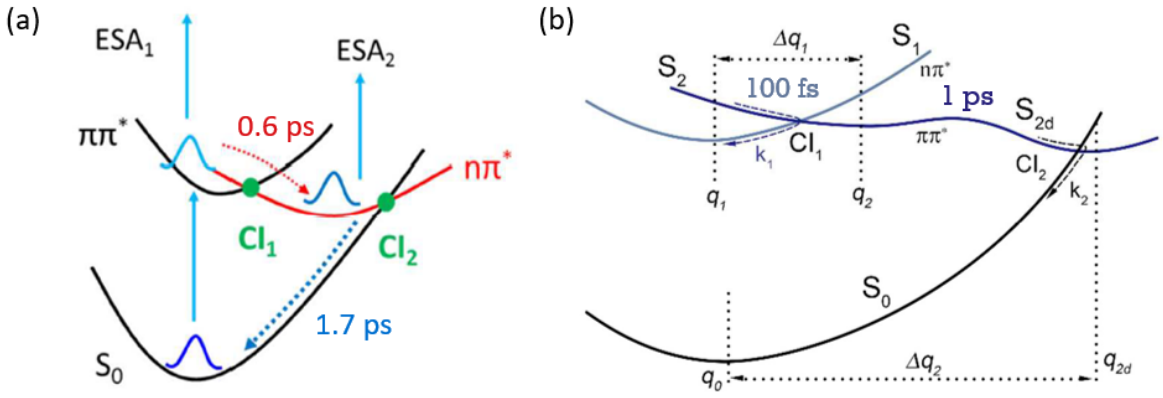

Figure 4.1: Thymine excited state decay pathways as presented in (a) Prokhonerko et al.[59] and (b) Xue et al.[66].

As we can see, either experimental or theoretical bottlenecks hampered the unambiguous explanation of the mechanisms underlying the excited state deactivation in pyrimidines. From the experimental point of view, either the resolution or the limited view of the spectral dynamics have prevented an accurate measurement able to be connected clearly with the computations. On the other hand, the theory side has been sacrificing accuracy either by neglecting the environmental effects or by the limited description of electronic correlations in their treatment. Moreover, dynamical simulations of the TA maps based on first principles that translate molecular dynamics into experimentally observable spectral features have been missing as well.

While many interpretations have been proposed over the years, the key questions remain open:

- what is the process associated with ultrafast decay in Urd and 5mUrd
- what is the reason for the observed longer lifetime of 5mUrd
- which are the effectively explored ultrafast decay pathways in Urd and 5mUrd
- are dark $n\pi^*$ states involved in the deactivation process

Here we attempt to answer them through a combination high temporal resolution UV transient absorption spectroscopy with broad spectral range of the probe pulse, and simulations based on quantum-classical dynamics within a hybrid quantum mechanics/molecular mechanics framework that take into account environmental effects done by the group of prof. Marco Garavelli from University of Bologna.[68–75].

4.2. Sample preparation

The samples for the experiments were purchased from Sigma-Aldrich. A phosphate-buffered saline (PBS) solution was prepared by dissolving 3.6 g of sodium dihydrogen phosphate and 4.26 g of sodium hydrogen phosphate in ultrapure water to obtain a concentration of 15 mM and pH of 7.4. The Urd and 5mUrd in PBS solutions were prepared to obtain concentrations of 27.6 mM and 24.2 mM, resulting in absorbance of 3 OD at the central pump wavelength in the 0.15 mm path length of the wire-guided jet configuration. The steady state absorption spectra of diluted nucleoside solutions are presented in Figure 4.2. In order to avoid photodamage and generation of solvated electrons by two-photon absorption, the pump energy was limited to 20-30 nJ (fluence of 88-132 $\mu J/cm^2$).

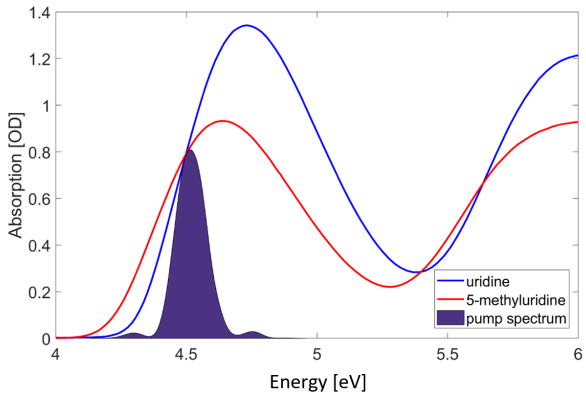

Figure 4.2: Steady state absorption spectrum of the measured molecules together with the pump pulse spectrum used for experiments.

4.3. Uridine

Figure 4.3 shows a comparison of experimental and computed TA spectra of Urd in PBS, recorded with sub-30-fs temporal resolution after excitation at 4.5 eV. Initially, we observe an intense SE band in the UV region, covering the 3-4 eV spectral range, as well as a corresponding PA1 band below 2.5 eV. The rise times of both of these signals are at the limit of the experimental resolution and also partially covered by the presence of the coherent artifact in the first 50 fs, which has been minimized by the use of low fluence and the wire-guided jet configuration.

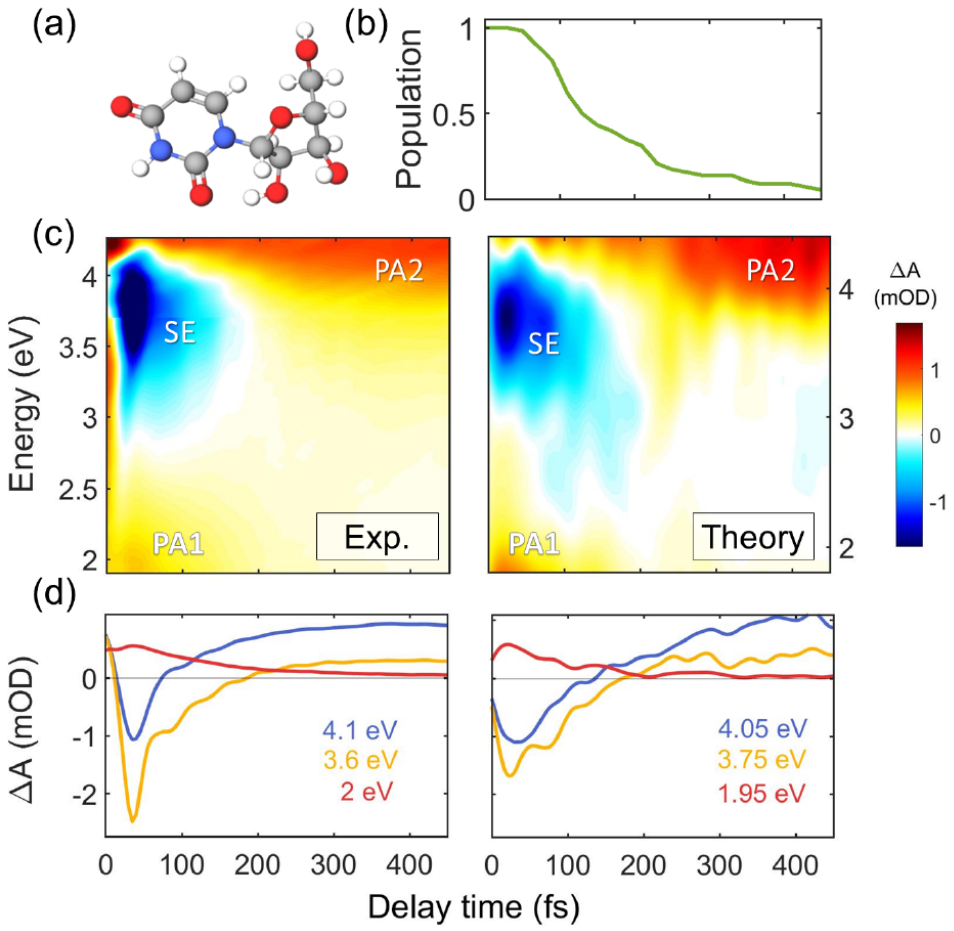

Figure 4.3: Excited state dynamics of uridine[76]. (a) Molecular structure of Urd. (b) Simulated excited state population decay. (c) Experimental and computed TA maps in parallel polarization configuration. (d) Dynamics of the above maps at selected probe energies.

Both bands observed at early times decay very quickly and disappear after 200 fs, while another PA2 band rises at deeper UV energies. From global fitting of the map we find a 97 fs time constant to be associated with the decay of SE and PA1 signals and a ∼1ps time constant for the decay of the PA2 signal (Figure 4.5). These values agree well with the results of fluorescence up-conversion and transient absorption measurements[61,65,67]. In addition to the ultrafast signals, we also find a long living minor component of the signal associated to the population of the $n\pi^*$ state shown in Figure 4.7.

The experimental result of the TA measurement is compared with the map computed based on simulations. We can see a very good agreement with the experiment. The early SE and PA1 signals are assigned to the $^1\pi\pi^*$ state. PA2 is identified as the hot ground state, as it is located nearby the edge of steady-state absorption and its build-up matches the decay of the SE. Fitting the population dynamics of the $^1\pi\pi^*$ state with an exponential, we obtain a 120 fs lifetime, which compares well both to the fit of experimental data and the simulated spectral dynamics of the PA1 band. The static computations recently identified two deactivation paths from the $^1\pi\pi^*$ state to the ground state in pyrimidine nucleosides, one involving ring-puckering with H9 out-of-plane bending and N1-C2 bond breaking[77]. Both routes could be responsible for the ballistic 100 fs decay observed experimentally that go through a CI reached over a small barrier. From simulations done by our collaborators, we could conclude that it's the ring puckering that is the dominant excited state deactivation mechanism[78]. Bond breaking is also possible but a very minor decay channel.

4.4. 5-Methyluridine

The maps of the TA experiment and simulation for 5mUrd are shown in Figure 4.4 and are qualitatively similar to Urd. After excitation, we observe a SE signal in the 3-4 eV UV region, as well as PA1 band extending below 3 eV, and another stronger PA2 band above 4 eV. The main difference are the dynamics following the initial appearance of the signals and their timescales. The SE band is rapidly shifting during the first 200 fs and significantly broadening into the 2.8-3.8 eV spectral window and together with PA1 band it lasts over 1 ps. Global analysis reveals time constants of 100 fs and 575 fs for initial period of shifting SE and the longer appearance of the broad SE signal respectively (Figure 4.5). Moreover the PA2 band exhibits a delayed build up in the first 100 fs as the SE band shifts out from underneath it, afterwards it decays in few picoseconds while blue-shifting.

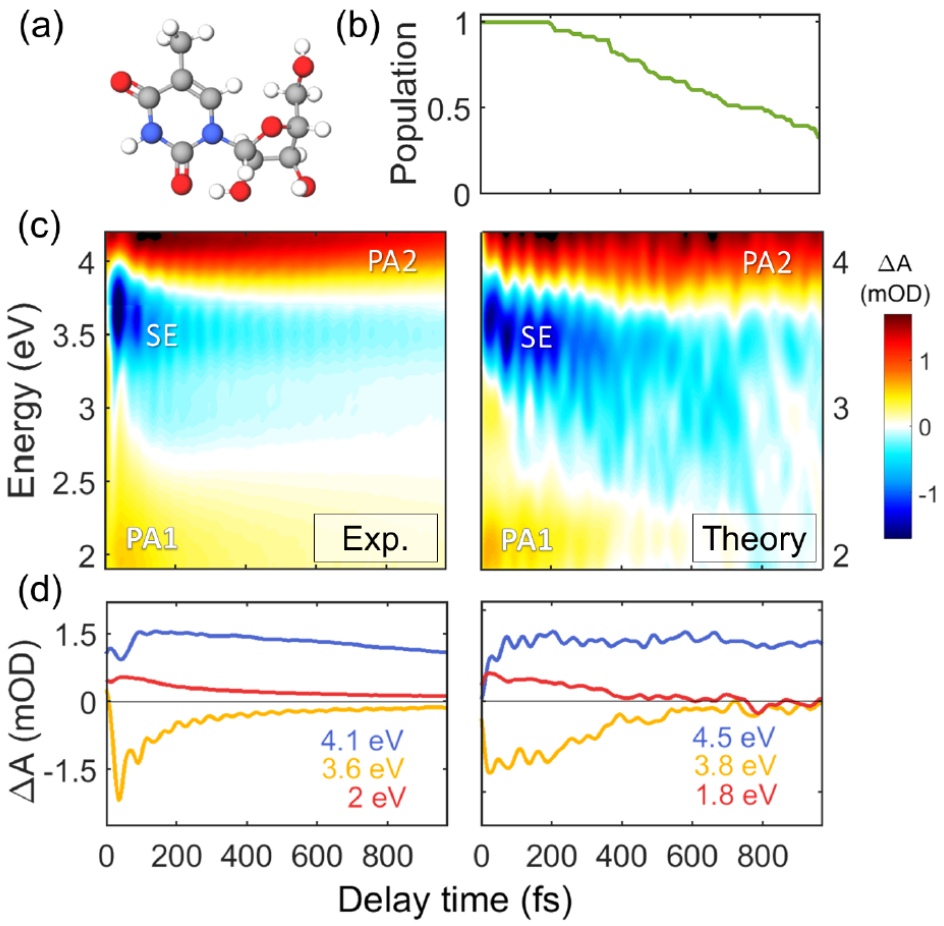

Figure 4.4: Excited state dynamics of 5-methyluridine[76]. (a) Molecular structure of 5mUrd. (b) Simulated excited state population decay. (c) Experimental and computed TA maps in parallel polarization configuration. (d) Dynamics of the above maps at selected probe energies.

The similar electronic structure of Urd and 5mUrd nucleosides is the reason for the analogous overall appearance of the two TA spectra. The simulated spectra for 5mUrd match the experiment very well and reproduce all the relevant features. We assign the initial, delayed dynamic of the PA2 signal to the tail of the intense PA band coming from the $^1\pi\pi^*$ state, which is revealed when the overlapping SE signal red-shifts out of this region. Over time this PA decays and in its place, the hot ground state PA appears and decays in a few ps. Two other PA bands are connected to the $^1\pi\pi^*$ evolution, PA1 that we observe below 2.5 eV and another one around 3 eV that is only slightly visible at the early times and later gets covered by the SE signal.

A surprising picture emerges from the non-adiabatic dynamics of the simulated spectra. We find that the $^1\pi\pi^*$ state of 5mUrd decays on a timescale of around 750 fs, which is

roughly one order of magnitude longer than the lifetime of $^1\pi\pi^*$ state in Urd. Moreover, only one hopping event is encountered within the first 200 fs. This confirms that the fast component observed in the TA spectra can't be associated with the decay to the ground state. As a result of mapping the $^1\pi\pi^*$ potential energy surface (PES)[79] implemented on all trajectories, we discover that the solvent introduces an effective dynamic barrier through which it slows down ultrafast bulky geometrical deformations. This barrier together with the inertia of the methyl group makes it impossible for 5mUrd to reach the CI region in 100 fs. In this view, it is revealed that while the solvent adapts to the electronic structure and the barrier decreases, the population is dynamically trapped in the $^1\pi\pi^*$ state on the timescale of several hundred femtoseconds. It is evident that the SE is redshifting in both experimental and theoretical spectra due to $^1\pi\pi^*$ trapping. As seen in several snapshots, the accompanying broadening of the signal is the result of out-of-plane distortion of the methyl group. For Urd however, no solvent reorganization is required due to the CI deformation only involving hydrogen atoms, which promotes the ultrafast decay on a sub-100 fs timescale.

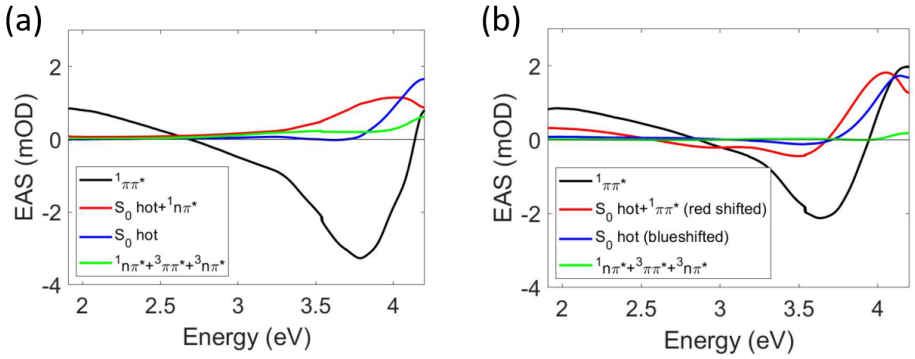

Figure 4.5: Global fits of the (a) Urd and (b) 5mUrd data represented as evolution associated spectra (EAS)[76]

4.5. Involvement of the $n\pi^*$ state

Looking for the possibility of some dark excited state, e.g. $n\pi^*$, being responsible for the fast time constant in 5mUrd, we find that even if a particular molecule in the simulation spends a picosecond in the $^1\pi\pi^*$ state, it doesn't transfer to another excited state before the CI with the GS is reached. From experiment, we only find a very low long-living signal (Figure 4.6), which could be attributed to the $n\pi^*$ and/or $3^1\pi\pi^*$ states. It is estimated that less than 5% of the population ends up in that channel.

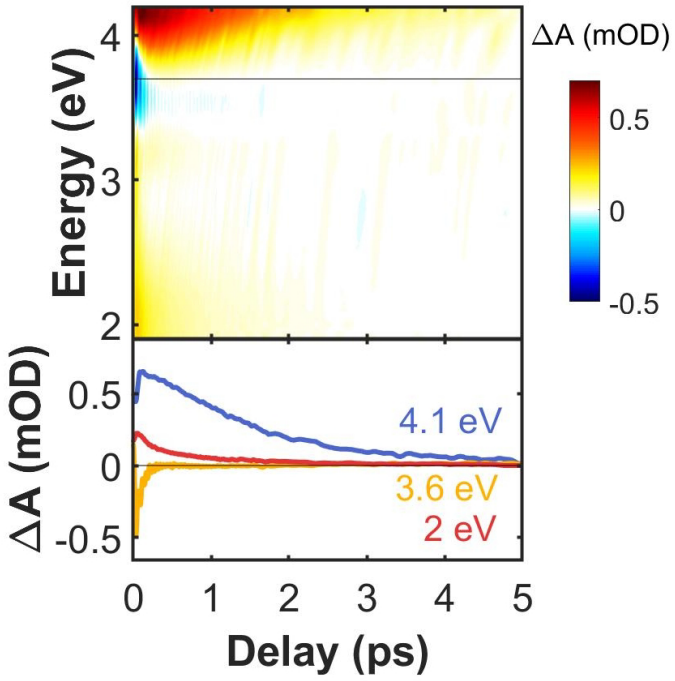

Figure 4.6: 5mUrd TA map measured with polarizations at magic angle showing very low residual signal after 5 ps[76]

On the other hand, we find that part of the Urd population (Figure 4.7) is partially transferred out of the $^1\pi\pi^*$ state into the nearest $n\pi^*$ due to wavefunction mixing in the FC region, even considering its short lifetime[80]. We estimate that up to 20% of the population can transfer to the dark $n\pi^*$ state in this manner at early times after excitation. A recent study[66] suggests a further ISC towards the triplet state manifold on the nanosecond timescale.

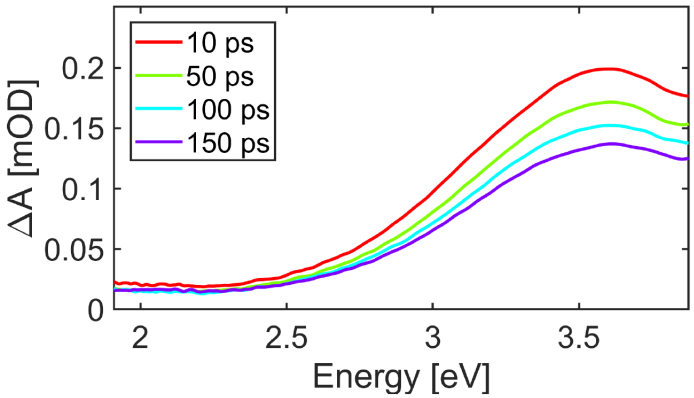

Figure 4.7: Urd transient spectra measured with polarizations at magic angle at long delays, showing significant intensity spectrum corresponding to the population of dark $n\pi^*$ state[76]

4.6. Coherent oscillations

Thanks to the very high temporal resolution of the experimental setup, we are able to observe coherent oscillations within the SE signal. This provides a unique insight into the dynamics of the excited state vibrations of the molecules. An oscillatory component of the full TA map, can be extracted by the means of a high bandpass Fourier filter. Oscillations appear immediately following the excitation in both nucleosides. In Urd only a few periods are visible and the decay lasts ∼100 fs, as the SE signal, thus it supports the idea that the oscillations are coming from the excited state vibrations. In contrast, in 5mUrd, we can clearly discern the oscillatory pattern for up to 700 fs which agrees with the long lifetime of the excited state found for this molecule.

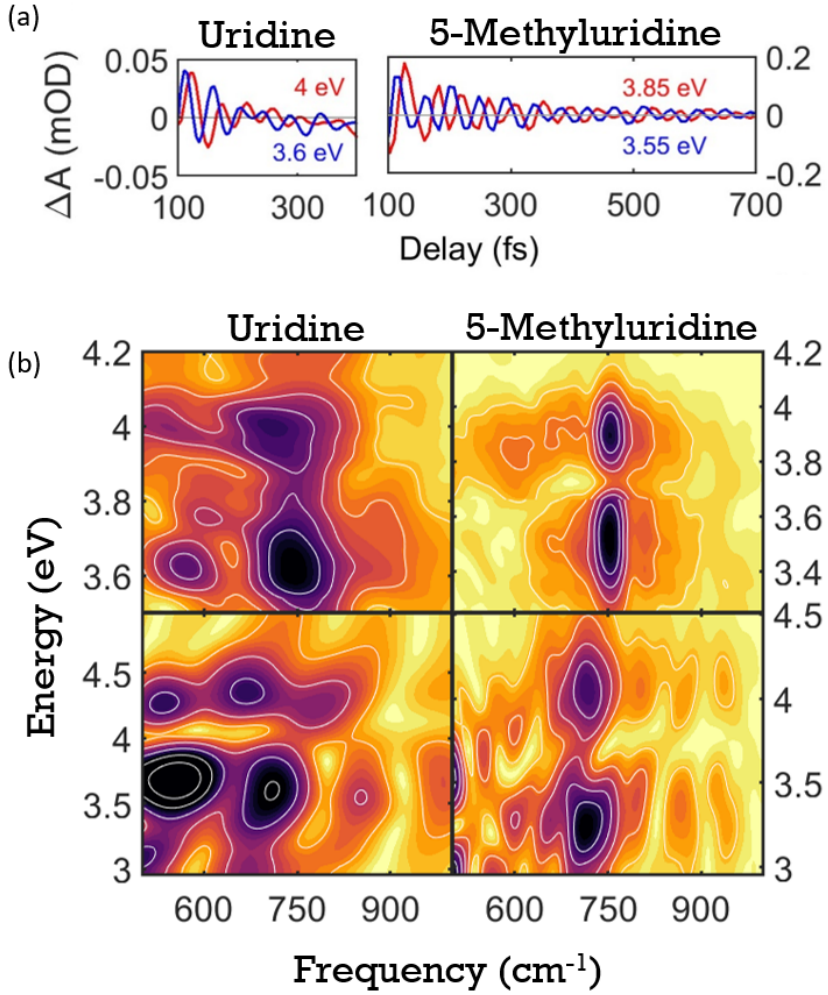

Figure 4.8: (a) Oscillations extracted from the TA map for chosen probe energies. (b) FT maps of the oscillatory residual from experiment (top) and computation (bottom) showing very good agreement.

If we look at the total 2D Fourier map (Figure 4.8), we notice a pair of peaks in the region of the SE signal, similarly reproduced by the theoretical map. For both Urd and 5mUrd, we observe a dominant mode at 750 cm^{-1} in the experimental Fourier maps. The node present around 3.9 eV, as discussed in Chapter 2, coincides with the central wavelength of emission of the SE band and is connected with a π phase shift between the peaks. These points further support the assignment of the vibrational peaks to the SE coming from the excited state[81]. The node position matches closely the vertical energy gap with the ground state at the $^1\pi\pi^*$ minimum in both nucleosides[79]. In the experimental Fourier maps for Urd, we can also distinguish a weaker pair of peaks (more clearly distinguishable in the theoretical map) at around 580 cm^{-1}. Through normal mode analysis of the excited state, we identified the 750 cm^{-1} mode as a breathing of the aromatic ring. It dominates the vibrational dynamics together with higher frequency stretching modes, which are too fast to be resolved by our setup. The 580 cm^{-1} mode found in Urd is on the other hand associated with hydrogen out-of-plane bending that accompanies the puckering so that we can assign it to the signature of the wavepacket motion towards the CI.

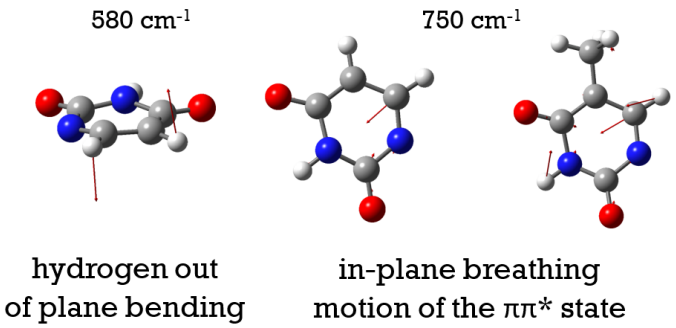

Figure 4.9: Vibrational modes observed in the experiment.

4.7. Summary

In Figure 4.10 we present a comprehensive overview of the excited state decay pathways of uridine and 5-methyluridine in an aqueous solvent, after all the above considerations. We conclude that while in both molecules we find an ultrafast ~100 fs time constant for the initial dynamics of the excited wavepacket, in Urd it is associated with a ballistic motion towards the CI and through it decays to the ground state, while for 5mUrd the fast component is ascribed to the motion away from the FC region, but the high barrier present on its way hinders the fast decay.

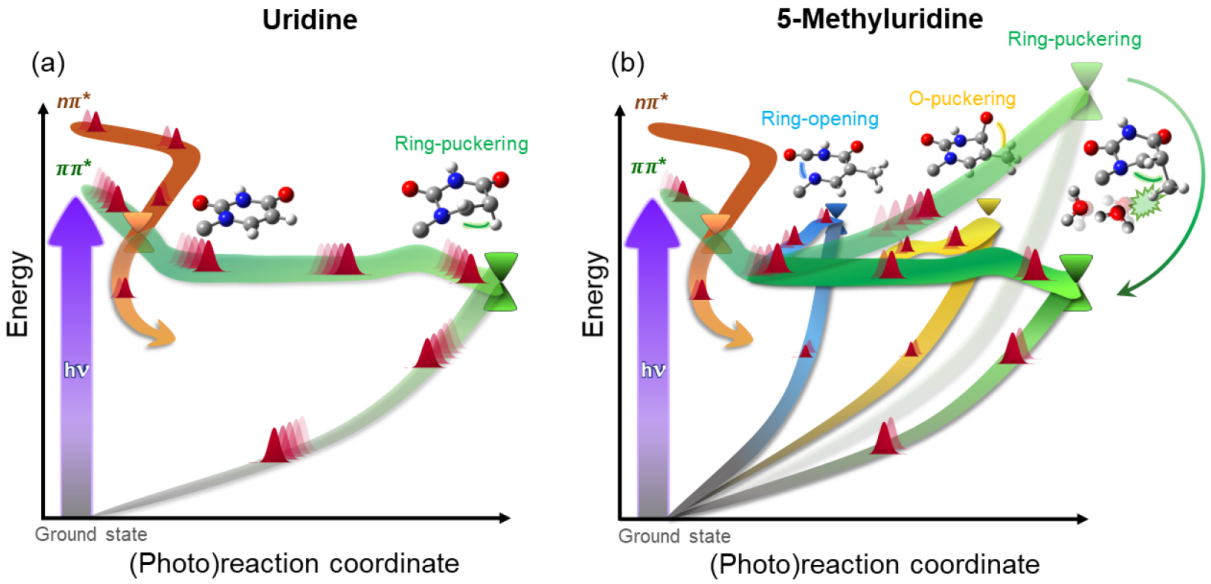

Figure 4.10: Excited state decay pathways in Urd and 5mUrd[76].

This solvent-induced dynamic barrier is associated with the bulky methyl group that is involved in ring puckering motion, and together with the higher inertia of the heavy methyl group leads to the population being trapped for a longer time in the $^1\pi\pi^*$ state. Subsequent solvent-assisted IC to the ground state happens on the longer sub-ps timescale. Moreover, while the Urd dark $n\pi^*$ state contributes significantly to the dynamics from the early times, in 5mUrd it is only a very minor decay channel. The main mechanisms driving the evolution of the system towards the CI are ring puckering due to hydrogen (Urd) or methyl group (5mUrd) out-of-plane bending. Due to the longer lifetime of 5mUrd, it also explores other minor decay routes such as ring-opening or O-puckering, which we do not observe directly in the experiment.

5 | Variety of photoprocesses in epigenetic deoxycytidine derivatives

In the previous chapter, we discussed fundamental differences in excited state behavior of uridine and 5-methyluridine, comparing how the addition of the methyl group affects the decay to the ground state, through which the nucleosides avoid photodamage. This in-depth study showed us how the decay differs between the uridine, nucleoside of RNA, and 5-methyluridine, which in its deoxyribose form becomes thymine, nucleoside of DNA. In this chapter, we focus on the special group of DNA nucleosides, which are epigenetic modifications of deoxycytidine.

5.1. Epigenetic derivatives

Multicellular organisms had to develop specialized cells to perform precise functions. All of the cells are based on the same genomic sequence information stored in the nucleus of all cells in the organism. During development this code needs to be well regulated, which involves activation and silencing of specific genes. An epigenetic information layer exists on top of the four canonical DNA nucleobases that regulates these processes. It relies on a group of cytidine derivatives made by attaching functional groups to the C5 position of the canonical base[82–85]. The main epigenetic modification is the methylation of 2'-deoxycytidne (dC) at the C5 position called 5-methyl-2'-deoxycytidine (mdC). Such change leads to transcriptional silencing of the corresponding gene and plays an important role in developmental processes. To turn the gene on again, the mdC has to be demethylated back to dC form[86,87]. This process is not yet fully understood, but additional epigenetic derivatives 5-hydroxymethyl-2'-deoxycytidine (hmdC)[88], 5-formyl-2'-deoxycytidine (fdC)[89], and 5-carboxyl-2'-deoxycytidine (cadC)[90] have been discovered to take part in the process (Figure 5.1). It has been shown that through consecutive oxidation reactions catalyzed by 10-11 translocation enzymes, these modified cytidines

are formed from mdC[90–93]. The oxidized derivatives of mdC are nowadays thought to not only form steps of the demethylation process, but also that they may take an active role in regulation of concentration and patterns of epigenetic markers. The presence of modifications in the epigenetic derivatives of dC, will affect the efficient deactivation channels of the canonical cytidine, where the absorbed UV light energy is safely dissipated away. This can induce more complex decay pathways that could lead to higher probabilities of photodamage, or even improve the photoprotection efficiency[13,14,94–96].

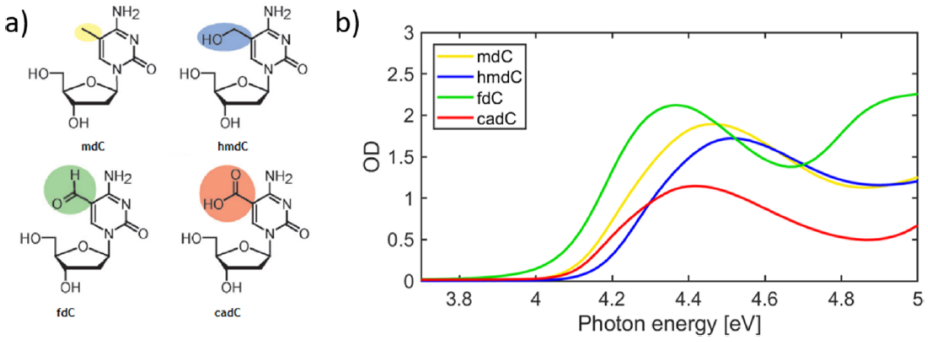

Figure 5.1: (a) Molecular structures of the epigenetic derivatives and (b) their linear absorption spectra[97]. The cadC nucleoside has been simulated in the anionic form as it is the stable species at neutral pH.

It has been documented that even though the thymine-thymine dimer is commonly formed due to the longer thymine excited state lifetime, it is rather poorly mutagenic and in most cases, it is read out correctly and repaired to its original state. In contrast, the available evidence clearly indicates that mdC plays a major role in mutagenesis in mammals[98]. In addition, the data shows that the T=T dimer, is in fact not the most efficiently produced dipyrimidine lesion caused by exposure of DNA to sunlight. It has been found that the CPD formation is enhanced up to 10-fold at 5'-CCG and 5'-TCG sequences due to the presence of mdC bases[99]. The increased chance of mutations caused by the CPD formation at the methylated cytosine sites is also the effect of significantly higher probability for spontaneous deamination in this form[100,101]. As shown in Figure 5.2, when the energetic UV photons bind the neighboring thymine and methylcytosine into a dimer, deamination, either direct or through a tetrahedral intermediate can turn the C into T. If the repair of the dimer while still in the T=^{m}C form is not fast enough, the replication mechanisms finding the T=T dimer at this position, even if read correctly, will copy forward the damaged sequence, with T substituted instead of C.

According to the literature, mdC shows an energy barrier ∼0.1 eV higher than its classical nucleoside dC, along the same decay pathway that drives the molecule from the ES to

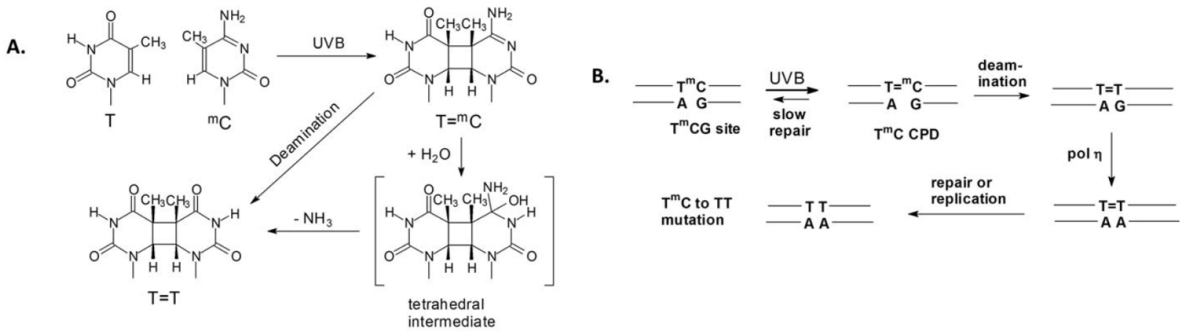

Figure 5.2: (a) Formation of a CPD at a T^{m}C site and its deamination. (b) Deamination bypass pathway leading to the formation of UV-induced C to T mutation at T^{m}C sites in which polymerase η inserts an A opposite the T resulting from deamination of the mdC in the CPD formed by UV light[100].

the "ethylene-like" CI with the GS[7,9,67,102]. This increase in the barrier height, explains the longer lifetime of the ES found in the derivative (6.8 ps) with respect to the parent molecule (1.1 ps), found in TA spectroscopy experiments[103,104]. Clearly, this significant decay elongation explains why the mdC is more susceptible to photodamage. Recently, experimental and theoretical studies have shown first results on the behavior of photoexcited hmdC, fdC, and cadC, presenting their different dynamics[105–107]. While the lack of high enough temporal resolution, prevented the correct description of the fastest dynamics in those molecules, they found experimental evidence of the existence of efficient ultrafast intersystem crossing (ISC) that populates the long-living triplet state in fdC. The correct mapping of photophysical processes underlying the excitation of epigenetic cytidines is of increasing interest, becoming a current matter of debate, and giving rise to contradictory hypotheses on the decay mechanisms.

Here we provide a unified description of the complex decay pathways of epigenetic derivatives through a combination of experimental data and theoretical support from the group of prof. Marco Garavelli from University of Bologna. The state-of-the-art sub-30-fs temporal resolution of the setup discussed in Chapter 3 helped us in following the rapid evolution of the photoexcited wavepackets in a broad spectral window, in contrast to previous works[104,105]. By comparison with static calculations using a hybrid SS-CASPT2/MM scheme with explicit water solvent, we could then unravel the major decay routes based on the minimum energy paths and find the main CIs driving the different photoprocesses[24,72,73,108]. Thanks to the high sensitivity of the experimental approach, we avoided the formation of solvated electrons by using low fluences, which helped with disentangling the TA signals and their correct assignment.

5.2. Sample preparation

The samples have been prepared by the collaborators from the LightDyNAmics consortium in the group of prof. Thomas Carell from Ludwig-Maximillien Universitat. All reactions (unless done in aqueous solutions) were done in flame-dried glassware and under argon atmosphere. 5-Methyl-2'deoxycytdine has been purchased from Sigma Aldrich, chemical ingredients for the other molecules were purchased from Sigma-Aldrich, TCI, Carbolution and Carbosynth, and the nucleosides were synthesized, purified, and identified according to literature. A PBS solution has been prepared by dissolving 26.7 g of sodium dihydrogen phosphate and 20 g of sodium hydrogen phosphate in 1 L of ultrapure water to obtain a concentration of 150 mM and a pH of 7.1 after adjusting with sodium hydroxide. The sample solutions were prepared to achieve high concentrations to achieve a thin effective sample path as due to the low available amount of the samples, they had to be measured in 1 mm cuvette, as described in Chapter 3.2. We prepared them with 2 OD in 100 um path, by mixing 5.1 mg of mdC in 1 ml, 5.8 mg of hmdC in 1 ml, 4.8 mg of fdC in 1 ml, and with 1.2 OD in 100 um path by mixing 5.4 mg of cadC in 1 ml. To record the linear absorption spectra, the samples have been diluted 10-fold to avoid saturation of the spectrophotometer in the 1 mm path of the cuvette. Figure 5.1 shows the chemical structures together with the steady-state absorption of all the measured nucleosides, obtained by substitution at the C5 position of the original cytosine nucleobase. The spectra are dominated by a band spanning 4.1 – 4.6 eV due to the $^1\pi\pi^*$ transition of the aromatic ring.

5.3. 5-Methyl-2'-deoxycytidine

Starting with mdC, Figure 5.3 shows a differential absorption transient spectrum map of the first picosecond after excitation at 4.35 eV, which populated the lowest bright $^1\pi\pi^*$ ES. Immediately, we observe a SE band peaking at 3.68 eV together with a PA band extending below 3.3 eV. The two bands experience a rapid partial decay in 130 fs, while the SE signal is clearly red-shifting to 3.54 eV. This first spectrum observed after excitation is also presented in Figure 5.3c (blue line), an evolution associated spectrum (EAS) acquired from global analysis of the TA measurement. Afterwards, the spectrum continuous the decay and the emission shift, in 1 ps changing from the purple spectrum into the pink one, followed by a 4.3 ps decay into a residual long living spectrum without any SE signatures.

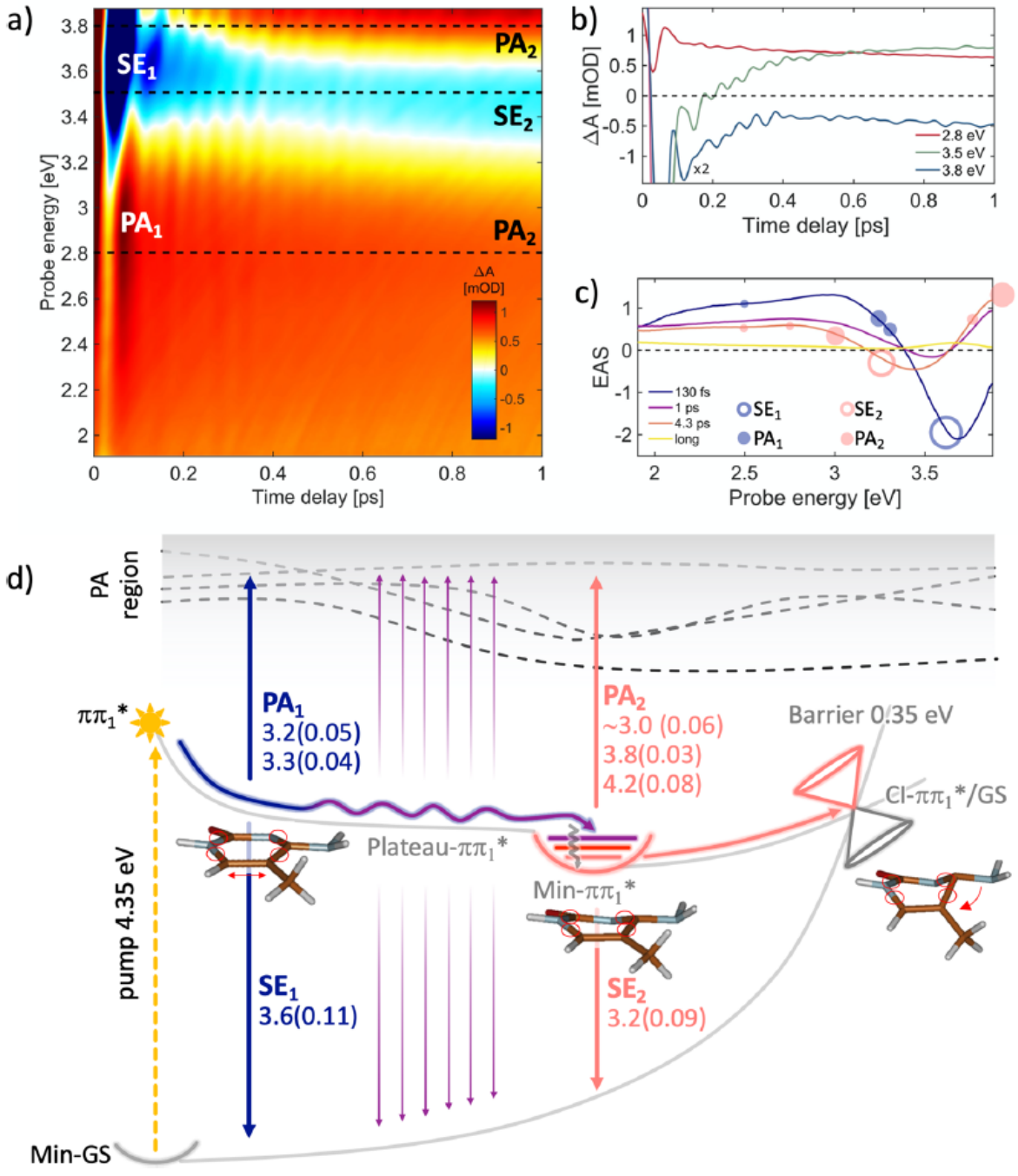

Figure 5.3: (a) TA map of mdC measured with polarizations at magic angle. (b) Dynamics at selected probe energies marked with dashed lines in panel a. (c) EAS with circles corresponding to the calculated SE and PA energies. Circle size is proportional to the oscillator strength. (d) Schematic mdC decay pathways color-coded to match the EAS in panel c. Calculated transition energies are given together with oscillator strength in brackets[97].

Experimental TA results are in line with ES decay paths predicted from QM/MM computations. The complete view of the early dynamics based on putting them together is presented in Figure 5.3d. Ultrafast relaxation from the FC region of the $^1\pi\pi^*$ (S1) state on the way to a flat region of the ES PES, set apart by low forces affecting the system (Plateau-$^1\pi\pi^*$, Figure 5.3d) is revealed. The calculated SE band at 3.6 eV with an oscillator strength (OS) of 0.11, matches the experimental SE band observed directly after excitation (empty blue circle in Figure 5.3c). Computations also replicate the bands of the PA spectrum (full blue circles in Figure 5.3c) detected over the whole visible region at early times (PA1) just after the molecule leaves the FC region and reaches the plateau (vertical blue arrows in Figure 5.3d). We assign the observed drop of intensity and red-shift of the SE band during the first 130 fs (change from blue to purple EAS) to the system moving across the flat Plateau-$^1\pi\pi^*$ region, before settling down in the minimum (Min-$^1\pi\pi^*$) within 1 ps. Due to the barrier that needs to be overcome to pass through the CI to the GS, the system resides here for a longer time of 4.3 ps (pink spectrum in Figure 5.3c). The computed SE2 from the Min-$^1\pi\pi^*$ point is red-shifted with respect to SE1 and located at 3.2 eV (OS 0.09). The reduction of the intensity and the blue-shift of the experimental SE peak compared to the calculated value (SE2, pink empty circle in Figure 5.3c) could be explained by the overlap of the SE2 with the tail of the PA2 band, expected at 3 eV from Min-$^1\pi\pi^*$ (OS 0.06). Additionally two other PA signals have been found from computations starting from the ES minimum, at 3.83 eV and 4.22 eV that match well with the experimental TA measured in that part of the spectrum. The 4.3 ps decay of the SE2 and PA2 signals coming from the $^1\pi\pi^*$ minimum is consistent with the presence of the 0.35 eV energy barrier leading to the lowest-lying CI between the ES and the GS. After the system traverses the main decay route of IC to S_0, a weak PA spectrum (yellow line in Figure 5.3c) is left, which doesn't decay within the experimental time window (30 ps), and represents other minor decay pathways, possibly being a signature of dark $n\pi^*$ states population.

The structural changes related to the ES evolution and IC processes are illustrated in Figure 5.3d. While the optimized $^1\pi\pi^*$/GS CI is not exactly the same as the "ethene-like" CI found previously by Martinez-Fernandez et al.[103], they both show similar energy barriers (0.35 and 0.3 eV respectively). The CI structure reported here is more easily accessible as it happens exactly along the reaction coordinate that connects the planar structure to the crossing while passing through the Min-$^1\pi\pi^*$. In the experimental TA maps, we also find signatures of vibrational motions recorded as oscillatory patterns modulating the SE signal (Figure 5.4). These oscillations are covering a broad region between 2.8 eV and 3.9 eV suggesting that the emission width observed is significantly artificially narrowed

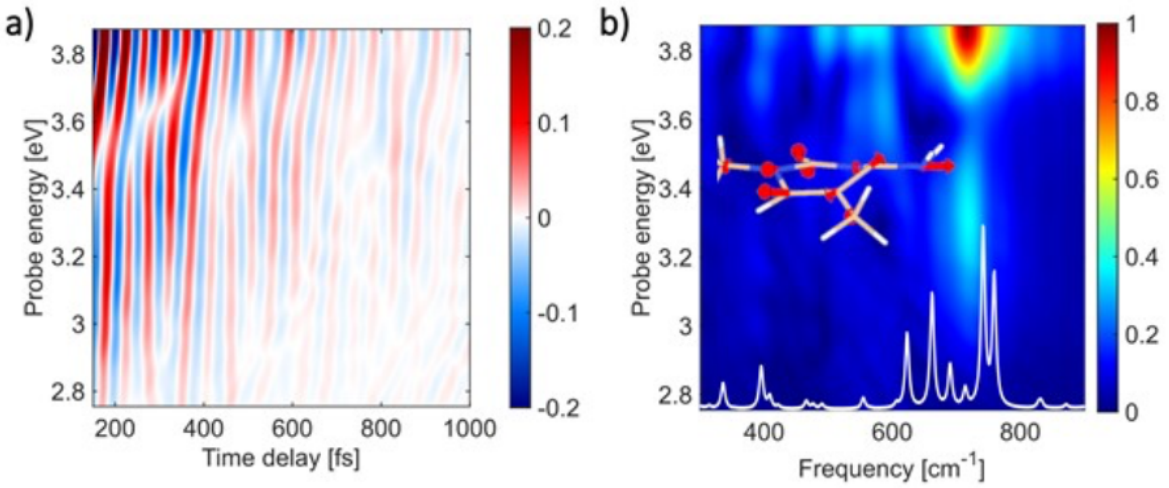

Figure 5.4: Oscillating residual of the TA map for mdC (a) and its FT map (b) with normal modes of the $^1\pi\pi^*$ minimum overlapped in white. Inset shows the ring distortion mode corresponding to the dominant 715 cm^{-1} mode[97].

through the presence of nearby PA bands. Looking at the FT map of the oscillations in the UV region, and their comparison, we can find a strong peak with a characteristic node at 3.6 eV in the amplitude at 715 cm^{-1}, which corresponds to the most intense calculated mode in this range at 740 cm^{-1} corresponding to the $^1\pi\pi^*$ ring distortion shown as inset in Figure 5.4.

5.4. 5-Hydroxymethyl-2'-deoxycytidine

Photophysics of hmdC are very similar to the ones observed in mdC upon UV photoexcitation at 4.35 eV. In both cases, the TA spectra and the computed energies closely resemble those of mdC (Figure 5.5). After the pump brings the population into the S_1 state ($^1\pi\pi^*$), it moves towards the Plateau-$^1\pi\pi^*$ region in 160 fs, and then rests in the minimum after 735 fs, showing red-shifting behavior of the SE band as in the previous case. These dynamics are explained the same way as in the mdC case. Initial planar relaxation leads to a ring-puckering mode that later has to pass through a similar size barrier (0.3 eV) to arrive at the CI of $^1\pi\pi^*$ with the GS, which this time takes 4.6 ps. The close photophysical behavior can be noticed by comparison of the two TA maps, noting that the visual difference of the observed total signals, is caused by relatively higher intensity of the PA bands in contrast to the SE bands in the case of hmdC, thus hiding the SE evolution behind the stronger absorption.

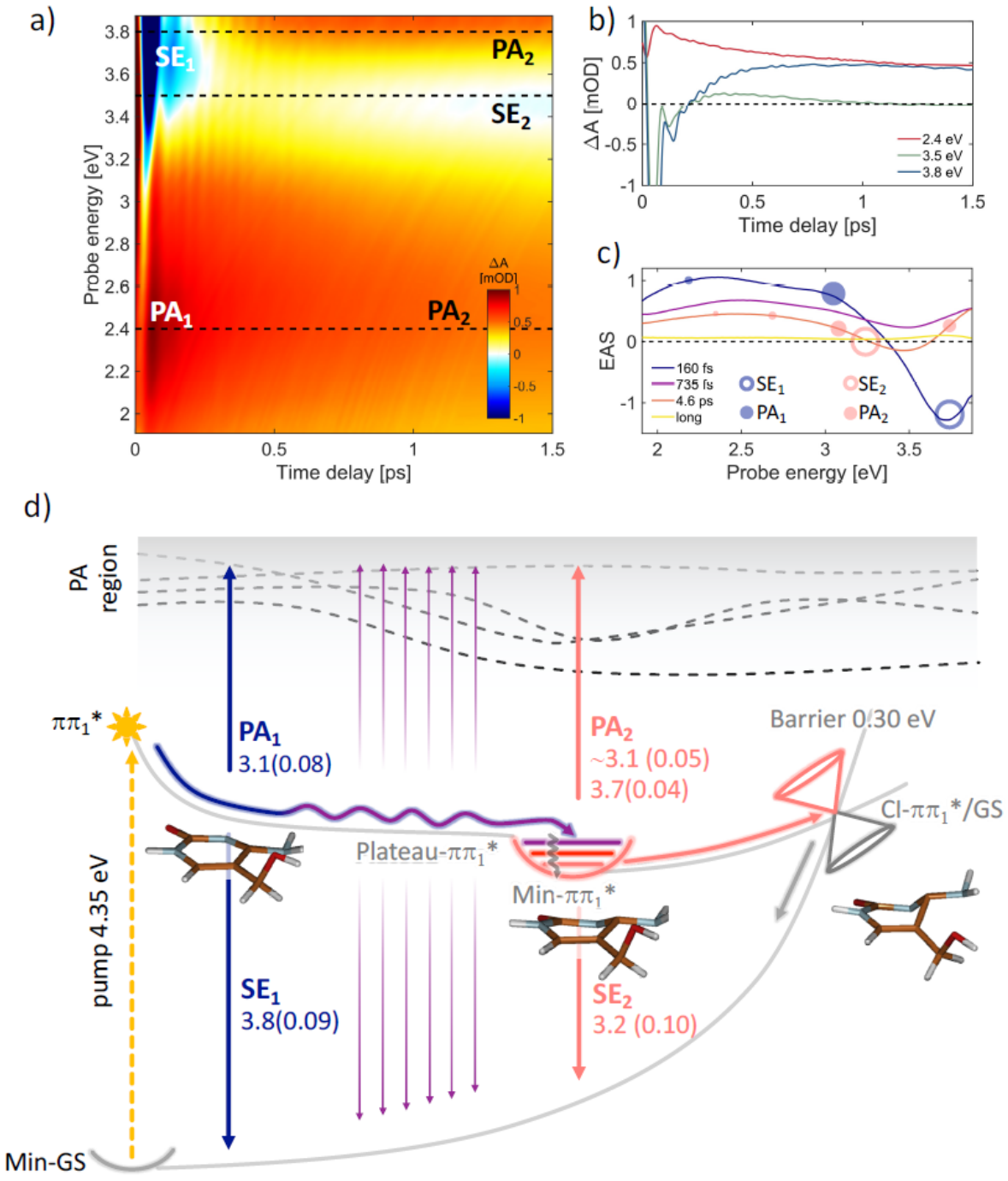

Figure 5.5: (a) TA map of hmdC measured with polarizations at magic angle. (b) Dynamics at selected probe energies marked with dashed lines in panel a. (c) EAS with circles corresponding to the calculated SE and PA energies. Circle size is proportional to the oscillator strength. (d) Schematic hmdC decay pathways color-coded to match the EAS in panel c. Calculated transition energies are given together with oscillator strength in brackets[97].

Also similarly to mdC, we find oscillations covering the SE band and corresponding again to a 715 cm^{-1} mode with a node at 3.6 eV, representing the average central photon energy of the emitting state (Figure 5.6).

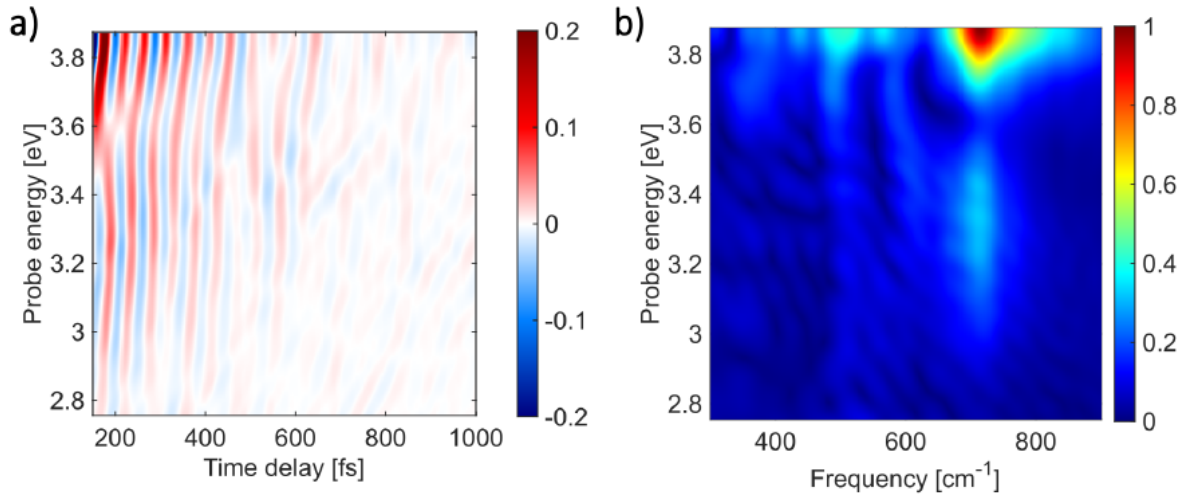

Figure 5.6: Oscillating residual of the TA map for hmdC (a) and its FT map (b). Similarly as in the case of mdC, the dominant mode is present at 715 cm^{-1}[97].

5.5. 5-Formyl-2'-deoxycytidine

Cytidine derivative with the formyl group shows a much different decay scenario compared to the other epigenetic nucleosides (Figure 5.7). This is caused by the presence of two almost isoenergetic excited states in the FC region, bright S_1 ($^1\pi\pi^*$) and dark S_2 ($n\pi^*$) (yellow star and circle respectively in Figure 5.7). The degeneracy of the states leads to branching of the population upon pumping at 4.35 eV. The $^1\pi\pi^*$ state (right part of Figure 5.7d) is showing spectral features that compare well with the experiment, where we observe the SE and PA1 bands, better distinguishable on the EAS plot (Figure 5.7c) as the blue curve. In parallel, the $n\pi^*$ dark state is partially populated, contributing its signatures of PA2 bands in the 3.3 and 3.9 eV regions (see Min-$n\pi^*$ PA2 in Figure 5.7d). Considering the bright state pathway, an ultrafast relaxation process leads to the Plateau $^1\pi\pi^*$, a planar region of the $^1\pi\pi^*$ state that spans a progressively shrinking S_1-S_0 energy gap from 3.3 to 1 eV (due to the increase in the energy of the GS). At this point, the structure experiences strong distortions along the "ethene-like" coordinate: starting from planar geometry, a large torsion around the C2N1-C6C5 angle (until 54 deg), and a C5 formyl-out-of-plane-bending (until 100 deg) take place (as presented in Figure 5.7d). Following the optimization along S1, we find a low-lying $^1\pi\pi^*$/GS CI, that lacks any energy barrier from the plateau region, suggesting ultrafast decay dynamics.

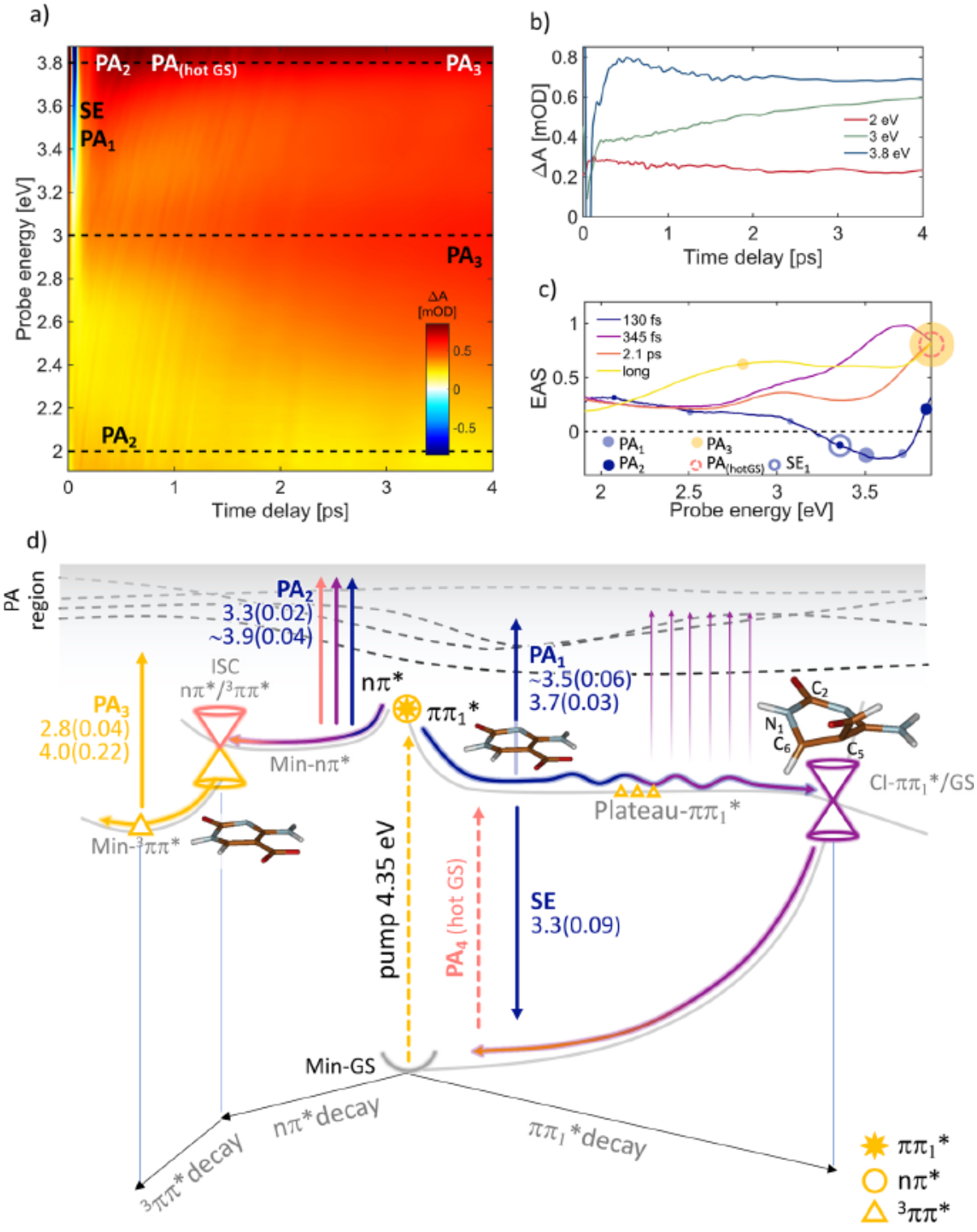

Figure 5.7: (a) TA map of fdC measured with polarizations at magic angle. (b) Dynamics at selected probe energies marked with dashed lines in panel a. (c) EAS with circles corresponding to the calculated SE and PA energies. Circle size is proportional to the oscillator strength. (d) Schematic fdC decay pathways color-coded to match the EAS in panel c. Calculated transition energies are given together with oscillator strength in brackets[97].

As can be seen in Figure 5.7c, the corresponding SE signal disappears in 130 fs, corresponding to a later stage of the Plateau-$^1\pi\pi^*$ region evolution. Then the $^1\pi\pi^*$-GS energy gap is reduced, until the decay of the wavepacket to the GS in 345 fs. The TA spectrum also contains contributions from the hot ground state absorption, after the decay of $^1\pi\pi^*$ population through CI. Hot GS relaxation usually lasts picoseconds and here we observe its decay together with the ISC process.

On the other hand, the previously mentioned dark state is almost degenerate with the $^1\pi\pi^*$ bright state at the FC point, and the crossing between the surfaces of these two states leads to population of the $n\pi^*$ singlet state through IC process at early times after excitation. Tracking the dark $n\pi^*$ state, the optimization leads to a Min-$n\pi^*$, where the calculated PA2 values contribute to the first three time constants, as the decay of the $n\pi^*$ state into the triplet via ISC process would require picosecond timescales, as supported by recent time-resolved mid-IR spectroscopy measurements[107].

An important feature of the $n\pi^*$ decay path is that at the Min-$n\pi^*$, the lowest $^3\pi\pi^*$ triplet excited state is in vicinity to the singlet $n\pi^*$, facilitating efficient ISC that populates the T1 triplet excited state minimum (yellow triangle in Figure 5.7d). The decay of the $n\pi^*$ spectrum in 2.1 ps (pink line in Figure 5.7c) into the remaining long-lived absorption spectrum (yellow line in Figure 5.7c) is assigned to the population of this lowest triplet state, that stays constant within our probing window[105]. In support of this mechanism, the calculated PA3 values coming from the triplet minimum (2.8 and 4 eV) show good agreement with the experimental peak around 2.84 eV (yellow line Figure 5.7c), as well as with the more intense UV signal, better recognizable in the DUV probe spectrum in Figure 5.8, which displays a higher OS of 0.22, this way explaining the strong absorption tail on the blue edge of the main TA map. The high quantum yield of the triplet state[105,109], can also be ascribed to a minor pathway coming from the Plateau-$^1\pi\pi^*$ region, in which the triplet is isoenergetic with the bright state (yellow triangles on the right of the Figure 5.7d).

The combination of high-resolution TA spectroscopic measurements with state-of-the-art CASPT2/MM computations enables us to derive this detailed picture of the different photoinduced decay pathways in fdC, connect the observed time constants, and understand the routes leading to population of the triplet.

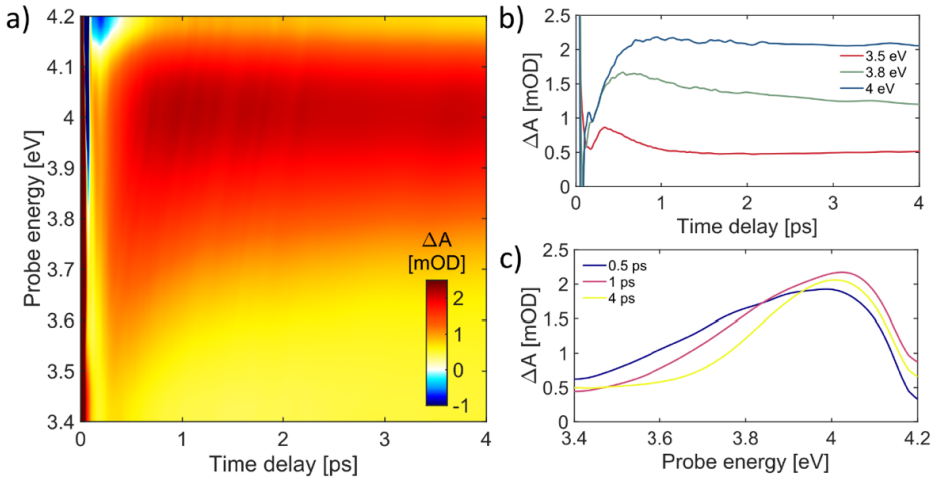

Figure 5.8: TA map (a) of fdC measured with the DUV probe together with dynamics at selected energies (b) and spectra at selected delays (c)[97].

The $^1\pi\pi^*/n\pi^*$ IC in the FC region, leading later to the ISC and the ultrafast barrierless $^1\pi\pi^* \rightarrow S_0$ decay are both previously unpredicted in fdC deactivation processes[105–107]. We also note here the remarkable similarity of the initially observed spectra for all the discussed molecules and their time constants, showing that the different substitutions are not removing the original path towards the CI with the GS.

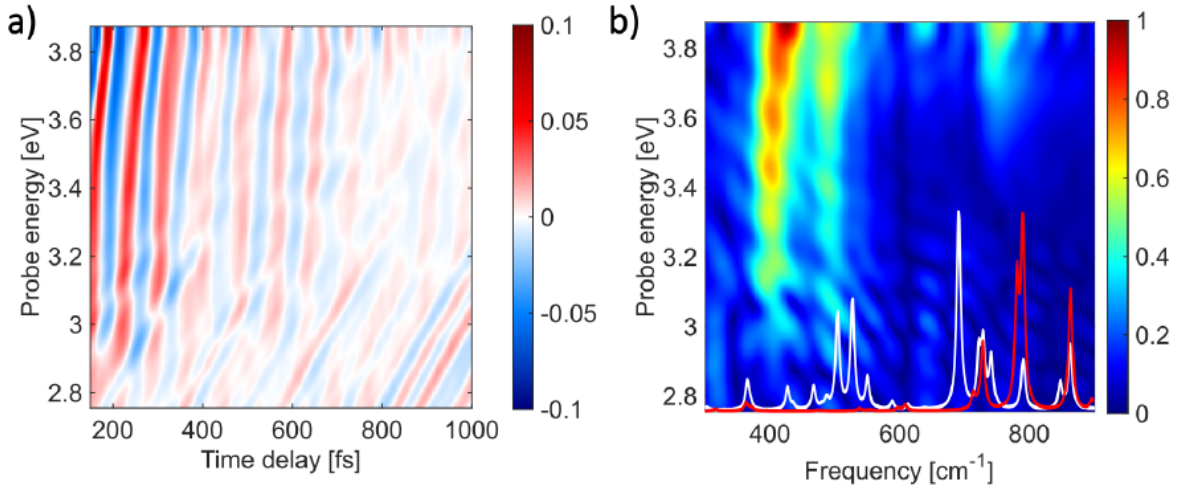

Figure 5.9: Oscillating residual of the TA map for fdC (a) and its FT map (b) with normal modes of the $^1\pi\pi^*$ plateau overlapped in red, matching the experimental mode at 750 cm^{-1} and normal modes of the $n\pi^*$ minimum in white, matching the experimental modes at 410, 490 and 640 cm^{-1}. Inset shows the ring distortion mode corresponding to the dominant 715 cm^{-1} mode[97].

In fdC, similarly to the previous two molecules we also find vibrational signatures in the UV part of the spectrum. In this case, we don't locate a node in the observed range, and the source of the oscillations cannot be clearly assigned, but we observe dominant modes at 410 cm^{-1}, 490 cm^{-1}, and 750 cm^{-1}. The computations locate the most intense modes at 791 cm^{-1}, corresponding to the ring distortion normal mode characteristic of $^1\pi\pi^*$ relaxation (red spectrum imposed on the FT map in Figure 5.9), and modes coming from the $n\pi^*$ minimum addressable to the 503 cm^{-1}, 526 cm^{-1} and 691 cm^{-1}, that we compare with the experimentally observed frequencies.

5.6. 5-Carboxyl-2'-deoxycytidine

Finally, we consider the photophysical behavior of cadC upon 4.35 eV excitation.

The experiment shows ultrafast decay of most of the initially observed intensity and no strong evidence for triplet formation is found. The experimental TA map (Figure 5.10) just after excitation is dominated by strong SE and PA signals at 3.68 and 2.33 eV respectively, rapidly shifting and decaying in 130 fs and giving rise to a hot ground state PA band in the UV together with small residual intensity in the shifted PA tail in the near IR region, which then decays on the picosecond timescale together with the stronger PA tail coming from the blue side of the spectrum. The EAS decays first with 130 fs time constant, while most of the population is leaving the $^1\pi\pi^*$ state through a CI and giving rise to the characteristic spectrum of hot ground state population that subsequently decays in 960 fs. Optimizing the lowest $^1\pi\pi^*$ state, we again find a flat region of the PES (Plateau-$^1\pi\pi^*$) where the SE signal at 3.7 eV (Figure 5.10c, blue open circle) matches the short-living experimental signal, leading in a ballistic fashion straight to the CI with the GS. This is much different behavior compared to mdC and hmdC nucleosides, where the flat region of the PES lead first to the Min-$^1\pi\pi^*$ and the energy barrier trapped the population for much longer times.

We attribute the red tail of the purple EAS spectrum to the minor residual population remaining trapped for longer times on the Plateau-$^1\pi\pi^*$ (similarly as in fdC), where the SE is almost negligible, showing only a very weak band around 2.9 eV. A significant part of the $^1\pi\pi^*$ population decays in a ballistic manner through the CI, but there is also corresponding low intensity PA signal living for much longer times, extending after the 30 ps experimental time window that comes from some minor decay pathway like possible $n\pi^*$ or triplet states. For the case of cadC derivative, we couldn't observe clear oscillations in the spectra, due to noise, sample degradation, and fast decay of the excited state.

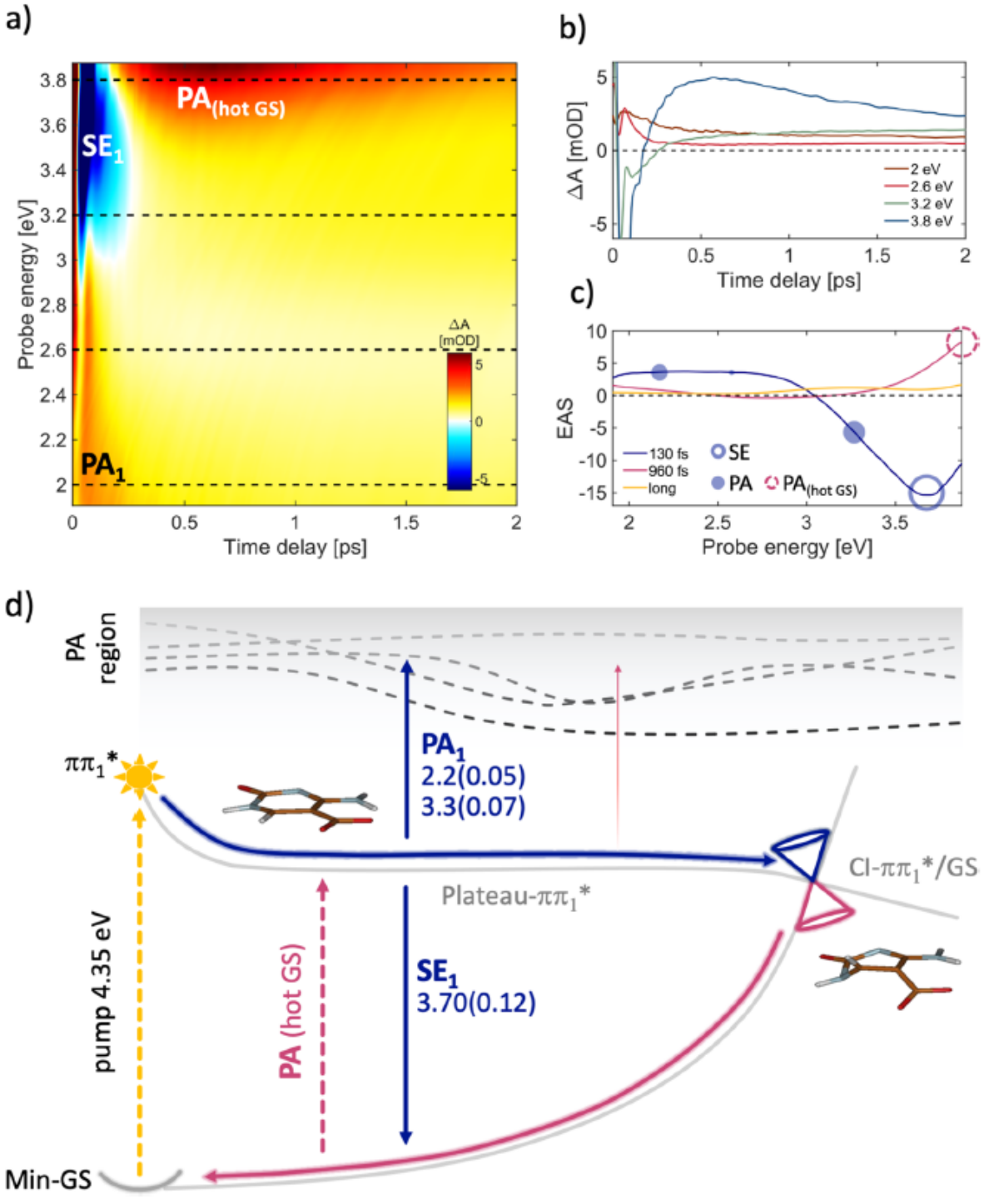

Figure 5.10: (a) TA map of cadC measured with parallel polarizations. (b) Dynamics at selected probe energies marked with dashed lines in panel a. (c) EAS with circles corresponding to the calculated SE and PA energies. Circle size is proportional to the oscillator strength. (d) Schematic cadC decay pathways color-coded to match the EAS in panel c. Calculated transition energies are given together with oscillator strength in brackets[97].

5.7. Summary

To conclude, this combined experimental and theoretical investigation provides a detailed picture of the ES dynamics of all four epigenetic 2'-deoxyctydine nucleosides. Blending ultrafast TA spectroscopy with a high temporal resolution with high-level CASPT2/MM computations with explicitly included solvent, we have shown how the different chemical substitutions dramatically affect the decay pathways. Replacing the hydrogen atom at the C5 position of the pyrimidine ring with methyl or hydroxymethyl group slows down the ultrafast decay path compared to unaltered cytidine due to an increased energy barrier to reach the CI (0.35 and 0.3 eV respectively compared to 0.18 eV in cytidine)[103]. The SE signal recorded in the TA map provides a spectroscopic fingerprint of the $^1\pi\pi^*$ state decaying in ∼4 ps in contrast with the typical subpicosecond decay of 2'-deoxycytidine. Substitution of C5 hydrogen with formyl group in fdC significantly affects the excited state dynamics. We identify a strongly populated $n\pi^*$ state that enables an ultrafast 2 ps ISC process that gives rise to a long-lived triplet state recognized in previous studies[105]. In the carboxyl derivative, we found the shortest ES lifetime among all the epigenetic cytidine nucleosides, where most of the population decays due to ballistic motion into the barrierless CI. This work constitutes a major step toward complete understanding of the intricate photophysical decay dynamics of epigenetic dC derivatives in the biologically relevant aqueous environment. Our results may help to illuminate the role of epigenetic nucleosides in the incidence of DNA photodamage, enhanced by either long lived singlet states or population of triplet states, possibly leading to generation of destructive singlet oxygen or perhaps suitable in medical applications as phototherapeutic agents.

6 | Environment sensitive ultrafast photophysics of tryptophan

The photophysics of Tryptophan (Trp) are being actively investigated due to its crucial importance for basic research as well as possible applications as a local probe for structural dynamics of proteins[25–27,30,31,110–115]. Even though there were many experimental and theoretical studies conducted on the photoinduced dynamics of Trp triggered by UV light, the earliest stages of its evolution evaded detailed explanations. Trp radicals play an important role in mediating biological electron transfer, e.g. Trp-48 in the hydrophobic core of azurin, the protein responsible for electron transfer between enzymes in the cytochrome chain of bacteria[32]. The local environments of Trp-48 in azurin as well as in many other proteins have been shown to be significantly affecting its spectral response[29–31]. Moreover, it has been shown theoretically that the aromatic side chains in small peptides can be used as local highly specific markers for tracking dynamics and structural rearrangements of proteins, through the application of 2D UV spectroscopy[28].

The tryptophan molecule exhibits the two lowest close-lying bright $^1\pi\pi^*$ excited states, Lb and La, with overlapping absorption bands. The La state lies vertically above Lb in the FC region, but it is also known from the literature that this is the main fluorescent state of Trp in polar solvent[116,117]. As a result, the observed ultrafast spectral dynamics have been assigned to the Lb→La IC process, the timescales of which have been debated[118–124]. Generally, hundreds of fs and ps time constants have been proposed, but without combination with detailed theoretical computations, the analysis lacked arguments for firm explanations.

The theoretical work done on the chromophore of Trp, Indole, can also help with explaining UV photophysics[125–131]. For example, Giussani et al. demonstrated that in the gas phase the Lb state is more stable than La[125]. Two CIs have been reported between Lb and La, suggesting a potential La→Lb transfer immediately after photoexcitation, but it has not been confirmed in experiments. The presence of strong vibronic coupling that is required for efficient IC was demonstrated by Brand et al.[126,127]. Based on time-dependent

density-functional theory dynamics in the solvent, Wohlgemuth et al.[132] obtained 45 fs for the time constant of the La→Lb IC (with minor repopulation of GS through a $\pi\sigma^*$[133,134]), and a similar timescale has been suggested in fluorescence anisotropy experiments[123].

All of the previous literature was hinting at the idea that there exist back-and-forth population exchanges between the La and Lb levels on ultrafast timescales, but suggested contrasting explanations. In this chapter, we show how a combination of high-resolution TA spectroscopy and CASPT2 theoretical calculations directly including solvent into quantum mechanics/molecular mechanics setup[71–73,135], helped us to explain the primary relaxation pathways of excited states in water solvated Trp. The calculations have been done by the group of prof. Marco Garavelli from University of Bologna.

6.1. Sample preparation

The sample has been bought from Sigma-Aldrich and used as received. After dissolving Trp in a water-based phosphate buffer solution of pH 7.4 we achieved a concentration of 36 mM and flowed it in a 150 μm thick wire-guided jet configuration, keeping the pump fluence below 300 $\mu J/cm^2$ to not induce solvated electrons coming from water. The steady-state absorption spectrum is shown in Figure 6.1, and is composed of the two singlet states La and Lb, as previously mentioned. The figure also reports the theoretical absorption curves with dashed lines, showing the total, as well as the separate shapes for the La and Lb bands, which agrees well with the experimental absorption (continuous line). Two different pump spectra are chosen to excite predominantly either La or Lb state, shown in corresponding colors, red for La and blue for Lb. The molecular structure of tryptophan in water solvent is also shown as an inset.

The different electronic nature (Figure 6.4) of these states implies a different response to the local solvent environment. The La state is characterized by significantly higher dipole moment due to the intramolecular charge transfer nature of the transition. On the other hand, the Lb state is composed of partial positive and negative charges delocalized over the indole chromophore, resulting in a dipole moment magnitude similar to the ground state. This will play an important role in interactions with the solvent that influences the overall dynamics.

6.2. Transient absorption

Figure 6.1b shows the TA map for the 4.37 eV excitation, where we expect to populate mostly the Lb state. We observe intense PA bands over the whole probing region covering

the SE signal that is expected in the 3.75-4 eV range based on the theoretical estimations (Figure 6.1e). The most pronounced spectral changes are observed above 3 eV, where we see simultaneous decay of the initially present strong PA1 band at 3.37 eV and rise of a PA2 band at 3.76 eV (Figure 6.1c) over the course of 5 ps of the measurement window, with an isosbestic point at 3.54 eV.

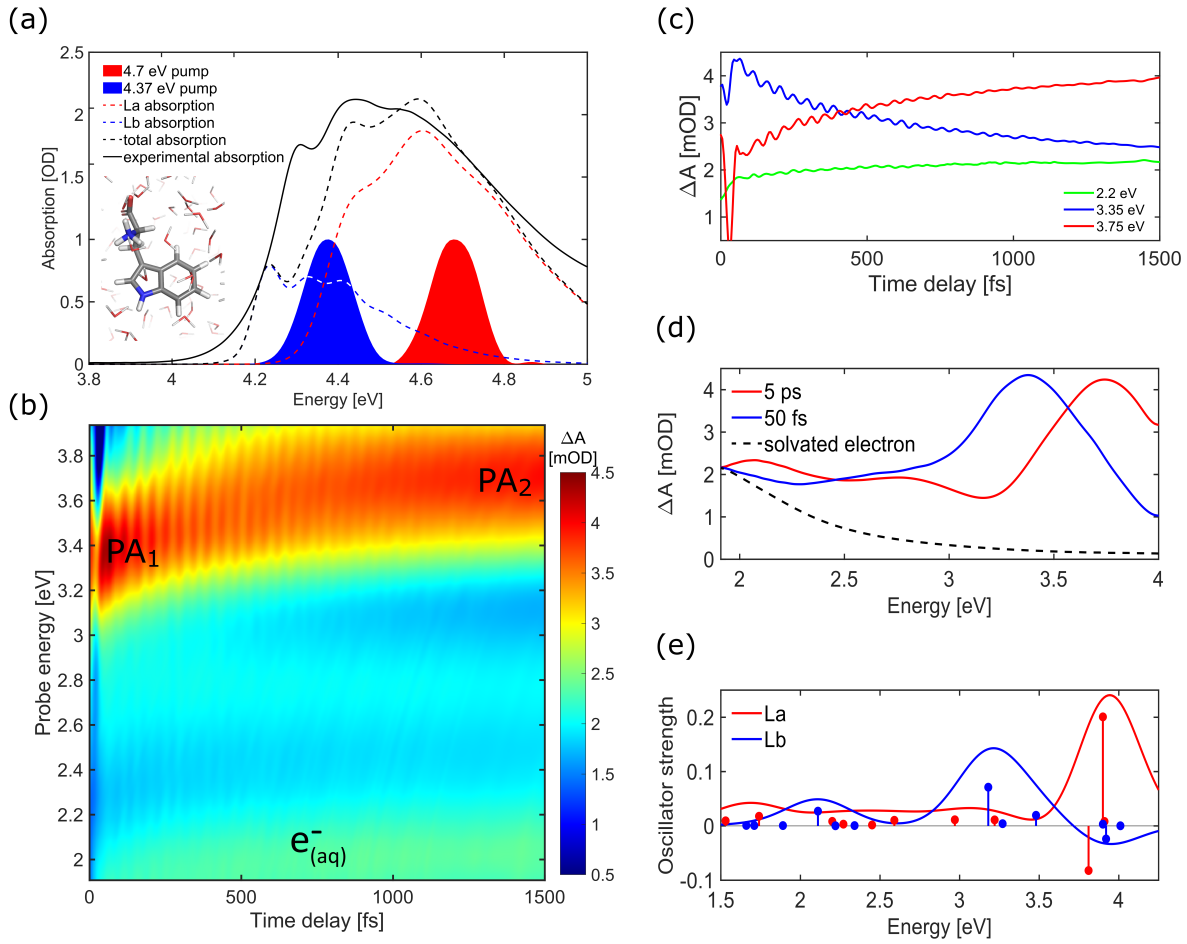

Figure 6.1: (a) Experimental steady state absorption of Trp in pH 7.4 buffer solution compared to the computed absorption spectra, distinguishing La and Lb regions. The pump spectra used in the experiment are shown with filled curves. Molecular structure of Trp shown as an inset. (b) Experimental TA map following excitation at 4.37 eV. (c) Temporal dynamics at selected energies, showing simulatneous decay of PA1 and rise of PA2, together with trace in the region of solvated electron peak absorption. (d) Experimental transient spectra at 50 fs and 5 ps delays. Solvated electron spectrum from literature is also shown[54]. (e) Theoretical transient spectra computed from the respective excited state minima of the Lb and La states.

Figure 6.1d show the spectral cuts at 5 ps and 50 fs after excitation (earlier times are obscured by the presence of coherent artifact), which can be compared with Figure 6.1e showing the computed transitions to higher energy excited states from either La or Lb. We can clearly see the similarities and interpret the PA1 and PA2 bands as signatures of Lb and La respectively, which shows that Lb is populated at early times and later transitions into La. In addition to main PA bands, there are also less intense absorption signals observed below 3 eV, composed of weaker peaks coming from La, Lb, and the presence of broad solvated electron band, which is the result of photoionization of the indole chromophore and subsequent trapping by water[54,136].

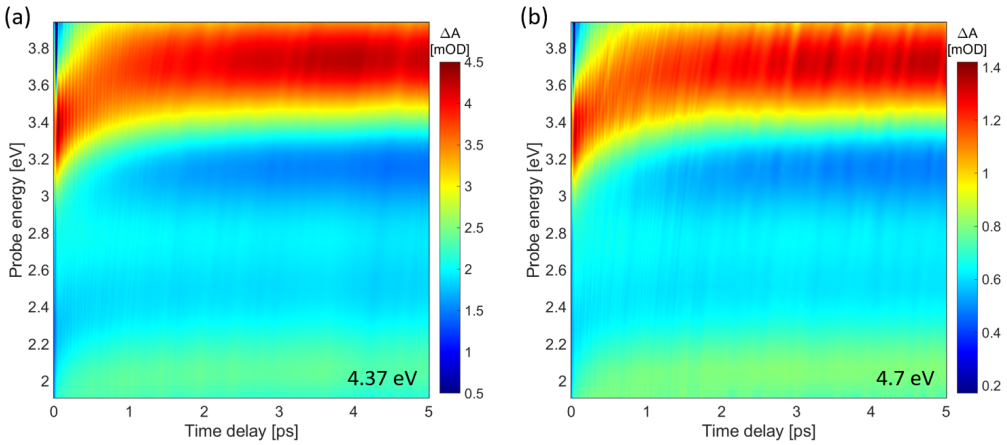

Figure 6.2: Comparison of TA maps for Trp excited with (a) 4.37 eV and (b) 4.7 eV pump pulse. We can see that the measurements show the same spectral dynamics in the two maps, with a slightly stronger solvated electron signal in the second case.

Interestingly exactly the same behavior is observed in case of the 4.7 eV pump, that should be prioritizing initial excitation of the La state. Figure 6.2 plots comparisons of TA maps for the two pump photon energies, to show that the only more significant difference between the measurements is the intensity of the solvated electron band. This is due to the difference in pump pulse energy between the measurements, as the photoionization is a nonlinear process.

6.3. Solvent-assisted dynamics

The presence of the Lb state signature PA at 50 fs delay, even when excitation is focused on the La state, is a strong indication of an ultrafast CI mediated La→Lb IC process occurring on an even faster timescale. It is also an experimental confirmation that the La state lies above the Lb state at the FC point. Therefore, characteristic La signal

being present at 5 ps, is an implication of an inversion of the order of these states and a back-transfer of the population to the La state. Global analysis of the experimental data (Figure 6.3) shows two time constants 220 fs and 1.1 ps. Since the initial La→Lb transfer takes place on the sub-50-fs timescale, we can assume that the two time constants from the fit, have to be connected to the secondary transfer from Lb to La.

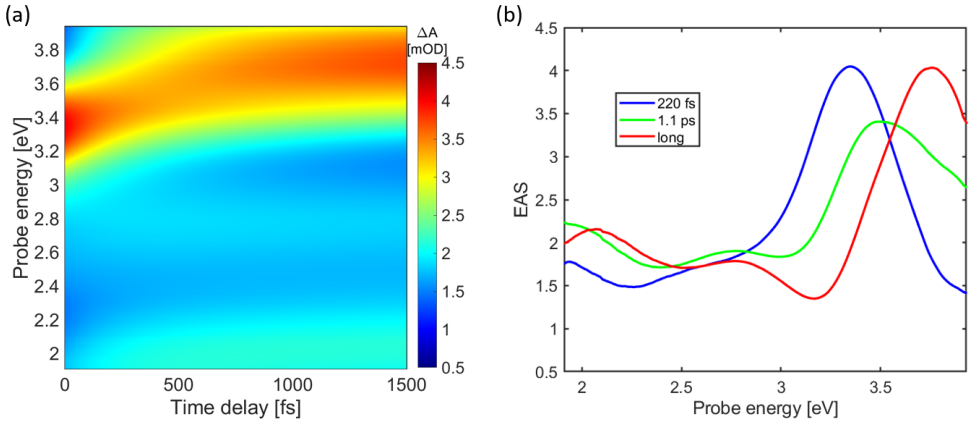

Figure 6.3: (a) Experimental TA map reconstructed based on the global fit. (b) Evolution associated spectra with their time constants.

As mentioned earlier, because of the polar nature of the La state (Figure 6.4), solvent plays an important role in explaining the observed dynamics. When the solvent is relaxed at the time of the pump interaction, the minimum of the Lb state is only 0.1 eV more stable than that of the La state. This favors the population of Lb initially. The large dipole moment of the La state is expected to induce a strong dynamical relaxation of the polar solvent, which would, in turn, cause the stabilization of the La state with respect to Lb, which is non-polar and less sensitive to the solvent reorganization, thus leading to an inversion of the state ordering.

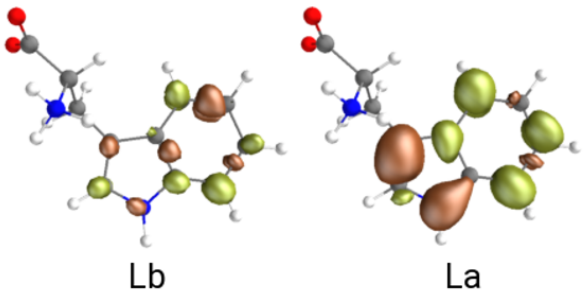

Figure 6.4: Difference density for Lb and La with respect to the ground state. Orange shows electron depletion and yellow electron addition compared to the ground state electron density.

After the excitation with the pump pulse, the solvent is in equilibrium with the GS electronic density of Trp and at the FC point, the La state is 0.3 eV above the Lb. The region of PES relevant for relevant for the discussed dynamics can be shown as a branching space around the Lb/La CI (Figure 6.5). This plane is described by a pair of vectors called gradient difference (GD) and derivative coupling (DC), which lift the degeneracy between the electronic surfaces and give rise to the double-cone topology characteristic of the PES around CI point. To better illustrate the dynamics, the character of the lower adiabatic surface (S_1) is shown as the magnitude of the transition dipole moment from the GS with a color map placed below the surface, which clearly separates the regions of La (red) and Lb (blue) character.

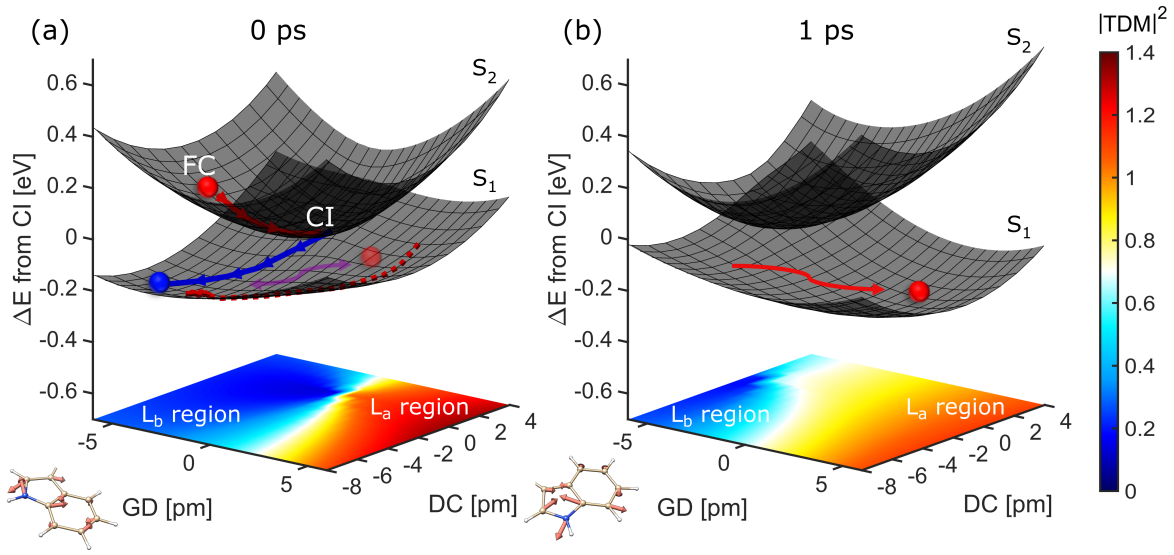

Figure 6.5: Trp branching space with (a) solvent relaxed to GS electron density, representative of early times after the interaction with the pump pulse, and (b) after 1 ps of non-equilibrium solvent dynamics around the La state. Geometrical deformations associated with the derivative coupling and gradient-difference vectors are depicted with arrows as insets on panel a. The plane below surfaces displays a map of transition dipole moment from the GS to the lower adiabatic surface S_1. This allows to characterize the nature of the S_1 surface as La (red), Lb (blue) or mixed. (a) Red and blue lines with arrows denote the projection of minimum energy path from the FC point to the CI and from the CI to the Lb minimum respectively. The dashed red line shows projection of the optimization from the La region to the Lb minimum. The wavepacket can coherently explore both regions as marked with purple arrow. (b) The stabilization of the La region due to the solvent interaction leads to transfer of population from Lb to La depicted schematically with a red arrow.

Vertical excitation to the La state in the FC region, positions the molecule on the top adiabatic surface, S_2. The first process that we then observe is the ultrafast sub-50-fs population of the Lb state. This is demonstrated here by the different possible paths that can be taken by the photoexcited system. If we track a minimum energy path (MEP) starting at the FC point of the S_2 surface (in the La state), it will guide us to the CI in a barrierless fashion (red line with arrows in Figure 6.5). Continuing the MEP path on the S_1 surface, would directly lead to the Lb-minimum (blue line with arrows in Figure 6.5). On the other hand, extrapolating along the direction of the MEP onto the S_1 surface, so assuming a momentum-conserving wavepacket across the CI, we will encounter a region of La character, which indicates that the crossing along the continuation of the MEP is largely diabatic. This region does not show a local minimum that could trap the population in the La region. Instead, the topography of the S_1 surface lays out a smooth relaxation path to the Lb region which is more stable energetically, shown by a full-dimensional geometry optimization from the La region on S_1 that ends up in the Lb region (projection on the branching plane shown by a red dashed line in Figure 6.5). These theoretical considerations strongly suggest that the Lb TA spectrum observed at 50 fs delay is the result of such ultrafast IC event which leads to a La→Lb population transfer, in contrast to previous studies[123].

Since the S_1 surface at early times is rather flat, it allows the hot wavepacket arriving from the S_2 surface to spread around and coherently explore regions of both characters. This is crucial to the population dynamics, as it lets fractions of the wavepacket in the La region polarize the solvent environment and in such a way cause large-scale solvent reorientation which leads to the electrostatic relaxation of the system. In order to understand this process, classical non-equilibrium dynamics simulation has been conducted and the adiabatic La-Lb energy gap has been tracked during the process. We found that the solvent relaxation around the Lb electron density doesn't change the state ordering, which makes it improbable as previously proposed[122], to undergo Lb→La IC from pure population of Lb. Contrary to this, solvent relaxation around the La electron density indicates the state ordering inversion within 100 fs, and continued adiabatic stabilization of La in the picosecond regime. This solvent influence on the La state, results in a sharp change in the PES topography, as demonstrated by the branching plane after 1 ps of solvent reorientation dynamics (Figure 6.5b). As expected, now the La region becomes more stable, and this allows the S_1 population to be collected in its minimum through a back-transfer from Lb. In contrast to the sub-50-fs CI-mediated La→Lb IC, this process is adiabatic, and observed in the experimental spectra as the decay of the PA1 and rise of the PA2, with a time constant of 220 fs.

6.4. Insight from coherent vibrations

Thanks to the very high temporal resolution of the experimental setup, exceeding by one order of magnitude that of previous experimental TA studies on Trp [119,121,124,137], we also observe coherent oscillations in the TA maps (Figure 6.6a), that are the result of molecular vibrations excited during the pumping process.

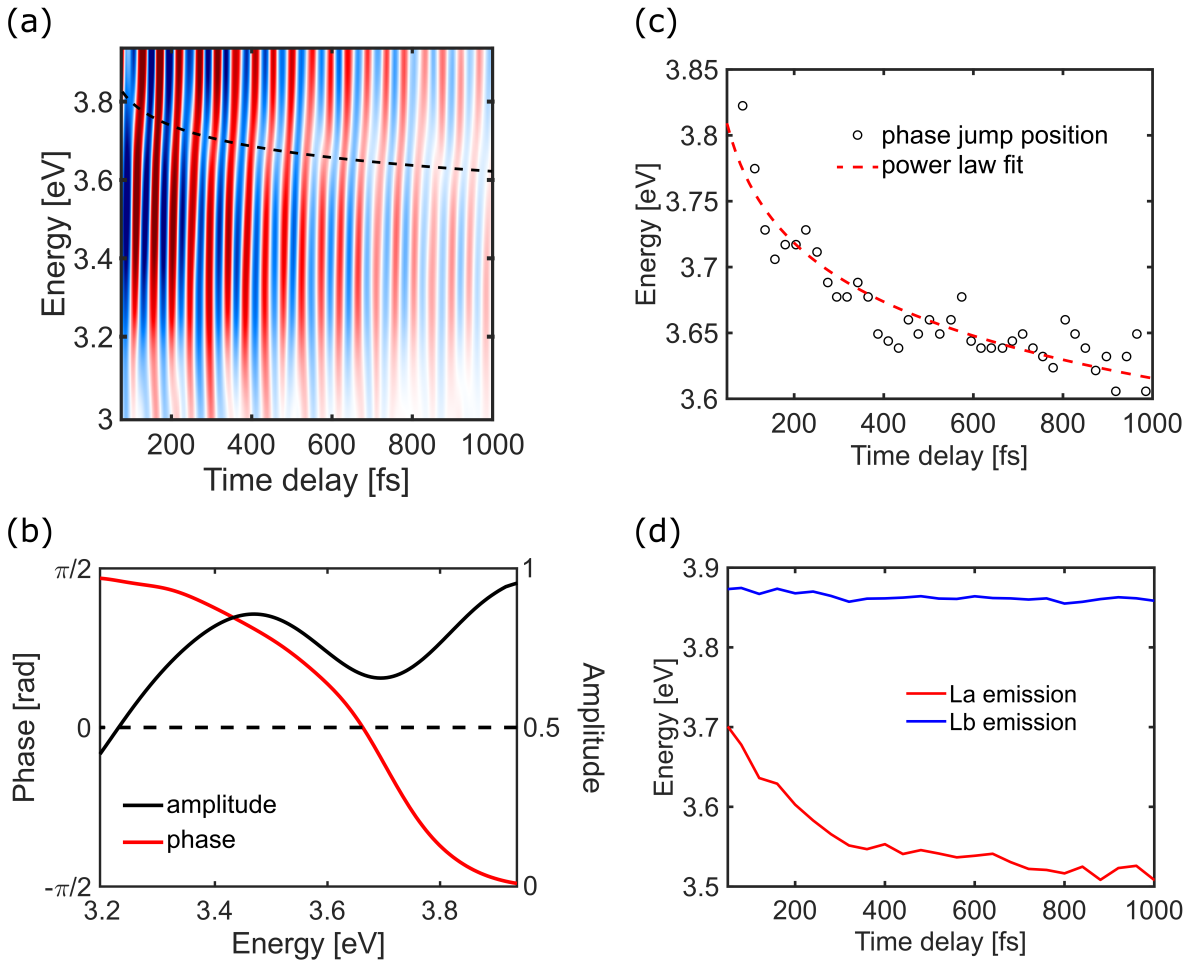

Figure 6.6: (a) Map of the oscillations extracted from the TA map with the location of the phase jump tracked with the dashed line from fit in the panel c. (b) Amplitude and phase of the FT of the oscillations map for the 720 $cm^{-}1$ frequency mode, showing a π phase jump across the peaks that can be associated with the central wavelength of the SE band. (c) Experimental phase jump positions read out from the oscillations map, showing continuous red-shift of the SE signal. (d) Emission energies from the La and Lb excited state minima computed along non-equilibrium relaxation of the solvent around Trp.

Fourier Transform of the oscillatory map in the 1.2 ps range reveals a 720 cm^{-1} mode dominating the entire probing window. We observe a characteristic amplitude node and the corresponding π phase jump at 3.7 eV (Figure 6.6b). The node appears at the position of the predicted SE band, and because GSB signals lie beyond the probing window, this lets us attribute it to the vibrational coherence of the ES. Moreover, we realized that the spectral position of this phase jump is red-shifting in time by ∼0.2 eV over the first picosecond (Figure 6.6c).

A decrease in the emission energy of the photoexcited state is evident in this shift. Non-equilibrium dynamics modeling of the emission energy evolution due to solvent response confirms that this red-shift is the fingerprint of the La emission (Figure 6.6d). On the other hand, for the Lb state, it leads to an insignificant change in emission energy. This presents a further proof that the La population has to be present at early times, even after direct excitation of the Lb state, and constitutes experimental proof for the previous assertion that the hot wavepacket is coherently exploring both Lb and La regions of the S_1 surface. Moreover, the emission energy red-shift observed here follows the solvent induced changes in the PES topography. This facilitates adiabatic population transfer by stabilizing the La state below the Lb state energy in 220 fs. During the continuation of the emission shift and after the inversion, the La state keeps relaxing and localizing its population in the minimum in 1.1 ps, as found from global analysis.

Through normal mode analysis, two main modes, at 1588 cm^{-1} and at 750 cm^{-1} (corresponding to the 720 cm^{-1} mode observed in the experiment) are recognized to be immediately initiated up photoexcitation of Trp. These modes display high overlap with the branching plane vectors and actively drive the coherent transfer of population. The 720 cm^{-1} frequency mode, together with the higher frequency one, connects the La and Lb regions on the S_1 surface so that the population can get around the CI through the inter-state coupling region. The oscillations remaining active on the picosecond timescale confirm that the branching plane vectors remain active as well. This is in agreement with the interpretation that the wavepacket instead of being trapped in the Lb region after the sub-50-fs IC from the La state, coherently explores the S_1 surface in both the Lb and La regions through the activate modes. As a result of long-living coherence, which causes both states to exist simultaneously at early times, the solvent relaxation around La is triggered, which lowers its energy with respect to Lb, leading to inversion of state ordering and full population of the La state.

6.5. Summary

To conclude, in this chapter we showed that, by combining high resolution ultrafast UV transient absorption spectroscopy with the high-level multiconfigurational CASPT2 theory within a hybrid QM/MM setup, the primary photoinduced dynamics of tryptophan are coherently driven by the different solvent response of the vibronically coupled lowest excited states, leading to complex dynamics on the femtosecond timescale. Initially, the ballistic access to the conical intersection enables sub-50-fs non-adiabatic population transfer from La to Lb. Following that, the resulting hot wavepacket coherently couples the La and Lb regions on the lower adiabatic surface, and by exploring the La region, triggers the solvent response to its polar character. Water reorganization significantly changes the PES topography and dynamically drives the minimum of the La state below the Lb state, promoting adiabatic transfer of the whole population to the La state in 220 fs. This process is supported by detailed analysis of the oscillations present in the TA map, that show a photoactive mode at 720 cm^{-1} with a characteristic phase jump, that red-shifts over time, tracking the position of the La state minimum. Understanding of this highly solvent-sensitive transition can further motivate adopting tryptophan as a probe of the local protein environment even on the ultrafast sub-ps timescales, potentially leading to more detailed explanation of the processes involved in the primary photoinduced protein dynamics.

Conclusions

The rapid development of femtosecond lasers, nonlinear optics, and computational techniques has been beneficial to improving ultrafast spectroscopy techniques and reaching the ever-shorter timescales and providing wider spectral access. Those maturing technologies allow us nowadays to study in deep detail the photoresponse of the biological molecules even in the difficult to reach UV region. As the DNA, amino acids, and proteins built from them are the most basic molecules which govern the biochemistry of the cell, this calls for a thorough understanding of their behavior at the molecular level. In this work, we aimed to show that with the available tools we are able to reach that goal.

We have first introduced the basic principles of ultrashort pulse description, managing dispersion, and generating tunable pulses through nonlinear optics that can be used as pump and probe pulses for transient absorption experiments. Then, the basic principles of such measurements have been presented together with the specification of the constructed UV transient absorption setup. Exploiting the broadband SHG of the tunable pulses generated from the visible NOPA, while passing through two compression stages, gave us access to tunable sub-20-fs UV pulses. Thanks to the ultrabroad probe pulses extending from the UV throughout the whole visible region, we were able to track the spectral signatures of various transitions in parallel, giving a broader view of the dynamics. Designing methods for sample delivery such as the wire-guided jet to optimize for minimal loss of temporal resolution allowed by the ultrashort pulses, helped us record the transient absorption traces together with coherent oscillations on top of them that were used for further insight about the underlying photoprocesses. Showing capabilities of the setup and the effectiveness of collaboration with the theoretical group, we have presented three studies of selected biomolecules.

In the first work, we have characterized uridine and 5-methyluridine, two pyrimidine RNA nucleosides that have been frequently studied in the past with various techniques. Yet, up until now, several main questions have been left unanswered. We have combined the high-resolution measurements in a broad spectral range with advanced dynamical simulations to present close agreement of experiment and theory and derive the ultimate conclusions about their decay pathways. In uridine we have shown a coherent ballistic

decay to the ground state, highlighting one of the modes involved in reaching the CI. On the other hand, in 5-methyluridine we disentangled the fast and slow time constants and properly assigned the faster one to the relaxation on the excited-state potential energy surface, while the slower was the internal conversion. The insight from computations shows how this is primarily caused by the initially present energy barrier due to the solvent arrangement around the methyl group and the higher inertia of the methyl group making it more difficult to reach the CI geometry. While in uridine there is clear long living dark $n\pi^*$ state, we have found only a very minor population residing in it in the case of 5-methyluridine, contrary to some of the previous literature.

The second study focused on the family of the epigenetic modifications of deoxycytidine, a DNA nucleoside that can be marked by methylation to signal gene regulation to the cell machinery, and the other three derivatives that are hypothesized to be more than just intermediate steps in the demethylation process. We have mapped out the major decay routes for all four epigenetic nucleosides finding that while 5-methyl-2'-deoxycytidine and 5-hydroxymethyl-2'-deoxycytidine are behaving very similarly and show a slowed-down version of deoxycytidine decay dynamics, with the population decaying to the ground state through a CI on several picosecond scale, the other two are much different. In 5-formyl-2'-deoxycytidine with the help of global analysis and the computations finding critical points of the potential energy surfaces, we were able to distinguish the minor path leading to the ground state as well as the significant population of the dark $n\pi^*$ state leading to ISC with the triplet in 2.1 ps. Such a fast and efficient triplet population could be responsible for photoinduced DNA damage or alternatively, could be used in medical applications as a phototherapeutic agent. In the last of the derivatives, 5-carboxyl-2'deoxycytidine, we found a distinct scenario, more akin to the uridine case, where most of the population rapidly decays to the ground state through a barrier-less conical intersection while only a minor part is left in longer living states.

Finally, we have presented the study of the brightest chromophore among the aromatic amino acids – tryptophan. While the later stages of its excited states' evolution have been known, the earliest events remained unexplained. We found a sub-50-fs CI from La to Lb state, which while not directly observable in the experiment, was hinted by the identical spectra recorded independently from which state has been initially excited, and confirmed through the computations. Moreover, we have explained the subsequent transfer of population back in 220 fs, from the Lb to the La state, which is driven by the dynamic solvent response around the population of the polar La state. While at the start the population is quickly transferred to the Lb, the potential energy surface is flat enough that the La state is periodically populated as well, through a vibrational coherence

coupling the two regions, which is also observed as the oscillatory modulation pattern of the transient spectra. Tracking the location of the phase jump in the oscillation map, which marks the energy of the emitting state, revealed how the La state is being brought lower in energy with respect to Lb, and collects all the population. This solvent-assisted inversion of the state ordering is not only a fundamentally interesting phenomenon to observe, but also it could be used as a precise tool for probing tryptophan-containing proteins in aqueous environments on the ultrafast timescales.

The measurements summarized above have definitely proven the constructed setup as a reliable tool for exploring ultrafast UV spectroscopy of primary photoinduced processes in biomolecules, allowing new discoveries of their basic photophysics. For the future measurements, we envision carrying further the lessons learned from the more basic molecules, and studying DNA strands and G-quadruplexes as well as small peptides and larger proteins. At the same time, improvement of the spectroscopic tools, such as development of a robust 2D UV spectroscopy setup would certainly help in disentangling the growing complexity of those systems.

Publications

- D. P. Schwinger, M. T. Peschel, T. Rigotti, P. Kabaciński, E. Thyrhaug, G. Cerullo, J. Hauer, R. de Vivie-Riedle, T. Bach. Photo-induced B-Cl bond fission in aldehyde-BCl_3 complexes: Theory, spectroscopy, and synthetic applications. In preparation.
- V. K. Jaiswal, P. Kabaciński, I. Conti, B. E. Nogueira de Faria, M. Gentile, A. M. de Paula, R. Borrego-Varillas, A. Nenov, G. Cerullo, M. Garavelli. Environment driven coherent population transfer governs the ultrafast photophysics of tryptophan. *J. Am. Chem. Soc.*, to be submitted.
- P. Kabaciński, M. Romanelli, E. Ponkkonen, V. K. Jaiswal, T. Carell, M. Garavelli, G. Cerullo, I. Conti. A unified description of ultrafast excited state decay processes in epigenetic deoxycytidine derivatives. *J. Phys. Chem. Lett.*, 12:11070-11077, 2021.
- R. Borrego-Varillas, A. Nenov, P. Kabaciński, I. Conti, L. Ganzer, A. Oriana, I. Delfino, O. Weingart, C. Manzoni, I. Rivalta, M. Garavelli, G. Cerullo. Real-time tracking of excited state decay pathways of pyrimidine nucleosides. *Nat. Comm.*, 12:7285, 2021.
- M. T. Peschel, P. Kabaciński, D. P. Schwinger, E. Thyrhaug, G. Cerullo, T. Bach, J. Hauer, R. De Vivie-Riedle. Activation of 2-cyclohexenone by BF_3 coordination: Mechanistic insights from theory and experiment. *Angew. Chem. Int. Ed.*, 60:10155-10163, 2021.
- E. Lucenti, A. Forni, A. Previtali, D. Marinotto, D. Malpicci, S. Righetto, C. Giannini, T. Virgilli, P. Kabaciński, L. Ganzer, U. Giovanella, C. Botta, E. Cariati. Unravelling the intricate photophysical behavior of 3-(pyridin-2-yl)triimidazotriazine AIE and RTP polymorphs. *Chem. Sci.* 11:7599-7608, 2020
- M. Forjan, G. Zgrablic, S. Vdovic, M. Sekutor, N. Basaric, P. Kabaciński, H.-M. Frey, A. Cannizzo, G. Cerullo. Photogeneration of quinone methide from adamantylphenol in an ultrafast non-adiabatic dehydration reaction. *Phys. Chem. Chem. Phys.*, 24:4384, 2022

Bibliography

[1] B. Alberts, D. Bray, K. Hopkin, A. Johnson, J. Lewis, M. Raff, K. Roberts, and P. Walter. *Essential Cell Biology*. Garland Science, 2009.

[2] W. J. Schreier, P. Gilch, and W. Zinth. Early events of DNA photodamage. *Annu. Rev. Phys. Chem.*, 66, 2015.

[3] K. Haiser, B. P. Fingerhut, K. Heil, A. Glas, T. T. Herzog, B. M. Pilles, W. J. Schreier, W. Zinth, R. de Vivie-Riedle, and T. Carell. Mechanism of UV-induced formation of dewar lesions in DNA. *Angew. Chem. Int. Ed.*, 51:408–411, 2012.

[4] G. P. Pfeifer and A. Besaratinia. UV wavelength-dependent DNA damage and human non-melanoma and melanoma skin cancer. *Photochem. Photobiol. Sci.*, 11: 90–97, 2012.

[5] C. T. Middleton, K. de La Harpe, C. Su, Y. K. Law, C. E. Crespo-Hernandez, and B. Kohler. DNA excited-state dynamics: from single bases to the double helix. *Annu. Rev. Phys. Chem.*, 60:217–239, 2009.

[6] J. M. L. Pecourt, J. Peon, and B. Kohler. Ultrafast internal conversion of electronically excited RNA and DNA nucleosides in water. *J. Am. Chem. Soc.*, 122: 9348–9349, 2000.

[7] J. M. L. Pecourt, J. Peon, and B. Kohler. DNA excited-state dynamics: ultrafast internal conversion and vibrational cooling in a series of nucleosides. *J. Am. Chem. Soc.*, 123:10370–10378, 2001.

[8] J. Peon and A. H. Zewail. DNA/RNA nucleotides and nucleosides: direct measurement of excited-state lifetimes by femtosecond fluorescence up-conversion. *Chem. Phys. Lett.*, 348:255–262, 2001.

[9] D. Onidas, D. Markovitsi, S. Marguet, A. Sharonov, and T. Gustavsson. Fluorescence properties of DNA nucleosides and nucleotides: a refined steady-state and femtosecond investigation. *J. Phys. Chem. B*, 106:11367–11374, 2004.

[10] S. Ullrich, T. Schultz, M. Z. Zgierski, and A. Stolow. Electronic relaxation dynamics

in DNA and RNA bases studied by time-resolved photoelectron spectroscopy. *Phys. Chem. Chem. Phys.*, 6:2796, 2004.

[11] H. R. Hudock, B. G. Levine, A. L. Thompson, H. Satzger, D. Townsend, N. Gador, S. Ullrich, A. Stolow, and T. J. Martinez. Ab initio molecular dynamics and time-resolved photoelectron spectroscopy of electronically excited uracil and thymine. *J. Phys. Chem. A*, 111:8500–8508, 2007.

[12] W. Domcke and D. R. Yarkony. Role of conical intersections in molecular spectroscopy and photoinduced chemical dynamics. *Ann. Rev. Phys. Chem.*, 65, 2012.

[13] S. Tommasi, M. F. Denissensko, and G. P. Pfeifer. Sunlight induces pyrimidine dimers preferentially at 5-methylcytosine bases. *Cancer Res*, 57:4727–4730, 1997.

[14] I. Conti, L. Martinez-Fernandez, L. Esposito, S. Hofinger, A. Nenov, M. Garavelli, and R. Improta. Multiple electronic and structural factors control cyclobutane pyrimidine dimer and 6-4 thymine-thymine photodimerization in a DNA duplex. *Chem. - Eur. J.*, 23:15177–15188, 2017.

[15] G. P. Pfeifer, Y.-H. You, and A. Besaratinia. Mutations induced by ultraviolet light. *Mutat. Res. Mol. Mech. Mutagen*, 571:19–31, 2005.

[16] M. K. Shukla and Leszczynski J. Electronic spectra, excited state structures and interactions of nucleic acid bases and base assemblies: a review. *J. Biomol. Struct. Dyn.*, 25, 2007.

[17] R. Improta, F. Santoro, and L. Blancafort. Quantum mechanical studies on the photophysics and the photochemistry of nucleic acids and nucleobases. *Chem. Rev.*, 116:3540–3593, 2016.

[18] R. J. Malone, A. M. Miller, and B. Kohler. Singlet excited-state lifetimes of cytosine derivatives measured by femtosecond transient absorption. *Photochem. Photobiol.*, 77, 2003.

[19] M. Z. Zgierski, S. Patchkovskii, T. Fujiwara, and E. C. Lim. The role of out-of-plane deformations in subpicosecond internal conversion of photoexcited purine bases: absence of the ultrafast decay channel in propanodeoxyguanosine. *Chem. Phys. Lett.*, 440, 2007.

[20] M. Z. Zgierski, T. Fujiwara, W. G. Kofron, and E. C. Lim. Highly effective quenching of the ultrafast radiationless decay of photoexcited pyrimidine bases by covalent modifications: photophysics of 5,6-trimethylenecytosine and 5,6-trimethyleneuracil. *Phys. Chem. Chem. Phys.*, 9, 2007.

[21] P. M. Hare, C. E. Crespo-Hernandez, and B. Kohler. Internal conversion to the electronic ground state occurs via two distinct pathways for pyrimidine bases in aqueous solution. *Proc. Natl. Acad. Sci. USA*, 104:435–440, 2007.

[22] B. Kohler. Nonradiative decay mechanisms in DNA model systems. *J. Phys. Chem. Lett.*, 1:2047–2053, 2010.

[23] C. E. Crespo-Hernandez, B. Cohen, P. M. Hare, and B. Kohler. Ultrafast excited-state dynamics in nucleic acids. *Chem. Rev.*, 104:1977–2019, 2004.

[24] I. Conti and M. Garavelli. Evolution of the excitonic state of DNA stacked thymines: intrabase $\pi\pi^* \rightarrow S_0$ decay paths account for ultrfast (subpicosecond) and longer (>100 ps) deactivations. *J. Phys. Chem. Lett.*, 9:2373–2379, 2018.

[25] S. Barik. The uniqueness of tryptophan in biology: properites, metabolism, interactions and localzation in proteins. *Int. J. Mol. Sci.*, 21, 2020.

[26] C. Consani, G. Aubock, F. Van Mourik, and M Chergui. Ultrafast tryptophan-to-heme electron transfer in myoglobins revealed by UV 2D spectroscopy. *Science*, 339: 1586–1589, 2013.

[27] J. Briand, J. Leonard, and S. Haacke. Ultrafast photo-induced reaction dynamics in bacteriorhodopsin and its trp mutants. *J. Opt.*, 12:084004, 2010.

[28] A. Nenov, I. Rivalta, G. Cerullo, S. Mukamel, and M. Garavelli. Disentangling peptide configurations via two-dimensional electronic spectroscopy: Ab initio simulations beyond the frenkel exciton hamiltonian. *J. Phys. Chem. Lett.*, 5:767–771, 2014.

[29] A. R. Bizzarri, D. Brida, S. Santini, G. Cerullo, and S. Cannistraro. Ultrafast pump-probe study of the excited-state charge-transfer dynamics in blue copper rusticyanin. *J. Phys. Chem. B*, 116:4192–4198, 2012.

[30] C. Shih, A. K. Museth, M. Abrahamsson, A. M. Blanco-Rodriguez, A. J. Di Bilio, J. Sudhamsu, B. R. Crane, K. L. Ronayne, M. Towrie, A. Vlcek, J. H. Richards, J. R. Winkler, and H. B. Gray. Tryptophan-accelerated electron flow through proteins. *Science*, 320:1760–1762, 2008.

[31] H. S. Shafaat, B. S. Leigh, M. J. Tauber, and J. E. Kim. Spectroscopic comparison of photogenerated tryptophan radicals in azurin: Effects of local environment and structure. *J. Am. Chem. Soc.*, 132:9030–9039, 2010.

[32] T. Cimei, A. R. Bizzarri, S. Cannistraro, G. Cerullo, and S. De Silvestri. Vibrational

coherence in azurin with impulsive excitation of the LMCT absorption band. *Chem. Phys. Lett.*, 362:497–503, 2002.

[33] Ediz Herkert, Nicole Slesiona, Martina Elisena Recchia, Thomas Deckert, Maria F Garcia-Parajo, Eric Michele Fantuzzi, Andrea Pruccoli, Imaiyan Chitra Ragupathy, Dominykas Gudavičius, Hervé Rigneault, Jan Majer, Andreas Zumbusch, Eleanor Munger, Sophie Brasselet, Arwyn T Jones, Peter Watson, Stephen A Boppart, Vikramdeep Singh, Saurabh Borkar, Frank E Quintela Rodriguez, Wolfgang Langbein, Vasilis Petropoulos, Niek F van Hulst, Margherita Maiuri, Giulio Cerullo, Daniele Brida, Filippo Troiani, Carlo Andrea Rozzi, Elisa Molinari, Mikas Vengris, and Paola Borri. Roadmap on bio-nano-photonics. *J. Opt.*, 23, 2021.

[34] M. Maiuri, M. Garavelli, and G. Cerullo. Ultrafast spectroscopy: state of the art and open challenges. *J. Am. Chem. Soc.*, 142, 2020.

[35] A. Cannizzo. Ultrafast UV spectroscopy: from a local to a global view of dynamical processes in macromolecules. *Phys. Chem. Chem. Phys.*, 14, 2012.

[36] M. Chergui. Ultrafast molecular photophysics in the deep-ultraviolet. *J. Chem. Phys.*, 150, 2019.

[37] A. M. Weiner. *Ultrafast Optics*. John Wiley & Sons, Inc., 2008.

[38] G. P. Agrawal. *Nonlinear Fiber Optics*. Academic Press, 2013.

[39] E. Treacy. Optical pulse compression with diffraction gratings. *IEEE J. Quantum Electron.*, 5, 1969.

[40] O. E. Martinez, J. P. Gordon, and R. L. Fork. Negative group-velocity dispersion using refraction. *J. Opt. Soc. Am. A*, 1, 1984.

[41] R. Szipocs, K. Ferencz, C. Spielmann, and F. Krausz. Chirped multilayer coatings for broadband dispersion control in femtosecond lasers. *Opt. Lett.*, 19, 1994.

[42] R. W. Boyd. *Nonlinear Optics*. Elsevier, 2008.

[43] C. Manzoni and G. Cerullo. Design criteria for ultrafast optical parametric amplifiers. *J. Opt.*, 18, 2016.

[44] S. A. Kovalenko, A. L. Dobryakov, J. Ruthmann, and N. P. Ernsting. Femtosecond spectroscopy of condensed phases with chirped supercontinuum probing. *Phys. Rev. A*, 59, 1999.

[45] D. Polli, M. R. Antognazza, D. Brida, G. Lanzani, G. Cerullo, and S. De Silvestri.

Broadband pump-probe spectroscopy with sub-10-fs resolution for probing ultrafast internal conversion and coherent phonons in carotenoids. *Chem. Phys.*, 350, 2008.

[46] R. Berera, R. van Grondelle, and J. T. M. Kennis. Ultrafast transient absorption spectroscopy: principles and application to photosynthetic systems. *Photosynth. Res.*, 101, 2009.

[47] J. J. Snellenburg, S. P. Laptenok, R. Seger, K. M. Mullen, and I. H. M. van Stokkum. Glotaran: A Java-based graphical user interface for the R package TIMP. *Journal of Statistical Software*, 49, 2012.

[48] M. Liebel, C. Schnedermann, T. Wende, and P. Kukura. Principles and applications of broadband impulsive vibrational spectroscopy. *J. Phys. Chem. A*, 119, 2015.

[49] M. Lorenc, M. Ziolek, R. Naskrecki, J. Karolczak, J. Kubicki, and A. Maciejewski. Artifacts in femtosecond transient absorption spectroscopy. *Appl. Phys. B*, 74, 2002.

[50] K. Ekvall, P. van der Meulen, C. Dhollande, L.-E. Berg, S. Pommeret, R. Naskrecki, and J.-C. Mialocq. Cross phase modulation artifact in liquid phase transient absorption spectroscopy. *J. Appl. Phys.*, 87, 2000.

[51] Bastian Baudish. *Time resolved broadband spectroscopy from UV to NIR: Beneficial use of the coherent artifact and pyrene dynamics.* PhD thesis, Ludwig-Maximilians-Universitat Munchen, 2017.

[52] R. Borrego-Varillas, L. Ganzer, G. Cerullo, and C. Manzoni. Ultraviolet transient absorption spectrometer with sub-20-fs time resolution. *Appl. Sci.*, 8:989, 2018.

[53] R. Borrego-Varillas, A. Oriana, F. Branchi, S. De Silvestri, G. Cerullo, and C. Manzoni. Optimized ancillae generation for ultra-broadband two-dimensional spectral-shearing interferometry. *JOSA B*, 32:1851–1855, 2015.

[54] B. Abel, U. Buck, A. L. Sobolewski, and W. Domcke. On the nature and signatures of the solvated electron in water. *Phys. Chem. Chem. Phys.*, 14:22–34, 2012.

[55] D. Polli, D. Brida, S. Mukamel, G. Lanzani, and G. Cerullo. Effective temporal resolution in pump-probe spectroscopy with strongly chirped pulses. *Phys. Rev. A*, 82, 2010.

[56] I. H. Malitson. Interspecimen comparison of the refractive index of fused silica. *J. Opt. Soc. Am.*, 55, 1965.

[57] A. Picchiotti, V. I. Prokhorenko, and R. J. Dwayne Miller. A closed-loop pump-

driven wire-guided flow jet for ultrafast spectroscopy of liquid samples. *Rev. Sci. Instrum.*, 86:093105, 2015.

[58] T. Kobayashi and Y. Kida. Ultrafast spectroscopy with sub-10 fs deep-ultraviolet pulses. *Phys. Chem. Chem. Phys.*, 14:6200, 2012.

[59] V. I. Prokhorenko, A. Picchiotti, M. Pola, A. G. Dijkstra, and R. J. Dwayne Miller. New insights into the photophysics of dna nucleobases. *J. Phys. Chem. Lett.*, 7: 4445–4450, 2016.

[60] T. Gustavsson, A. Sharonov, and D. Markovistsi. Thymine, thymidine and thymidine 5'-monophosphate studied by femtosecond fluorescence upconversion spectroscopy. *Chem. Phys. Lett.*, 351:195–200, 2002.

[61] B. Cohen, C. E. Crespo-Hernandez, and B. Kohler. Strickler-Berg analysis of excited singlet state dynamics in DNA and RNA nucleosides. *Faraday Discuss*, 127:137–147, 2004.

[62] F. Buchner, A. Nakayama, S. Yamazaki, H.-H. Ritze, and A. Lubcke. Excited-state relaxation of hydrated thymine and thymidine measured by liquid-jet photoelectron spectroscopy: experiment and simulation. *J. Am. Chem. Soc.*, 137:2931–2938, 2015.

[63] T. Gustavsson, A. Banyasz, R. Improta, and D. Markovitsi. Femtosecond fluorescence studies of DNA/RNA constituents. *J. Phys. Conf. Ser.*, 261, 2011.

[64] B. A. Erickson, Z. N. Heim, E. Pieri, E. Liu, T. J. Martinez, and D. M. Neumark. Relaxation dynamics of hydrated thymine, thymidine, and thymidine monophosphate probed by liquid jet time-resolved photoelectron spectroscopy. *J. Phys. Chem. A*, 123:10676–10684, 2019.

[65] M. M. Brister and C. E. Crespo-Hernandez. Excited-state dynamics in the RNA nucleotide uridine 5'-monophosphate investigated using femtosecond broadband transient absorption spectroscopy. *J. Phys. Chem. Lett.*, 10:2156–2161, 2019.

[66] B. Xue, A. Yabushita, and T. Kobayashi. Ultrafast dynamics of uracil and thymine studied using a sub-10 fs deep ultraviolet laser. *Phys. Chem. Chem. Phys.*, 18: 17044–17053, 2016.

[67] T. Gustavsson, A. Banyasz, E. Lazzarotto, D. Markovitsi, G. Scalmani, M. J. Frisch, V. Barone, and R. Improta. Singlet excited-state behavior of uracil and thymine in aqueous solution: A combined experimental and computational study of 11 uracil derivatives. *J. Am. Chem. Soc.*, 128:607–619, 2006.

[68] J. C. Tully. Mixed quantum-classical dynamics. *Faraday Discuss*, 110:407–419, 1998.

[69] S. Hammes-Schiffer and J. C. Tully. Proton transfer in solution: Molecular dynamics with quantum transitions. *J. Chem. Phys.*, 101:4657–4667, 1994.

[70] G. Granucci and M. Persico. Critical appraisal of the fewest switches algorithm for surface hopping. *J. Chem. Phys.*, 126:134114, 2007.

[71] P.-O. Widmark, P.-A. Malmqvist, and B. O. Roos. Density matrix averaged atomic natural orbital (ANO) basis sets for correlated molecular wave functions. *Theor. Chim. Acta*, 77:291–306, 1990.

[72] O. Weingart, A. Nenov, P. Altoe, I. Rivalta, J. Segarra-Marti, I. Dokukina, and M. Garavelli. COBRAMM 2.0 - A software interface for tailoring molecular electronic structure calculations and running nanoscale (QM/MM) simulations. *J. Mol. Model.*, 24:271, 2018.

[73] F. Aquilante and et al. Modern quantum chemistry with [Open]Molcas. *J. Chem. Phys.*, 152:214117, 2020.

[74] R. Salomon-Ferrer, D. A. Case, and R. C. Walker. An overview of the Amber biomolecular simulation package. *Wiley Interdiscip. Rev. Comput. Mol. Sci.*, 3: 198–210, 2013.

[75] L. Du and Z. Lan. An on-the-fly surface-hopping program JADE for nonadiabatic molecular dynamics of polyatomic systems: implementation and applications. *J. Chem. Theory Comput.*, 11:1360–1374, 2015.

[76] R. Borrego-Varillas, A. Nenov, P. Kabacinski, I. Conti, L. Ganzer, A. Oriana, V. K. Jaiswal, I. Delfino, O. Weingart, C. Manzoni, I. Rivalta, M. Garavelli, and G. Cerullo. Tracking excited state decay mechanisms of pyrimidine nucleosides in real time. *Nat. Comm.*, 12:7285, 2021.

[77] A. Pepino, J. Segarra-Marti, A. Nenov, R. Improta, and M. Garavelli. Resolving ultrafast photoinduced deactivations in water-solvated pyrimidine nucleosides. *J. Phys. Chem. Lett.*, 8:1777–1783, 2017.

[78] S. Matsika. Radiationless decay of excited states of uracil through conical intersections. *J. Phys. Chem. A*, 108:7584–7590, 2004.

[79] J. P. Zauleck, M. T. Peschel, F. Rott, S. Thallmair, and R. de Vivie-Riedle. Ultrafast

reactive quantum dynamics coupled to classical solvent dynamics using an ehrenfest approach. *J. Phys. Chem. A*, 122:2849–2857, 2018.

[80] A. J. Pepino, J. Segarra-Marti, A. Nenov, I. Rivalta, R. Improta, and M. Garavelli. UV-induced long-lived decays in solvated pyrimidine nucleosides resolved at the MS-CASPT2/MM level. *Phys. Chem. Chem. Phys.*, 20:6877–6890, 2018.

[81] A. T. N. Kumar, F. Rosca, A. Widom, and P. M. Champion. Investigations of amplitude and phase excitation profiles in femtosecond coherence spectroscopy. *J. Chem. Phys.*, 114:701, 2001.

[82] T. Carell, M. Q. Kurz, M. Muller, M. Rossa, and F. Spada. Non-canonical bases in the genome: The regulatory information layer in DNA. *Angew. Chem. Int. Ed.*, 57:4296–4312, 2018.

[83] T. Carell, C. Brandmayr, A. Hienzsch, M. Muller, D. Pearson, V. Reiter, I. Thoma, P. Thumbs, and M. Wagner. Structure and function of noncanonical nucleobases. *Angew. Chem. Int. Ed.*, 51:7110–7131, 2012.

[84] C. S. Nabel, S. A. Manning, and R. M. Kohli. The curious chemical biology of cytosine: deamination, methylation and oxidation as modulators of genomic potential. *ACS Chem. Biol.*, 7:20–30, 2012.

[85] X. Yang, H. Han, D. D. DeCarvalho, F. D. Lay, and G. Jones, P. A. Liang. Gene body methylation can alter gene expression and is a therapeutic target in cancer. *Cancer Cell*, 26:577–590, 2014.

[86] L. Shen, C.-X. Song, C. He, and Y. Zhang. Mechanism and function of oxidative reversal of DNA and RNA methylation. *Annu. Rev. Biochem.*, 83:585–614, 2014.

[87] A. C. Drohat and C. T. Coey. Role of base excision "repair" enzymes in erasing epigenetic marks from DNA. *Chem. Rev.*, 116:12711–12729, 2016.

[88] S. Kriaucionis and N. Heintz. The nuclear DNA base 5-hydroxymethylcytosine is present in purkinje neurons and the brain. *Science*, 324:929–930, 2009.

[89] T. Pfaffender, B. Hackener, M. Truβ, M. Munzel, M. Muller, C. A. Deiml, C. Hagemeier, and T. Carell. The discovery of 5-formylcytosine in embryonic stem cell DNA. *Angew. Chem. Int. Ed.*, 50:7008–7012, 2011.

[90] S. Ito, L. Shen, Q. Dai, S. C. Wu, L. B. Collins, J. A. Swenberg, C. He, and Y. Zhang. Tet proteins can covert 5-methylcytosine to 5-formylcytosine and 5-carboxylcytosine. *Science*, 333:1300–1303, 2011.

[91] C. You, D. Ji, X. Dai, and Y. Wang. Effects of TET-mediated oxidation products of 5-methylcytosine on DNA transcription in vitro and in mammalian cells. *Sci. Rep.*, 2015:7052, 2015.

[92] X. Lu, B. S. Zhao, and C. He. TET family proteins: oxidation activity, interacting molecules, and functions in diseases. *Chem. Rev.*, 115:2225–2239, 2015.

[93] M. Tahiliani, K. P. Koh, Y. Shen, W. A. Pastor, H. Bandukwala, Y. Brudno, S. Agarwal, L. M. Iyer, D. R. Liu, L. Aravind, and A. Rao. Conversion of 5-methylcytosine to 5-hydroxymethylcytosine in mammalian DNA by MLL partner TET1. *Science*, 324:930–935, 2009.

[94] L. Martinez-Fernandez, A. J. Pepino, J. Segarra-Marti, A. Banyasz, M. Garavelli, and R. Improta. Computing the absorption and emission spectra of 5-methylcytidine in different solvents: a test-case for different solvation models. *J. Chem. Theory Comput.*, 12:4430–4439, 2016.

[95] L. Esposito, A. Banyasz, T. Douki, M. Perron, D. Markovitsi, and R. Improta. Effect of C5-methylation of cytosine on the photoreactivity of DNA: A joint experimental and computational study of TCG trinucleotides. *J. Am. Chem. Soc.*, 136:10838–10841, 2014.

[96] A. Giussani, I. Conti, A. Nenov, and M. Garavelli. Photoinduced formation mechanism of the thymine-thymine (6-4) adduct in DNA; a QM(CASPT2//CASSCF):MM(AMBER). *Faraday Discuss.*, 207:375–387, 2018.

[97] P. Kabacinski, M. Romanelli, E. Ponkkonen, V. K. Jaiswal, T. Carell, M. Garavelli, G. Cerullo, and I. Conti. Unified description of ultrafast excited state decay processes in epigenetic deoxycytidine derivatives. *J. Phys. Chem. Lett.*, 12:11070–11077, 2021.

[98] L. Martinez-Fernandez, A. Banyasz, L. Esposito, D. Markovitsi, and R. Improta. UV-induced damage to DNA: effect of cytosine methylation on pyrimidne dimerization. *Angew. Chem. Int. Ed.*, 57:4296–4312, 2018.

[99] S.-I. Kim and G. P. Pfeifer. The epigenetic DNA modification 5-carboxylcytosine promotes high levels of cyclobutane pyrimidine dimer formation upon UVB irradiation. *Genome Instability & Disease*, 2:59–69, 2021.

[100] Q. Song, V. J. Cannistraro, and J.-S. Taylor. Synergistic modulation of cyclobutane pyrimidine dimer photoproduct formation and deamination at a T^mCG site over a

full helical DNA turn in a nucleosome core particle. *Nucleic Acids Research*, 42: 13122–13133, 2014.

[101] V. J. Cannistraro and J.-S. Taylor. Acceleration of 5-methylcytosine deamination in cyclobutane dimers by G and its implications for UV-induced C-to-T mutation hotspots. *J. Mol. Biol.*, 392:1145–1157, 2009.

[102] C. Ma, C.-W. Cheng, C. T.-L. Chan, R. C.-T. Chan, and W.-M. Kwok. Remarkable effects of solvent and substitution on the photo-dynamics of cytosine: A femtosecond broadband time-resolved fluorescence and transient absorption study. *Phys. Chem. Chem. Phys.*, 17:19045–19057, 2015.

[103] L. Martinez-Fernandez, A. J. Pepino, J. Segarra-Marti, J. Jovaisaite, I. Vaya, A. Nenov, D. Markovitsi, T. Gustavsson, A. Banyasz, M. Garavelli, and R. Improta. Photophysics of deoxycytidine and 5-methyldeoxycytidine in solution: A comprehensive picture by quantum mechanical calculations and femtosecond fluorescence spectroscopy. *J. Am. Chem. Soc.*, 139:7780–7791, 2017.

[104] X. Wang, Z. Zhou, Y. Tang, J. Chen, D. Zhong, and J. Xu. Excited state decay pathways of 2'-deoxy-5-methylcytidine and deoxycytidine revisited in solution: A comprehensive kinetic study by femtosecond transient absorption. *J. Phys. Chem. B*, 122:7027–7037, 2018.

[105] X. Wang, Y. Yu, Z. Zhou, Y. Liu, Y. Yang, J. Xu, and J. Chen. Ultrafast intersystem crossing in epigenetic DNA nucleoside 2'-deoxy-5-formylcytidine. *J. Phys. Chem. B*, 123:5782–5790, 2019.

[106] J. Xing, Y. Ai, Y. Liu, J. Du, W. Chen, Z. Lu, and X. Wang. Theoretical studies on the photophysics and photochemistry of 5-formylcytosine and 5-carboxylcytosine: The oxidative products of epigenetic modification of cytosine in DNA. *J. Phys. Chem. B*, 122:2704–2714, 2018.

[107] X. Wang, L. Martinez-Fernandez, Y. Zhang, K. Zhang, R. Improta, B. Kohler, J. Xu, and J. Chen. Solvent-dependent stabilization of a charge transfer state is the key to ultrafast triplet state formation in an epigenetic DNA nucleoside. *Chem. - Eur. J.*, 27:10932–10940, 2021.

[108] I. Conti, G. Cerullo, A. Nenov, and M. Garavelli. Ultrafast spectroscopy of photoactive molecular systems from first principles: Where we stand today and where we are going. *J. Am. Chem. Soc.*, 142:16117–16139, 2020.

[109] A. Frances-Monerris, M. Lineros-Rosa, M. A. Miranda, V. Lhiaubet-Vallet, and

A. Monari. Photoinduced intersystem crossing in DNA oxidative lesions and epigenetic intermediates. *Chem. Commun.*, 56:4404–4407, 2020.

[110] J. Xu, B. Chen, P. Callis, P. L. Muino, H. Rozeboom, J. Broos, D. Toptygin, L. Brand, and J. R. Knutson. Picosecond fluorescence dynamics of tryptophan and 5-fluorotryptophan in monellin: Slow water–protein relaxation unmasked. *J. Phys. Chem. B*, 119:4230–4239, 2015.

[111] Y. Qin, C.-W. Chang, L. Wang, and D. Zhong. Validation of response function construction and probing heterogeneous protein hydration by intrinsic tryptophan. *J. Phys. Chem. B*, 116:13320–13330, 2012.

[112] R. B. Fenwick, D. Oyen, H. J. Dyson, and P. E. Wright. Slow dynamics of tryptophan–water networks in proteins. *J. Am. Chem. Soc.*, 140:675–682, 2018.

[113] P. Houston, N. Macro, M. Kang, L. Chen, J. Yang, L. Wang, Z. Wu, and D. Zhong. Ultrafast dynamics of water–protein coupled motions around the surface of eye crystallin. *J. Am. Chem. Soc.*, 142:3997–4007, 2020.

[114] T. Li, A. A. Hassanali, Y.-T. Kao, D. Zhong, and S. J. Singer. Hydration dynamics and time scales of coupled water-protein fluctuations. *J. Am. Chem. Soc.*, 129: 3376–3382, 2007.

[115] J. Yang, Y. Wang, L. Wang, and D. Zhong. Mapping hydration dynamics around a β-barrel protein. *J. Am. Chem. Soc.*, 139:4399–4408, 2017.

[116] L. J. Andrews and L. S. Forster. Protein difference spectra. effect of solvent and charge on tryptophan. *Biochemistry*, 11:1875–1879, 1972.

[117] S. Soorkia, C. Jouvet, and G. Gregoire. Uv photoinduced dynamics of conformer-resolved aromatic peptides. *Chem. Rev.*, 120:3296–3327, 2020.

[118] X. Shen and J. R. Knutson. Subpicosecond fluorescence spectra of tryptophan in water. *J. Phys. Chem. B*, 105:6260–6265, 2001.

[119] D. Sharma, J. Leonard, and S. Haacke. Ultrafast excited-state dynamics of tryptophan in water observed by transient absorption spectroscopy. *Chem. Phys. Lett.*, 489:99–102, 2010.

[120] A. J. Ruggiero, D. C. Todd, and G. R. Fleming. Subpicosecond fluorescence anisotropy studies of tryptophan in water. *J. Am. Chem. Soc*, 112:1003–1014, 1990.

[121] A. Ajdarzadeh, C. Consani, O. Bram, A. Tortschanoff, A. Cannizzo, and M. Cher-

gui. Ultraviolet transient absorption, transient grating and photon echo studies of aqueous tryptophan. *Chem. Phys.*, 422:47–52, 2013.

[122] J. Yang, L. Zhang, L. Wang, and D. Zhong. Femtosecond conical intersection dynamics of tryptophan in proteins and validation of slowdown of hydration layer dynamics. *J. Am. Chem. Soc.*, 134:16460–16463, 2012.

[123] O. Bräm, A. Ajdarzadeh Oskouei, A. Tortschanoff, F. van Mourik, M. Madrid, J. Echave, A. Cannizzo, and M. Chergui. Relaxation dynamics of tryptophan in water: A uv fluorescence up-conversion and molecular dynamics study. *The Journal of Physical Chemistry A*, 114:9034–9042, 2010.

[124] J. Leonard, D. Sharma, B. Szafarowicz, K. Torgasin, and S. Haacke. Formation dynamics and nature of tryptophan's primary photoproduct in aqueous solution. *Phys. Chem. Chem. Phys.*, 12:15744–15750, 2010.

[125] A. Giussani, M. Merchan, D. Roca-Sanjuan, and R. Lindh. Essential on the photophysics and photochemistry of the indole chromophore by using a totally unconstrained theoretical approach. *J. Chem. Theory Comput.*, 7:4088–4096, 2011.

[126] C. Brand, J. Kupper, D. W. Pratt, W. Leo Meerts, D. Krugler, J. Tatchen, and M. Schmitt. Vibronic coupling in indole: I. Theoretical description of the $^1L_a - {}^1L_b$ interaction and the electronic spectrum. *Phys. Chem. Chem. Phys.*, 12:4968–4979, 2010.

[127] P. R. Callis and T. Liu. Vibronic coupling in indole: II. Investigation of the $^1L_a - {}^1L_b$ interaction using rotationally resolved electronic spectroscopy. *Phys. Chem. Chem. Phys.*, 12:4980–4988, 2010.

[128] G. Kumar, A. Roy, R. S. McMullen, S. Kutagulla, and S. E. Bradforth. The influence of aqueous solvent on the electronic structure and non-adiabatic dynamics of indole explored by liquid-jet photoelectron spectroscopy. *Faraday Discuss.*, 212:359–381, 2018.

[129] T. J. Godfrey, H. Yu, M. S. Biddle, and S. Ullrich. A wavelength dependent investigation of the indole photophysics via ionization and fragmentation pump–probe spectroscopies. *Phys. Chem. Chem. Phys.*, 17:25197–25209, 2015.

[130] T. J. Godfrey, H. Yu, and S. Ullrich. Investigation of electronically excited indole relaxation dynamics via photoionization and fragmentation pump-probe spectroscopy. *J. Chem. Phys.*, 141:44314, 2014.

[131] R. Livingstone, O. Schalk, A. E. Boguslavskiy, G. Wu, L. T. Bergendahl, A. Stolow,

M. J. Paterson, and D. Townsend. Following the excited state relaxation dynamics of indole and 5-hydroxyindole using time-resolved photoelectron spectroscopy. *The Journal of Chemical Physics*, 135:194307, 2011.

[132] M. Wohlgemuth, V. Bonacic-Koutecky, and R. Mitric. Time-dependent density functional theory excited state nonadiabatic dynamics combined with quantum mechanical/molecular mechanical approach: Photodynamics of indole in water. *J. Chem. Phys.*, 135:54105, 2011.

[133] G. Gregoire, C. Jouvet, C. Dedonder, and A. L. Sobolewski. On the role of dissociative $\pi\sigma^*$ states in the photochemistry of protonated tryptamine and tryptophan: An ab initio study. *Chem. Phys.*, 324:398–404, 2006.

[134] A. L. Sobolewski and W. Domcke. Ab initio investigations on the photophysics of indole. *Chem. Phys. Lett.*, 315:293–298, 1999.

[135] A. Warshel and M. Levitt. Theoretical studies of enzymic reactions: Dielectric, electrostatic and steric stabilization of the carbonium ion in the reaction of lysozyme. *J. Mol. Biol.*, 103:227–249, 1976.

[136] D. V. Bent and E. Hayon. Excited state chemistry of aromatic amino acids and related peptides. III. Tryptophan. *J. Am. Chem. Soc.*, 97:2612–2619, 1975.

[137] H. Kandori, R. Borkman, and K. Yoshihara. Picosecond transient absorption of aqueous tryptophan. *J. Phys. Chem.*, 97:9664–9667, 1993.

List of Figures